

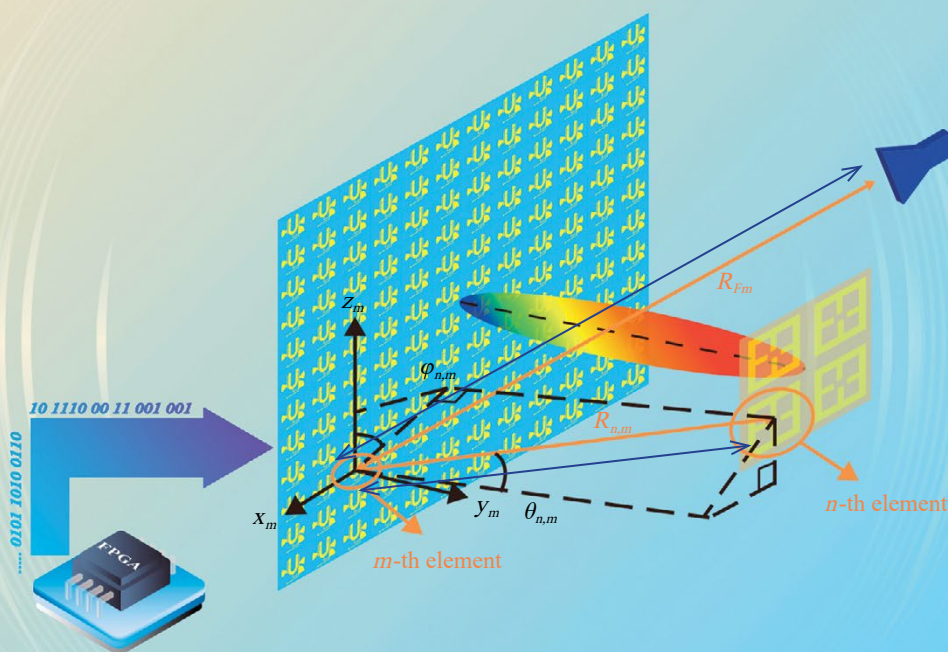


ZTE COMMUNICATIONS

中兴通讯技术(英文版)

June 2022, Vol. 20 No. 2

Special Topic: Simultaneous Wireless Information and Power Transfer: Technology and Practice



Special Topic ►

Simultaneous Wireless Information and Power Transfer: Technology and Practice

01 Editorial YUAN Qiaowei, LUO Fa-Long

03 High-Power Simultaneous Wireless Information and Power Transfer: Injection-Locked Magnetron
Technology YANG Bo, MITANI Tomohiko, SHINOHARA Naoki, ZHANG Huaiqing

Applications using simultaneous wireless information and power transfer have increased significantly. Wireless communication technology can be combined with the Internet of Things to develop many innovative applications using SWIPT, which is mainly based on wireless energy harvesting from electromagnetic waves used in communications. Wireless power transfer that uses magnetrons has been developed for communication technologies. Injection-locked magnetrons that can be used to facilitate high-power SWIPT for several devices are reviewed in this paper. This new technology is expected to pave the way for promoting the application of SWIPT in a wide range of fields.

13 An Overview of SWIPT Circuits and Systems
..... Ricardo TORRES, Diogo MATOS, Felisberto PEREIRA, Ricardo CORREIA, Nuno Borges CARVALHO

From a circuit implementation perspective, this paper presents a brief overview of simultaneous wireless information and power transmission. By creating zero-power batteryless wireless sensors, SWIPT mixes wireless power transmission with wireless communications to allow the truly practical implementation of the Internet of Things as well as many other applications. What is addressed in this paper about SWIPT mainly includes technical backgrounds, problem formation, state-of-the-art solutions, circuit implementation examples and system integrations.

19 Optimal Design of Wireless Power Transmission Systems Using Antenna Arrays
..... SUN Shuyi, WEN Geyi

Three design methods for wireless power transmission systems using antenna arrays have been investigated. The three methods, corresponding to three common application scenarios of WPT systems, are based on the method of maximum power transmission efficiency between two antenna arrays. They are unconstrained MMPTE, weighted MMPTE and constrained MMPTE. To demonstrate the optimal design process with the three methods, a WPT system operating at 2.45 GHz is designed, simulated and fabricated, in which the transmitting (Tx) array, consisting of 36 microstrip patch elements, is configured as a square and the receiving array, consisting of 5 patch elements, is configured as an L shape. The power transmission efficiency is then maximized for the three application scenarios, which yields the maximum possible PTEs and the optimized distributions of excitations for both Tx and Rx arrays. The feeding networks are then built based on the optimized distributions of excitations. Simulations and experiments reveal that the unconstrained MMPTE, which corresponds to the application scenario where no radiation pattern shaping is involved, yields the highest PTE. The next highest PTE belongs to the weighted MMPTE, where the power levels at all the receiving elements are imposed to be equal. The constrained MMPTE has the lowest PTE, corresponding to the scenario in which the radiated power pattern is assumed to be flat along the Rx array.

Submission of a manuscript implies that the submitted work has not been published before (except as part of a thesis or lecture note or report or in the form of an abstract); that it is not under consideration for publication elsewhere; that its publication has been approved by all co-authors as well as by the authorities at the institute where the work has been carried out; that, if and when the manuscript is accepted for publication, the authors hand over the transferable copyrights of the accepted manuscript to *ZTE Communications*; and that the manuscript or parts thereof will not be published elsewhere in any language without the consent of the copyright holder. Copyrights include, without spatial or timely limitation, the mechanical, electronic and visual reproduction and distribution; electronic storage and retrieval; and all other forms of electronic publication or any other types of publication including all subsidiary rights.

Responsibility for content rests on authors of signed articles and not on the editorial board of *ZTE Communications* or its sponsors.

All rights reserved.

28 Dynamic Power Transmission Using Common RF Feeder with Dual Supply
..... DUONG Quang-Thang, VO Quoc-Trinh, PHAN Thuy-Phuong, OKADA Minoru

This paper proposes the design concept of a dynamic charging system for electric vehicles using multiple transmitter coils connected to a common RF feeder driven by a pair of two power supplies. The authors employ a pair of two power sources which are electrically separated by an odd-integer number of quarter wavelength to drive the RF feeder. As a result, the voltage standing wave generated by one power source is complemented by that of the other, leading to stable received power and transmission efficiency at all the receiver's positions along with the charging pad.

37 Polarization Reconfigurable Patch Antenna for Wireless Power Transfer Related Applications
..... SHEN Jun, ZHAO Tianxiang, LIU Xueguan

A polarized reconfigurable patch antenna is proposed in this paper. The proposed antenna is a dual cross-polarized patch antenna with a programmable power divider. The phase-controlled power divider and the cross dual-polarized antenna are designed, fabricated and tested, and then they are combined to realize the polarized reconfigurable antenna. By moving the phase of the phase shifter, the antenna polarization is reconfigured into VP, HP, and CP. The test is conducted at the frequency of 915 MHz, which is widely used for SWIPT in RFID applications. The results demonstrate that when the antenna is configured as CP, the axial ratio of the antenna is less than 3 dB, and when the antenna is configured as HP or VP, the axial ratio of the antenna exceeds 20 dB. Finally, experiments are conducted to verify the influence of antenna polarization changes on wireless power transmitting.

43 A Radio-Frequency Loop Resonator for Short-Range Wireless Power Transmission
..... WANG Xin, LI Wenbo, LU Mingyu

A microstrip loop resonator loaded with a lumped capacitor is proposed for short-range wireless power transmission applications. Power transmission efficiency of greater than 80% is achieved with a power transmission distance smaller than 5 mm via the strong coupling between two loop resonators around 1 GHz, as demonstrated by simulations and measurements. Experimental results also show that the power transmission performance is insensitive to various geometrical misalignments. The numerical and experimental results of this paper reveal a bandwidth of more than 50 MHz within which the power transmission efficiency is above 80%.

Review ►

48 Programmable Metasurface for Simultaneously Wireless Information and Power Transfer System
..... CHANG Mingyang, HAN Jiaqi, MA Xiangjin, XUE Hao, WU Xiaonan, LI Long, CUI Tiejun

The authors elaborate on a system solution using PMS for SWIPT, offering an optimized wireless energy management network. Both transmitting and receiving sides of the proposed solution are presented in detail. More importantly, a numerical model based on the plane-wave angular spectrum method is investigated to accurately calculate the radiation fields of PMS in the Fresnel and Fraunhofer regions. Using this model, efficiencies of WPT between the transmitter and the receiver are analyzed. Finally, future research directions are discussed, and integrated PMS for the wireless information and wireless power is outlined.

Serial parameters: CN 34-1294/TN*2003*q*8*62*en*P*¥30.00*2200*10*2022-06

Statement

This magazine is a free publication for you. If you do not want to receive it in the future, you can send the "TD unsubscribe" mail to magazine@zte.com.cn. We will not send you this magazine again after receiving your email. Thank you for your support.



Editorial: Special Topic on Simultaneous Wireless Information and Power Transfer: Technology and Practice

Guest Editors >>>



YUAN Qiaowei received the BE, ME and PhD from Xidian University, China in 1986, 1989 and 1997, respectively. From 1990 to 1991, she was a special research student at Tohoku University, Japan. She worked with the Sendai Research and Development Laboratory, Matsushita Communication Company, Ltd., Japan from 1992 to 1995, with the Sendai Research and Development Center, Oi Electric Company, Ltd., Japan from 1997 to 2002, and with the Intelligent Cosmos Research Institute, Japan from 2002 to 2007. From 2007 to 2008, she was an associate professor with Tokyo University of Agriculture and Technology, Japan. She was an associate professor/professor with the National Institute of Technology, Sendai College, Japan from April 2009 to March 2020. Since April 2020, she has been a professor with Tohoku Institute of Technology, Japan, and since September 2021, she has also been a specially appointed professor at Tohoku University, Japan. Dr. YUAN received the Best Paper Award and Zenichi Kiyasu Award from the Institute of Electronics, Information and Communication Engineers (IEICE) of Japan in 2009. She also received the Achievement Award from IEICE in 2015, and other Achievement Awards from the IEICE Technical Committee on Wireless Power Transfer from 2016 to 2017. Dr. YUAN served as the secretary of the IEICE Technical Committee on Wireless Power transfer of Japan from 2012 to 2014. She also served as the vice chair of IEEE Sendai WIE from 2017 to 2018 and has been the chair of IEEE Sendai WIE from 2019 to 2022. Now she is an IEEE R10 WIE committee member and IEEE MTT-25 committee member.



LUO Fa-Long is an IEEE Fellow and an affiliate full professor with the Electrical & Computer Engineering Department at the University of Washington in Seattle, the US. Having gained international high recognition, Dr. LUO has 39 years of research and industry experience in wireless communications, neural networks, signal processing, machine learning and broadcasting with real-time implementation, applications and standardization. Including his well-received books *Applied Neural Networks for Signal Processing* (1999, Cambridge) and *Signal Processing for 5G* (2016, Wiley-IEEE), he has published seven books and more than 100 technical papers in the related fields. Dr. LUO has also contributed 105 patents/inventions which have successfully resulted in a number of new or improved commercial products in mass production. Now he serves as a board member of both the Conference Board and the Membership Board of the IEEE Signal Processing Society (SPS), as well as an IEEE Fellow Committee member. He has also served as the chairman of IEEE Industry Digital Signal Processing (IDSP) Standing Committee and the technical board member of IEEE SPS. Dr. LUO was awarded the Research Fellowship by the Alexander von Humboldt Foundation of Germany.

While having enabled human beings to realize the dream of communicating with whomever whenever and wherever, wireless technologies and applications are being developed at a very rapid speed and in a massively large scale as we have entered the 5G era and several grand 6G plans have also been clearly visible. However, most electronic products, including mobile phones, still have not gotten rid of the shackles of power wires. The wirelessization of electric energy is another major challenge for mankind following the discovery of electromagnetic waves. In the past 20 years, wireless power transfer (WPT) has once again received great attention and development. Simultaneous wireless information and power transfer (SWIPT) is a combination of wireless power transmission and wireless information transmission (WIT). With great advantages of parallel transmission of information and energy,

SWIPT has broad application prospects and brings revolution in various industrial fields and our daily life.

This special issue focuses on the SWIPT technology development in terms of both WIT and WPT aspects. The topics addressed in this special issue cover a broad range from the element configuration to system design of SWIPT applications, mainly including cutting-edge high power SWIPT technologies, novel receiver and transmitter design techniques, and multiple-input multiple-output (MIMO) techniques for SWIPT applications. Especially, the compatibility and commonality among SWIPT solutions are highlighted for multiple application scenarios. The call-for-papers of this special issue have brought excellent submissions in both quality and quantity. After two-round reviews, seven excellent papers have been selected for publication in this special issue which is organized as follows.

The first paper titled “High-Power Simultaneous Wireless Information and Power Transfer: Injection-Locked Magnetron Technology” reviews the latest research findings on injection-locked magnetrons that can be used in high-power SWIPT systems developed by the authors. In this paper, the performance

DOI: 10.12142/ZTECOM.202202001

Citation: Q. W. Yuan and F.-L. Luo, “Editorial: special topic on simultaneous wireless information and power transfer: technology and practice,” *ZTE Communications*, vol. 20, no. 2, pp. 1 – 2, Jun. 2022. doi: 10.12142/ZTECOM.202202001.

of injection-locked magnetrons using amplitude, phase, and frequency modulation is evaluated. The experimental results show that the highest data rate can reach 10 Mbit/s, demonstrating that the injection-locked magnetron can maintain high-power output and modulate the sound signal, motor control signal, and video signal simultaneously. The wirelessly powered TV system using injection-locked magnetrons is an amazing application that shows the technique could be applied to both the Internet of Things (IoT) and Internet of Everything (IoE) society. Potential SWIPT applications have been increased significantly by the proposed injection-locked magnetrons technique.

The second paper titled “An Overview of SWIPT Circuits and Systems” presents a brief overview of SWIPT from a circuit implementation perspective. What the paper mainly addresses include the technical backgrounds, problem formations, state-of-the-art solutions, circuit implementation examples and system integrations. With the combination of wireless power transmission and backscatter communications, the use of higher-order modulation formats integrates WIT and WPT systems, reducing the need for batteries significantly in these sensors and creating the path for a true Internet of Everything in the future.

Titled “Optimal Design of Wireless Power Transmission Systems Using Antenna Arrays”, the third paper investigates three design methods for WPT systems using antenna arrays, focusing on optimal design for MIMO of both WIT and WPT systems. To demonstrate the optimal design processes of the three methods, a WPT system operating at 2.45 GHz is designed, simulated and fabricated. In this system, the Tx array with 36 microstrip patch elements is configured as a square, while the Rx array with five patch elements is configured as an L shape. Simulations and experiments reveal that the three optimization methods proposed for the design of WPT systems are applicable to any environment and any antenna array.

The fourth paper titled “Dynamic Power Transmission Using Common RF Feeder with Dual Supply” proposes a design concept of a dynamic charging system for electric vehicles using multiple transmitter coils connected to a common RF feeder driven by a pair of two power supplies. Using a common RF feeder for multiple transmitter coils can reduce the power electronic redundancy compared to the conventional system where each transmitter coil is individually driven by one switched mode power supply. As a result, the voltage standing wave generated by one power source is complemented by that of the other, leading to stable received power and transmission efficiency at all the receiver positions along with the charging pad. The simulation results at the 85 kHz frequency band verify the output power stabilization effect of the proposed design. The authors of this paper have indicated that the proposed concept can also be applied to simultaneous wireless information and power transfer for passive radio frequency identification (RFID) tags by raising the operation frequency to higher Industrial, Scientific, and Medical (ISM) bands, e.g., 13.56 MHz and employing similar

modulation methods used for the current RFID technology.

The fifth paper titled “Polarization Reconfigurable Patch Antenna for Wireless Power Transfer Related Applications” proposes a polarized reconfigurable patch antenna composed of a dual cross-polarized patch antenna and a programmable power divider. The programmable power divider consists of two branch line couplers (BLC) and a digital phase shifter. The proposed phase-controlled power divider and the cross dual-polarized antenna are designed, fabricated, and tested. The experiments show that different antenna polarizations can be configured through the programmable phase shifter without changing the antenna gain performance. The wireless power transmission experiment demonstrates that tuning the transmitting antenna polarization to match the receiving antenna polarization can improve the efficiency of wireless power transmission.

The sixth paper titled “A Radio-Frequency Loop Resonator for Short-Range Wireless Power Transmission” proposes a microstrip loop resonator loaded with a lumped capacitor for short-range wireless power transmission applications. The overall physical dimensions of the proposed loop resonator configuration are as small as 3 cm by 3 cm. Simulation and measurement data demonstrate that the strong coupling between two loop resonators around 1 GHz can realize the power transmission efficiency of greater than 80% with a power transmission distance smaller than 5 mm. The experimental results also show that the power transmission performance is insensitive to various geometrical misalignments.

Serving as a review-style paper and the last paper of this special issue, the seventh paper is titled “Programmable Metasurface for Simultaneously Wireless Information and Power Transfer System” and presents a system solution using programmable metasurface (PMS) for SWIPT, offering an optimized wireless energy management network. Both transmitting and receiving sides of the proposed solution are introduced in detail. On the transmitting side, the WPT technique is used in versatile power conveying strategies for near-field or far-field targets, single or multiple targets, and equal or unequal power targets. On the receiving side, the wireless energy harvesting (WEH) technique can work well on multi-functional rectifying metasurfaces that collect the wirelessly transmitted energy and the ambient energy. More importantly, a dedicated numerical model based on the plane-wave angular spectrum method is investigated to accurately calculate the radiation fields of PMS in the Fresnel and Fraunhofer regions. Moreover, future research directions of the integrated PMS for wireless information and wireless power are highlighted in this paper.

As we conclude the introduction to this special issue and the content of seven papers, we would like to thank all authors for their valuable contributions. We also express our sincere gratitude to all the reviewers for their timely and insightful comments on all submitted papers. It is hoped that this special issue is informative and useful for future SWIPT technology developments and practical applications.



High-Power Simultaneous Wireless Information and Power Transfer: Injection-Locked Magnetron Technology

YANG Bo¹, MITANI Tomohiko¹, SHINOHARA Naoki¹,
ZHANG Huaqing²

(1. RISH, Kyoto University, Kyoto 6110011, Japan;
2. Chongqing University, Chongqing 400044, China)

DOI: 10.12142/ZTECOM.202202002

<https://kns.cnki.net/kcms/detail/34.1294.TN.20220513.2202.002.html>,
published online May 16, 2022

Manuscript received: 2022-04-18

Abstract: Applications using simultaneous wireless information and power transfer (SWIPT) have increased significantly. Wireless communication technologies can be combined with the Internet of Things to develop many innovative applications using SWIPT, which is mainly based on wireless energy harvesting from electromagnetic waves used in communications. Wireless power transfer that uses magnetrons has been developed for communication technologies. Injection-locked magnetrons that can be used to facilitate high-power SWIPT for several devices are reviewed in this paper. This new technology is expected to pave the way for promoting the application of SWIPT in a wide range of fields.

Keywords: simultaneous wireless information and power transfer; wireless power transfer; magnetrons; injection-locked; Internet of Energy; Internet of Things

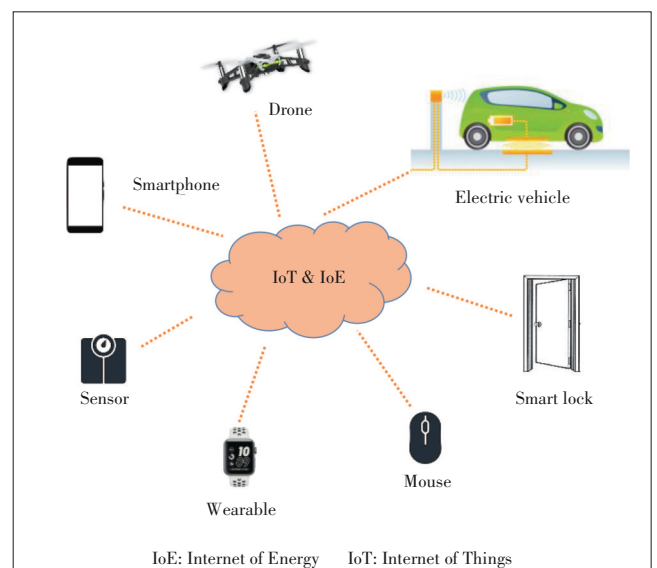
Citation (IEEE Format): B. Yang, T. Mitani, N. Shinohara, et al., "High-power simultaneous wireless information and power transfer: injection-locked magnetron technology," *ZTE Communications*, vol. 20, no. 2, pp. 3 – 12, Jun. 2022. doi: 10.12142/ZTECOM.202202002.

1 Introduction

Governments worldwide have reached a consensus and signed the "Paris Agreement," which aims to reduce global carbon emissions significantly. However, the signing of this agreement alone will not be sufficient to reduce carbon emissions. We have to increase the current energy utilization rate while looking for new renewable energy sources. Simultaneous wireless information and power transfer (SWIPT) is a technology that has drawn increasing attention lately. SWIPT can collect electromagnetic wave energy used in communications and supply it to low-power devices, such as sensors. In SWIPT products, near-field communication (NFC) and radio frequency identifier (RFID) technologies are being widely used. These two technologies have become indispensable for building the Internet of Things (IoT). The Internet of Energy (IoE) society advocates smart power systems that can be used to optimize IoT-based energy use. The SWIPT technology is being used in a wide range of devices as shown in Fig. 1. SWIPT is used in ap-

plication scenarios of both low-power and high-power devices, such as mobile phones, electric vehicles and drones, which require high-power SWIPT.

SWIPT can be classified using several methods. For ex-



▲ Figure 1. Applications of simultaneous wireless information and power transfer (SWIPT)

This work was supported by the collaborative research program from the Microwave Energy Transmission Laboratory (METLAB), Research Institute for Sustainable Humanosphere (RISH), Kyoto University and National Institute of Information and Communications Technology (NICT), JAPAN under Grant No. 02401.

ample, it can be classified under time, power, antenna, and space domains^[1]. Based on the wireless power transfer (WPT) technology used, it can also be classified under inductive coupling^[2-3], capacitive coupling^[4-5], magnetic resonance coupling^[6-7], and microwave or other radio frequencies radiation^[8-9]. Besides, based on WPT and wireless information transfer (WIT) signals involved, SWIPT can be classified under the multiplexing signal^[8-9], the different signals^[10] and the different helical modes of the orbital angular momentum^[11-12]. According to its development history, the technical routes taken by the development of SWIPT can be divided into wireless energy harvesting (WEH) technology based on wireless communication technology and WPT technology for communication functions. The former is mainly used in low-power devices, and the latter, referred to as high-power SWIPT in this review, is mainly used in high-power applications. Lately, SWIPT researchers have focused their attention on low-power WEH. However, high-power SWIPT has many application prospects. For example, wireless charging of flying drones using a WPT system and beamforming technology will enable the drone to fly for a long time^[13].

The Japanese government has enforced new radio regulations for high-power WPT via microwave and released three frequency bands for WPT^[14]. The maximum power allowed in WPT in the 5.75 GHz band is 32 W, which is much above the power allowed in communications. This new standard, being the first commercialized microwave WPT standard released, is expected to bring many innovative applications to WPT systems. In the United States, Energous Corp. and Ossia Inc. have obtained authorization from the Federal Communications Commission (FCC) for WattUp^[15] and Cota^[16], respectively, for real WPT systems. These products can be used for charging mobile phones, watches, and other consumer electronics. They will not be useful in high-power applications, such as drones and electric vehicles.

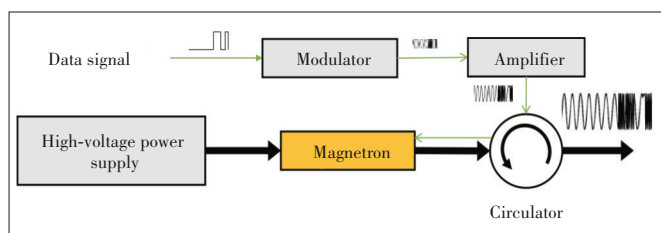
Here, we summarize the results of studies conducted on high-power WPT using injection-locked magnetrons and the modulation technologies used. The frequency stability of magnetrons is poor, although compared with other amplifiers, magnetrons have high power density, have high efficiency, and are of low cost. A previous study discussed how the phase and power of a magnetron output could be controlled^[17]. TAHIR et al. developed a 2.45 GHz injection-locked magnetron as a communication transmitter and transmitted data using 2 Mbit/s phase-shift keying (PSK)^[18]. With injection locking, 2.45 GHz and 5.8 GHz continuous-wave magnetrons can be used for amplitude, phase, and frequency modulation (FM)^[19] to achieve data transmission rates as high as 10 Mbit/s. An experimental study of a television broadcasting system that was wirelessly powered by an injection-locked magnetron has been reported^[20]. These studies prove that injection-locked magnetrons are sufficiently stable for use in WIT systems. This review presents the technical principles, latest developments,

and future trends of injection-locked magnetrons and their associated modulation technologies, and identifies the challenges and future development directions of high-power SWIPT.

2 Overview of Injection-Locked Magnetrons

A magnetron can be modulated by adjusting its output. Four methods are available to adjust the output of a magnetron. These methods involve the control of one of the following magnetron parameters: 1) anode current^[21-22], 2) magnetic field^[22-24], 3) filament power^[19], and 4) injection power^[18-19,25]. In Method 1), a high-voltage power supply is used to change the anode current of the magnetron or couple the data signal to the anode voltage. The rise time of the low-ripple high-voltage power supply has to be approximately 3 ms^[19]. A high-response pulse-drive power supply can have a rise time of 0.1 ms^[26]. The rise time of the power supply limits the data rate that can be achieved at high speeds. In Methods 2) and 3), the control parameter requires a large and fast response power supply. Method 4) can be realized by a low-power data signal which can be modulated as the injection signal. This section will present a detailed description of Method 4) used in injection-locked magnetrons.

In an injection-locked magnetron, a signal is injected into the magnetron, and the magnetron output is locked with the injection signal. The injection signal frequency is set close to the self-oscillation frequency of the magnetron. The locked frequency range Δf can be expressed as $\Delta f = 2f \sqrt{P_i/P_o} / Qe^{[27]}$, where f is the injection signal frequency, P_i is the injection signal power, P_o is the magnetron output power, and Qe is the external Q-factor of the magnetron. Within the locked frequency range of Δf , the frequency and phase of the magnetron output are locked with those of the injection signal. Therefore, by controlling the injection signal parameters, the magnetron output can be made to synchronize with the injection signal. In addition, when the modulation signal is injected, the magnetron output will get locked with the injection signal, and the magnetron will amplify the modulation signal by working as an amplifier (Fig. 2). In the absence of an injection signal, the output of the magnetron will be a high-power signal, different from that produced by a power amplifier. Thus, a SWIPT system receiver will have power stability even when no data is transferred through the communication channel.



▲ Figure 2. Schematic of injection-locked magnetron system

2.1 Amplitude-Shift Keying Used in Injection-Locked Magnetron

In the system shown in Fig. 2, the data signal is modulated by the modulator using amplitude-shift keying (ASK). The modulated signal is amplified and injected into the magnetron through a circulator. The power of the injection signal changes from approximately 6.6 W to 22 W. The modulation depth is set to 70%. When the output power of the magnetron was measured using a signal analyzer, it was found to have shifted by approximately 6%^[19]. The amplitude depth of the injection-locked magnetron output is lower than that of the injection signal. Magnetron behavior is different from amplifier behavior because the gain of the magnetron fluctuates when the injected power is increased. The modulation depth of the injected power affects the offset level of the magnetron output power.

Error vector magnitude (EVM), magnitude error (MAG Err), phase error (Phase Err), and frequency error (Freq Err) are used to evaluate the modulated signal quality. The modulated data signal uses a pseudo-noise (PN) 9 sequence. When using ASK modulation at 200 kbit/s, the quality of the injection-locked magnetron output ($P_o/P_i = 13.5$ dB) and the injection signal are not much different as shown in Table 1.

Two conditions have to be satisfied for the injection-locked magnetron to function as an amplitude modulator. First, the modulation amplitude of the injection signal has to be lowered to keep the magnetron working in a frequency-locked state. Second, fast data rates require wide bandwidths, which have to be narrower than the locked frequency range Δf .

2.2 Phase-Shift Keying Used in Injection-Locked Magnetron

When used in the magnetron, PSK follows a procedure similar to that used by ASK. To use PSK, the modulator type in Fig. 2 has to be changed from ASK to PSK. The data signal is modulated onto a carrier signal using a phase shift of 180° . The modulated signal passes through a power amplifier with

an injection power of 14 W. The output of the magnetron is locked with the injection signal, and a PSK-modulated signal will be available at the magnetron output.

When the magnetron is used for PSK modulation, a double balanced mixer is used to compare a sine wave with the output signal of the magnetron. The intermediate frequency (IF) port of the mixer is connected to a low-pass filter. When the demodulated signal is observed using an oscilloscope, the rising time t_{rise} of the phase-modulated signal at the magnetron output ($P_o/P_i = 16.4$ dB) is found to be approximately 59 ns. The maximum data transmission rate, f_p , can be expressed as $f_p = \alpha/t_{rise}$, where α is a constant (usually set to less than 0.35)^[19]. In a previous study, the response time of the magnetron was expressed as $(Qe/2\pi f) \sqrt{P_o/P_i}$, which has been derived using Alder's equations^[18]. According to this formula, a high injection power will reduce the magnetron response time, thereby enabling a high transmission rate.

We observe that the phase noise at 60 Hz caused by the filament power supply is present in the output of the injection-locked magnetron. This phase noise can be avoided by turning off the filament power supply, high-pass filter, or phase-locked looping^[17]. As with ASK, the system has been designed to make the magnetron work only in the injection-locked state. With multi-value phase modulation methods, such as quadrature phase-shift keying (QPSK) and eight phase-shift keying (8PSK), the transmission rate of the data signal is found to be 10 Mbit/s when measured with a signal analyzer. The quality of the magnetron output is slightly lower than that of the injection signal, although it is still within the usable range.

2.3 Frequency-Shift Keying Used in Injection-Locked Magnetron

Frequency-shift keying (FSK) has many advantages, such as low cost and strong noise immunity. It can be used in injection-locked magnetrons. An FSK experiment is similar to

▼ **Table 1. Parameters measured in injection-locked magnetron experiments^[19]**

		Injection signal (signal generator & amplifier)				Magnetron output			
Type	Data rate	EVM/%	MAG Err/%	Phase Err/deg	Freq Err/Hz	EVM/%	MAG Err/%	Phase Err/deg	Freq Err/Hz
ASK	200 kbit/s	1.74	1.48	0.540 4	3 489.5	2.29	0.49	1.307 4	3 708.7
BPSK	10 Mbit/s	4.24	4.02	0.776 3	78.137	8.85	8.33	1.704 8	3 397.1
QPSK	10 Mbit/s	5.29	4.10	1.933 7	3.606 8	9.21	7.17	3.277 6	-18.842
8PSK	5 Mbit/s	5.62	4.06	2.254 2	41.388	11.37	6.36	5.457 7	78.593
MSK	10 Mbit/s	3.03	0.91	3.652 5	3.326 9	6.56	3.02	2.885 8	30.079
Type	Data rate/(Mbit/s)	FSK Err/%	MAG Err/%	CF offset/kHz	Freq DEV/Hz	FSK Err/%	MAG Err/%	CF Offset/kHz	Freq DEV/Hz
2 FSK	10	2.61	0.83	1.731 3	975.96	6.38	8.12	0.1730	928.88
4 FSK	10	2.22	0.75	-2.411 6	972.16	5.13	0.64	2.913 8	929.53
8 FSK	5	0.78	0.78	0.175 17	993.53	1.45	0.62	0.263 6	981.90
16 FSK	10	2.09	0.65	0.661 01	976.22	4.20	0.61	10.662	1 025.4

8PSK: eight phase-shift keying
 ASK: amplitude-shift keying
 BPSK: binary phase-shift keying

CF: carrier frequency
 Err: phase error
 EVM: error vector magnitude

Freq DEV: frequency deviation
 Freq Err: frequency error
 FSK: frequency-shift keying

MAG Err: magnitude error
 MSK: minimum-shift keying Phase
 QPSK: quadrature phase-shift keying

the PSK experiment. After the modulation type of the magnetron to FSK is set, the frequency deviation will also be set. The FSK-modulated signal is amplified and injected into the magnetron through a circulator, the magnetron is locked by the FSK signal, and the FSK signal is amplified. A frequency demodulator is used to demodulate the output signal of the magnetron. An oscilloscope is used to measure the relevant parameters of the demodulated signal, which are almost similar to those of the signal obtained using PSK. This injection-locked magnetron can output FSK signals at a speed of 10 Mbit/s. The relevant parameters include the carrier frequency (CF offset) and frequency deviation (Freq DEV) of the demodulated signals obtained from multi-value frequency modulated signals (Table 1). All parameters relating to FSK are consistent with those related to PSK although FSK modulation quality is better than PSK modulation quality.

A low modulation index will produce only a few sidebands. Multi-value FSK modulations have high bandwidth efficiency. For the same locked frequency range of Δf , a lower modulation index and multi-value FSK modulations will produce a faster transmission rate. As with ASK, the FSK bandwidth has to be narrower than the locked frequency range Δf .

2.4 Challenges Faced in Using Injection-Locked Magnetrons as Modulators

Compared with that of other devices, the communication bandwidth of an injection-locked magnetron is narrow because it has to be less than its locked frequency range. Because the modulation depth of an ASK-modulated signal obtained from an injection-locked magnetron cannot be linearly related to the injection signal, the use of modulation methods, such as quadrature amplitude modulation, is difficult in injection-locked magnetrons. The maximum transmission rate of PSK and FSK-modulated signals that are currently possible is only 10 Mbit/s. It cannot be increased to 5G and Wi-Fi transmission rates without making a major structural adjustment in the magnetron. A past study has revealed that by improving impedance matching, the magnetron bandwidth could be increased^[28]. Utilizing a three-screw tuner, the magnetron bandwidth was increased from 2~6 MHz to 120 MHz. The bandwidth could be increased by using a time splitter or a signal separator in analog signal modulation or low-rate data communication, such as that required with motor control signals. The injection-locked magnetron for the high-power SWIPT is still the best worth looking forward to wide applications.

Regulations and standards also pose challenges. The continuous-wave magnetrons are currently being used mainly in microwave ovens and industrial heaters, which are used in closed spaces. However, because SWIPT is applied in open spaces, appropriate regulations have to be formulated. In the case of high-power SWIPT, standards specific to it have to be prepared. Magnetrons are extensively used in industrial applications using devices such as microwave ovens and other heat-

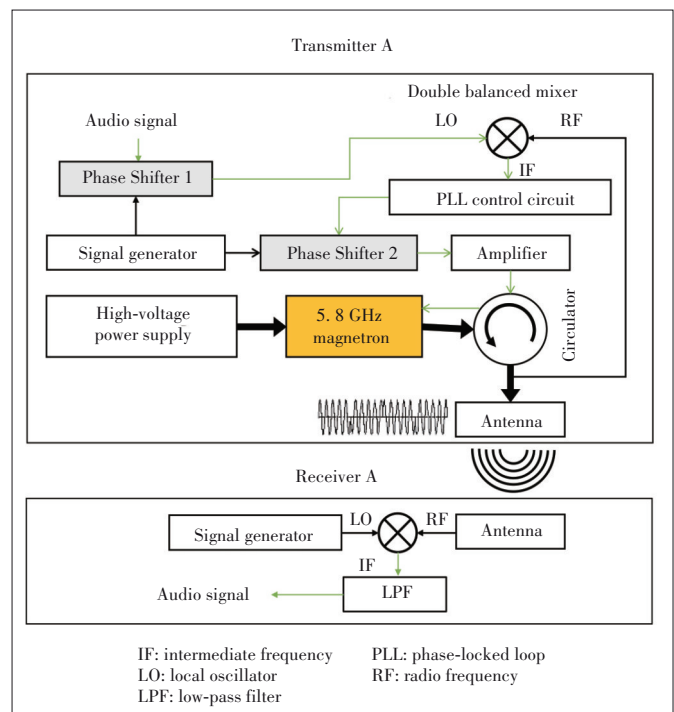
ing devices, where the low cost of the magnetrons is an advantage compared to that of other devices.

3 High-Power SWIPT Systems

The earliest use of magnetrons in communications can be traced back to the 1940s, and in 1953, the 100 W frequency variable magnetron M402, operating in the 6 GHz band with a frequency range of 1 MHz, was developed and used in a 23-channel telephone system^[28]. However, because of the technological limitations that existed at that time, the magnetrons used in communications were gradually replaced by klystrons and semiconductors. WEGLEIN et al.^[29], TAHIR et al.^[18, 30], and READ et al.^[31] has mentioned a magnetron being used for modulation, however, there are no actual data has been performed. Here we present the latest developments in injection-locked magnetron systems producing modulated signals. The high-power SWIPT systems based on injection-locked magnetrons have been recently used in combination with the WPT technology to handle audio, motor control and video signals of wireless TV systems, and beamforming phased array systems used in video transmissions.

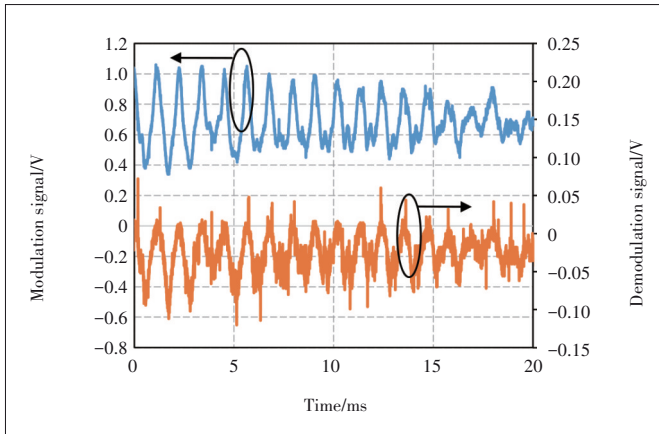
3.1 Demonstration of Phase-Controlled Magnetron System Used in Radio Broadcasting

The noise resistance of the phase-controlled magnetron (PCM) is considered higher than that of an injection-locked magnetron. The magnetron is used to transfer an audio signal (Fig. 3). The audio signal is fed into Phase Shifter 1, and the



▲ Figure 3. Schematic of phase-controlled magnetron system used in radio broadcasting^[19]

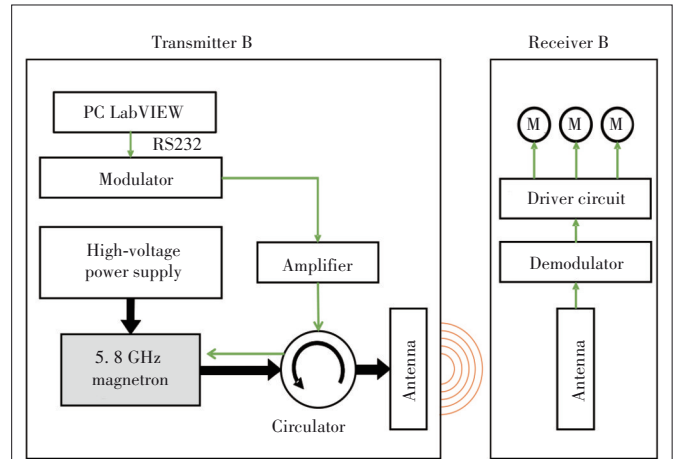
modulated signal is compared with the magnetron output by the double-balanced mixer. The signal at the IF port of the mixer representing the phase difference between the two signals compared is fed to the phase-locked loop (PLL) circuit to control Phase Shifter 2. The PLL circuit gradually reduces the phase difference between the two signals compared to bringing it to zero when the magnetron will produce a phase-modulated (PM) signal that follows the injection signal. In the receiver, the antenna is connected to a mixer, which works as a simple demodulator. The mixer produces at its IF port an audio signal corresponding to the phase difference between the signal generator output and the antenna signal. Fig. 4 shows the audio signal and the signal obtained by demodulating the PM signal. In this analog phase-modulating system, the WIT system acts as a radio broadcast system. A PCM with high noise resistance will avoid the 60 Hz phase noise produced by the filament. PCMs are expected to amplify multi-value PSK signals.



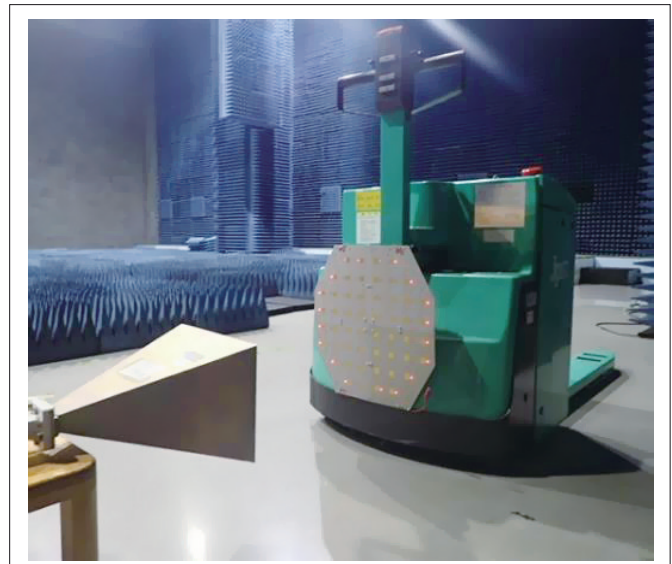
▲ Figure 4. Audio signal and demodulated signal obtained from a phase-modulated (PM) signal transmitted by the injection-locked magnetron (without filter)

3.2 Demonstration of a SWIPT System Used in a Remote-Controlled Electric Trolley

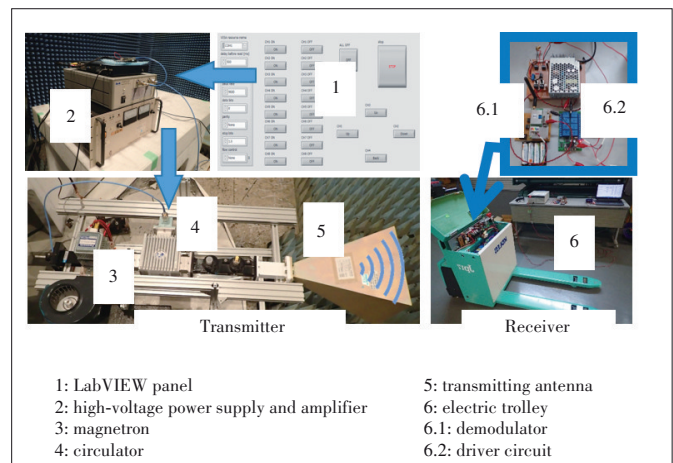
Fig. 5 shows the schematic of the SWIPT system used in an injection-locked magnetron producing FSK-modulated signals in the microwave range. An RS-232 signal corresponding to the motor control signal is fed into a modulator that produces an FSK-modulated signal. This modulated signal is amplified and injected into a 5.8 GHz band magnetron through a circulator. The magnetron is locked with the injection signal. The magnetron outputs FSK-modulated microwaves to an electric trolley through the horn antenna shown in Figs. 6 and 7. The receiver installed in the electric trolley receives the modulated microwaves and demodulates them to control the motors. Fig. 8 shows the control data pertaining to the transmitted and demodulated data. The operation of the data transfer system is confirmed at a high data transmission rate, such as 115 200 bit/s. The demodulated data is fed back to the RS-232 Rx/D port to check the data



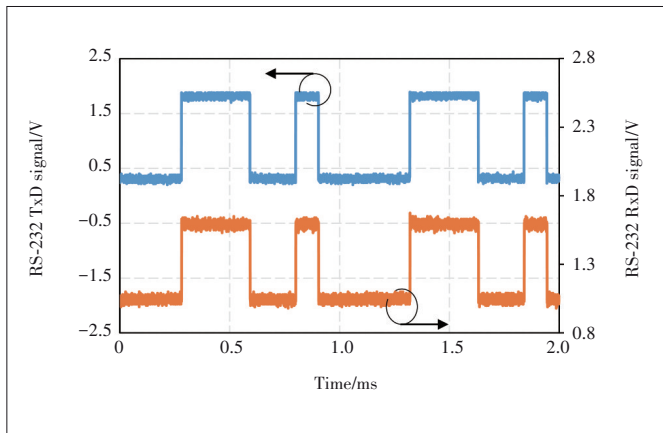
▲ Figure 5. Schematic of simultaneous wireless information and power transfer (SWIPT) used in an injection-locked magnetron to control an electric trolley^[32]



▲ Figure 6. Picture of simultaneous wireless information and power transfer (SWIPT) system used in an electric trolley control system



▲ Figure 7. Pictures of simultaneous wireless information and power transfer (SWIPT) system used in an electric trolley control system^[32]



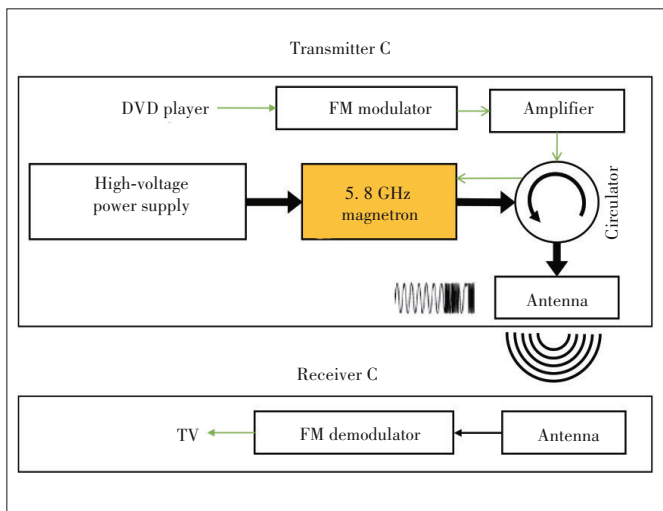
▲ Figure 8. Modulated and demodulated signals produced by the injection-locked magnetron^[32]

error without bit error.

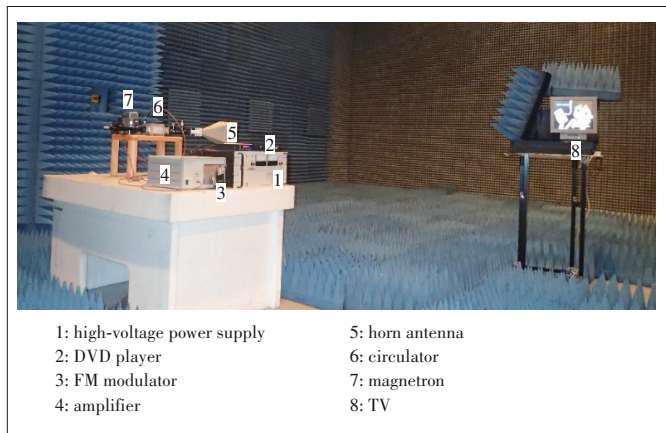
The experiment conducted using the 5.8 GHz injection-locked magnetron was on the use of a 655 W SWIPT system in an electric trolley remote-control system using FSK. With their increased industrial production, electric trolleys are being widely used in work related to factory automation. The remote electric trolley control system presented in this review would be suitable for applications involving smart factory and smart warehouse logistics.

3.3 Demonstration of Use of Frequency Modulation in Television Broadcasting System

In the TV broadcasting system shown in Figs. 9 and 10, FM is used with the analog video signal. A DVD player feeds audio and video signals to an FM modulator. The FM modulator output is amplified to 10 W. The modulated signal is injected into the magnetron. In the receiver, the demodulator produces the TV, video, and audio signals corresponding to the DVD signal.



▲ Figure 9. Schematic of TV broadcasting system using an injection-locked magnetron^[19]

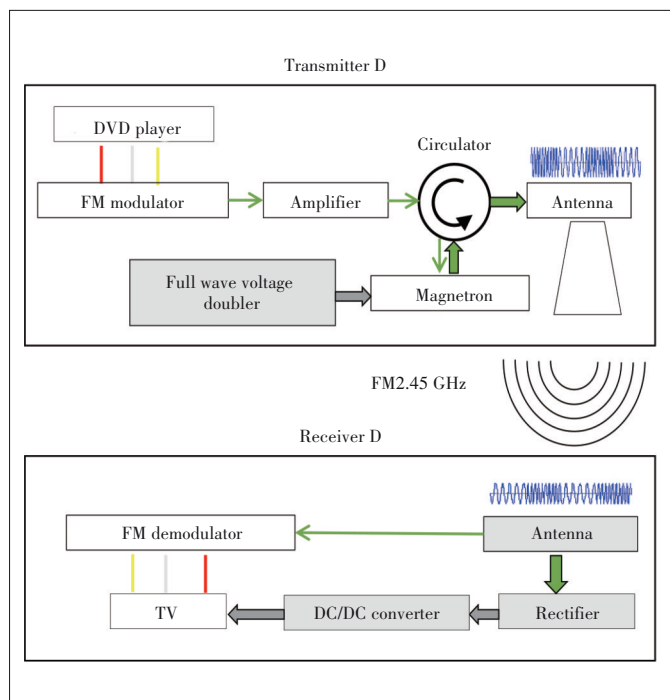


▲ Figure 10. Picture of TV broadcasting system using an injection-locked magnetron^[19]

This FM system using an injection-locked magnetron can be used in a TV broadcasting system. With digital TV becoming popular, the system may not have many applications. The system depicted in Figs. 9 and 10 demonstrate that injection-locked magnetrons can be used for low-speed audio and control signal transmissions and large-capacity data communications, such as those relating to video signals.

3.4 SWIPT System Used in Wirelessly Powered TV Broadcasting System

Based on the FM system used in the TV broadcasting system, a microwave-driven wireless TV system using the high-power WPT technology has been developed^[20]. Fig. 11 shows the diagram of the wirelessly powered TV system. The wire-



▲ Figure 11. Schematic of wirelessly powered TV system^[20]

lessly powered TV, comprising a 2.45 GHz band magnetron and a power supply, was developed based on the principle used in a microwave oven. The transmitter cost was not much different from the microwave oven cost. The system demonstrates the advantages of using injection-locked magnetrons for high-power SWIPT.

The noise produced by the magnetron depends on the stability of the power supply circuit and the temperature of the electron emission filament inside the magnetron^[33]. The magnetron used in the system is Panasonic 2M236-M42, which has an oscillation voltage of 3.60 kV. The power supply circuit used can oscillate continuously. The power supply circuits used in microwave ovens are based on half-wave double-voltage rectifiers. The magnetron output oscillates intermittently at 60 Hz. With the intermittent oscillation of the magnetron output, the magnetron oscillation frequency changes significantly because the fluctuation of the oscillation frequency of a magnetron depends on the anode current of the magnetron. Because the magnetron has a discontinuous output with its anode current changing drastically, the oscillation frequency of the magnetron also tends to change significantly. Thus, the noise in the microwave oven would be large. The conventional PCM uses a regulated DC power supply and reduces the magnetron noise by turning off the filament. However, when the filaments in microwave ovens using half-wave double-voltage rectifiers are turned off after the magnetrons start to oscillate, the electron emissions from the filaments will stop because of the discontinuous outputs, and oscillations will not occur. The output voltage has to be maintained above the oscillation voltage to make the magnetron produce an output continuously. In the system considered, a full-wave double-voltage rectifier is used. The output of the rectifier is higher than the magnetron oscillation voltage at a 4.16% ripple rate. The oscillation bandwidth is less than 3 MHz. The injection signal has a 2 MHz

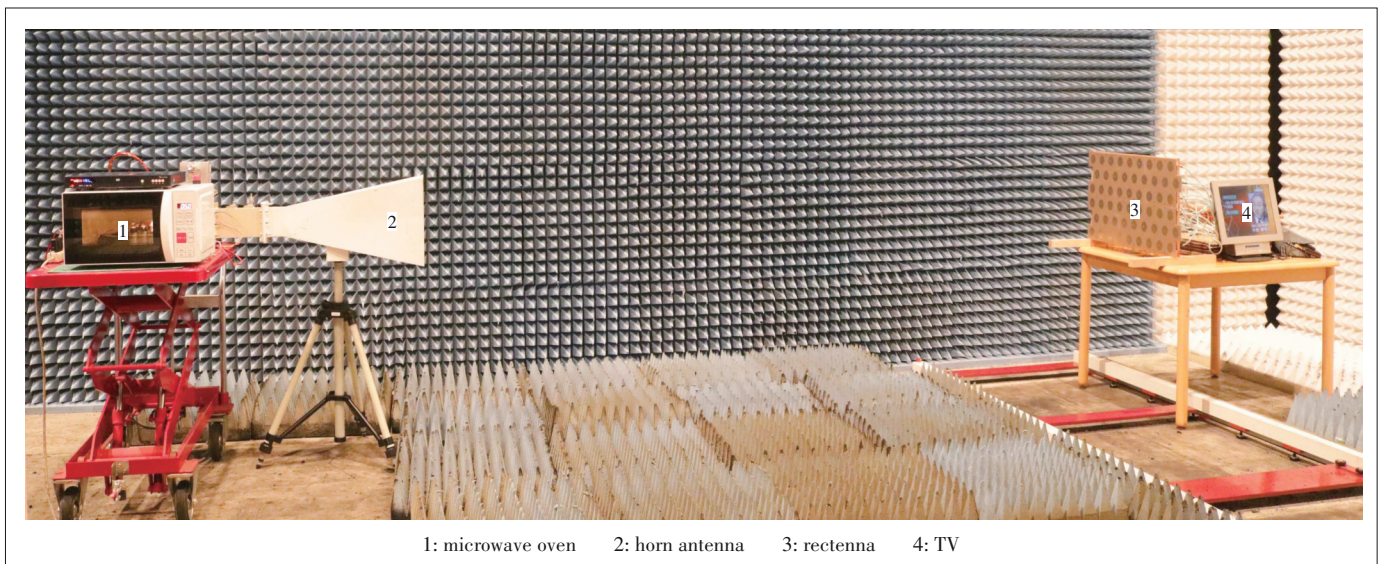
bandwidth. With 10 W injection power, the magnetron can work in the injection-locked state. The DVD signal is modulated and injected into the magnetron as in the TV broadcasting system. The magnetron produces a 329 W FM microwave for transmission to the receiver.

The receiver has 54 patch antennas with each antenna connected to a rectifier. The maximum rectifier efficiency is 51.7% at a 1.8 W input power and with a 60 Ω load. One rectifier circuit is connected to the demodulator, and the video and audio signals produced by the modulator are fed into the TV. The outputs of the other rectifier circuits are connected to a DC/DC converter. The distance between the transmitter and the receiver is 3.5 m, and the receiver is fed with 48 W of DC power, which is sufficient to drive the TV. The other relevant parameters of the system are shown in Table 2 and Fig. 12 shows a picture of the working wireless TV.

▼ **Table 2. Parameters of wirelessly powered TV^[20]**

Parameter	Value
Magnetron	2M236-M42 (Panasonic)
Anode current	140 mA
Anode voltage	-3.68 kV (DC)
Filament current	7.4 A
Filament voltage	3.35 V (AC 60Hz)
Injected power	10 W
Output frequency	2.448 - 2.450 GHz
Output power	329 W (RF)
Rectified power	48 W (DC)
Modulation	Frequency, modulation
Transmitter antenna	Gain 16 dBi (SPC)
TV	LL-M1550A (Sharp)

SPC: slotted polar cap



▲ **Figure 12. Picture of wirelessly powered TV^[20]**

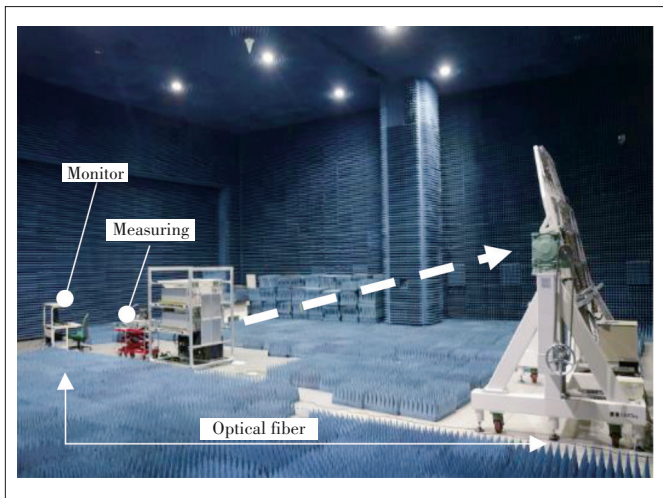
3.5 High-Power SWIPT System Used in Magnetron-Based Phased Array System

In a high-power WPT system, one magnetron is sufficient to supply the required energy. Based on the research conducted on PCM technology^[17], four injection-locked magnetrons are used to construct a 2×2 phased array system. The output power of the magnetron phased array can be controlled from 350 W to 1 637 W. As shown in Fig. 13, the phased array system transmits 1 304 W, and its receiver, which is at a 5 m distance from it, collects 142 W of DC power. The RF-RF-DC efficiency is close to 12%^[25]. By adjusting the phase of each PCM element, two-dimensional beamforming will be achieved.

In the SWIPT system shown in Fig. 14, the magnetron out-

puts a modulated signal. The effect of modulation on transmission efficiency is almost negligible. When measured at different modulation rates (1, 10, 100, and 1 000 kbit/s), the modulated beam is found to degrade the power received by less than 3%. Beamforming does not affect the modulation quality in WIT significantly. If the receiver power is sufficient for the demodulation level, communication quality will not change. The phase shifters are set for switching at 100 ms, which is close to the response time of the magnetron phased array. The magnetron phased array produces a dynamic beam at $\pm 2^\circ$. The EVMs of the dynamic and static beams are not much different. The EVMs measured in front of the magnetron phased array are similar. The EVMs are affected mainly by the received power level^[34].

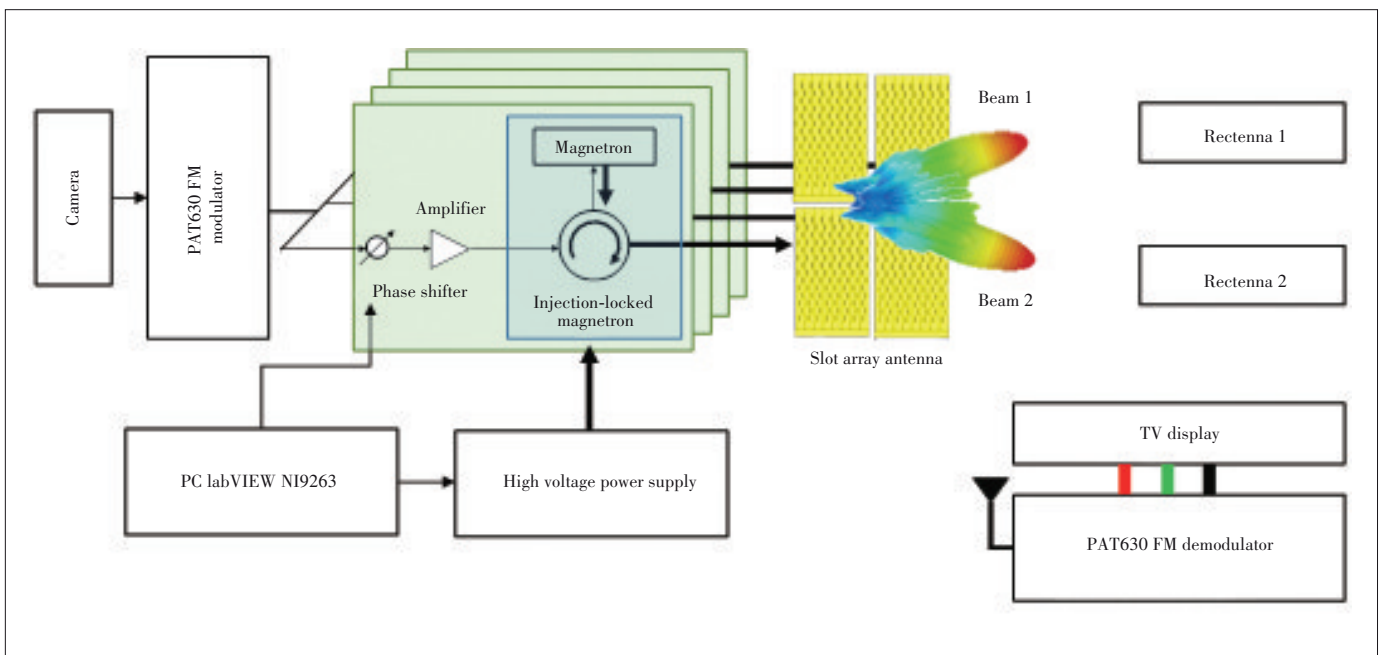
As shown in Figs. 14 and 15, the modulated video signal is used as the injection signal. When four PCMs are injected and locked with the same modulation wave, beamforming of the magnetron phased array can be achieved by adjusting the phase of each PCM. The magnetron phased array delivers microwave beam switching to Rectennas 1 and 2 every 2 seconds. At the same time, the TV displayed a stable camera signal. Experiments conducted have revealed that video transmission could be done with dynamic beamforming^[34]. The results show that the phased arrays transmitting a modulated signal and those producing the beam can coexist. In this high-power SWIPT, the main lobe power is used for WPT, and the side lobe is used for WIT, which is a novel method.



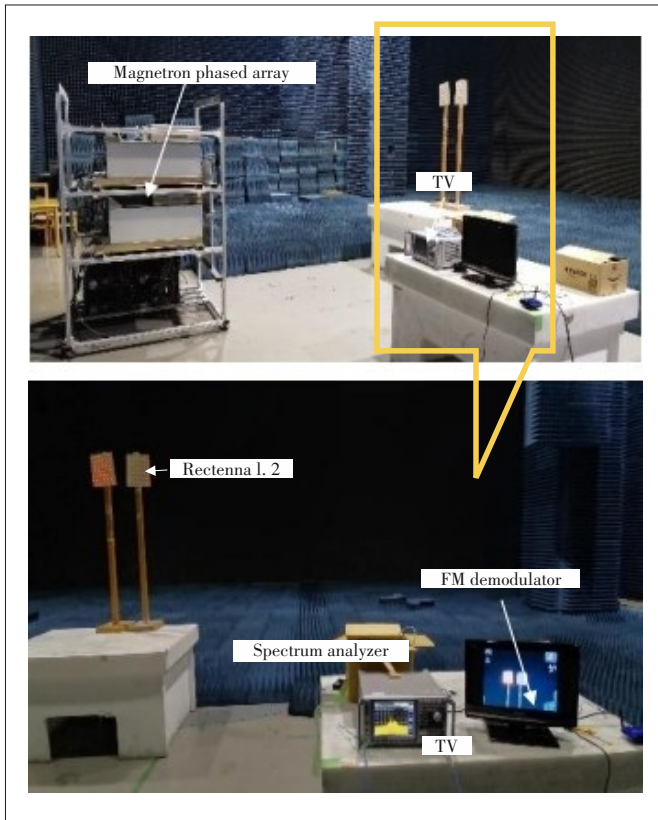
▲ Figure 13. Picture of 5.8 GHz magnetron-based phased array used in the wireless power transfer (WPT) experiment^[25]

4 Conclusions

This review summarizes the latest research findings on injection-locked magnetrons that can be used in high-power



▲ Figure 14. Schematic of high-power simultaneous wireless information and power transfer (SWIPT) system used by the magnetron phased array^[34]



▲ Figure 15. Picture of high-power simultaneous wireless information and power transfer (SWIPT) system used by the magnetron phased array^[34]

SWIPT. The performance of injection-locked magnetrons using amplitude, phase, and frequency modulation is evaluated. The highest data rate that could be achieved is 10 Mbit/s. These demonstration experiments of the injection-locked magnetron maintaining the high-power output have realized the modulated sound signal, motor control signal, and video signal. The wirelessly powered TV system that has been demonstrated uses a high-power SWIPT system. A high-power SWIPT used in a magnetron-based phased array, which transmits video using beam scanning, is also presented. The effects of beam scanning on signal quality and the modulated signal and on transmission efficiency are quantitatively evaluated. Technically, a practicable high-power SWIPT has been achieved.

However, in enabling the IoT and IoE society, many challenges will have to be overcome with the collaboration and cooperation of all industries. We have reviewed the latest developments of SWIPT that can be used with low-power devices and based on communication standards, such as 5G, Wi-Fi, and Bluetooth. The Japanese government is discussing WPT-related regulations, which would set the maximum power of the system as 32 W. The devices such as drones and electric vehicles require high power for charging. Currently, no standard on high-power SWIPT used via microwaves has been formulated through consensus. Another challenge is posed by

high-efficiency energy conversion technologies. The existing microwave power-amplifying devices used for communication have low conversion efficiency. Although magnetrons can perform high-efficiency conversions, their bandwidths are narrow, which does not permit high-speed communications. The traveling wave tube (TWT) has a wide bandwidth and efficient conversion capabilities. However, because of its high cost, TWT is being used mainly in satellite communications. Thus, we need to find a wide bandwidth energy conversion device that is inexpensive and highly efficient.

In the future, high-power SWIPT may be combined with 5G base stations and wireless routers. We can look forward to a future with wireless IoT and an IoE society where drones, mobile phones, and other devices operate wirelessly.

References

- [1] KRIKIDIS I, TIMOTHEOU S, NIKOLAOU S, et al. Simultaneous wireless information and power transfer in modern communication systems [J]. *IEEE communications magazine*, 2014, 52(11): 104 – 110. DOI: 10.1109/MCOM.2014.6957150
- [2] BOYD J. Here comes the wallet phone [wireless credit card] [J]. *IEEE spectrum*, 2005, 42(11): 12 – 14. DOI: 10.1109/MSPEC.2005.1526896
- [3] COSKUN V, OZDENIZCI B, OK K, et al. NFC loyal system on the cloud [C]// 7th International Conference on Application of Information and Communication Technologies. IEEE, 2013: 1 – 5. DOI: 10.1109/ICAICT.2013.6722637
- [4] KIM J, KIM D H, PARK Y J. Analysis of capacitive impedance matching networks for simultaneous wireless power transfer to multiple devices [J]. *IEEE transactions on industrial electronics*, 2015, 62(5): 2807 – 2813. DOI: 10.1109/TIE.2014.2365751
- [5] DAI J J, LUDOIS D C. A survey of wireless power transfer and a critical comparison of inductive and capacitive coupling for small gap applications [J]. *IEEE transactions on power electronics*, 2015, 30(11): 6017 – 6029. DOI: 10.1109/TPEL.2015.2415253
- [6] BOU-BALUST E, HU A P, ALARCON E. Scalability analysis of SIMO non-radiative resonant wireless power transfer systems based on circuit models [J]. *IEEE transactions on circuits and systems I: Regular papers*, 2015, 62(10): 2574 – 2583. DOI: 10.1109/TCSI.2015.2469015
- [7] CHABALKO M, BESNOFF J, LAIFENFELD M, et al. Resonantly coupled wireless power transfer for non-stationary loads with application in automotive environments [J]. *IEEE transactions on industrial electronics*, 2017, 64(1): 91 – 103. DOI: 10.1109/TIE.2016.2609379
- [8] ZHANG R, HO C K. MIMO broadcasting for simultaneous wireless information and power transfer [J]. *IEEE transactions on wireless communications*, 2013, 12(5): 1989 – 2001. DOI: 10.1109/TWC.2013.031813.120224
- [9] DING Z G, ZHONG C J, WING KWAN NG D, et al. Application of smart antenna technologies in simultaneous wireless information and power transfer [J]. *IEEE communications magazine*, 2015, 53(4): 86 – 93. DOI: 10.1109/MCOM.2015.7081080
- [10] CHOI K W, HWANG S I, AZIZ A A, et al. Simultaneous wireless information and power transfer (SWIPT) for Internet of Things: novel receiver design and experimental validation [J]. *IEEE Internet of Things journal*, 2020, 7(4): 2996 – 3012. DOI: 10.1109/JIOT.2020.2964302
- [11] GOLAM M, IGBOANUSI I S, LEE J M, et al. Reliable communication using orbital angular momentum with SWIPT for military networks [C]// International Conference on Information and Communication Technology Convergence (ICTC). IEEE, 2019: 636 – 638. DOI: 10.1109/ICTC46691.2019.8939759
- [12] MASE M, SHINOHARA N, MITANI T, et al. Evaluation of efficiency and iso-

- lation in wireless power transmission using orbital angular momentum modes [C]/IEEE Wireless Power Transfer Conference. IEEE, 2021: 1 – 4. DOI: 10.1109/WPTC51349.2021.9458043
- [13] SHINOHARA N. Wireless power transfer in Japan: Regulations and activities [C]/14th European Conference on Antennas and Propagation (EuCAP). IEEE, 2020: 1 – 4. DOI: 10.23919/EuCAP48036.2020.9135422
- [14] SHINOHARA N. History and innovation of wireless power transfer via microwaves [J]. IEEE journal of microwaves, 2021, 1(1): 218 – 228. DOI: 10.1109/JMW.2020.3030896
- [15] Energoous. Energoous receives FCC approval, extending charging zone to up to 1 meter for groundbreaking over-the-air, power-at-a-distance wireless charging [EB/OL]. [2021-12-10]. <https://ir.energoous.com/news-events/press-releases/detail/672/energoous-receives-fcc-approval-extending-charging-zone-to>
- [16] Global Banking & Finance Review. Ossia receives FCC authorization for its next generation platform for wireless power at a distance [EB/OL]. [2021-12-10]. <https://www.globalbankingandfinance.com/category/news/ossia-receives-fcc-authorization-for-its-next-generation-platform-for-wireless-power-at-a-distance/amp>
- [17] YANG B, MITANI T, SHINOHARA N. Experimental study on a 5.8 GHz power-variable phase-controlled magnetron [J]. IEICE transactions on electronics, 2017, E100.C(10): 901 – 907. DOI: 10.1587/transele.e100.c.901
- [18] TAHIR I, DEXTER A, CARTER R. Frequency and phase modulation performance of an injection-locked CW magnetron [J]. IEEE transactions on electron devices, 2006, 53(7): 1721 – 1729. DOI: 10.1109/TED.2006.876268
- [19] YANG B, MITANI T, SHINOHARA N. Evaluation of the modulation performance of injection-locked continuous-wave magnetrons [J]. IEEE transactions on electron devices, 2019, 66(1): 709 – 715. DOI: 10.1109/TED.2018.2877204
- [20] YANG B, MITANI T, SHINOHARA N. Injection-locked CW magnetron for a wirelessly-powered TV [C]/International Vacuum Electronics Conference (IVEC). IEEE, 2019: 1 – 2. DOI: 10.1109/IVEC.2019.8745010
- [21] SHINOHARA N, MATSUMOTO H, HASHIMOTO K. Phase-controlled magnetron development for SPORTS: space power radio transmission system [J]. URSI radio science bulletin, 2004, 2004(310): 29 – 35. DOI: 10.23919/URSIRSB.2004.7909435
- [22] SHINOHARA N, MITANI T, MATSUMOTO H. Development of phase and amplitude controlled magnetron [C]/6th International Vacuum Electronics Conference (IVEC). IEEE, 2005: 61 – 65
- [23] BROWN W C. The high signal to noise ratio of the microwave oven magnetron and evidence of a negative feedback loop to control it [C]/11st International Workshop Crossed-Field Devices. Defense Technical Information Center, 1995: 178 – 187
- [24] BROWN W C. Update on the solar power satellite transmitter design [J]. Space power, 1984, 6(2): 123 – 135
- [25] YANG B, CHEN X J, CHU J, et al. A 5.8-GHz phased array system using power-variable phase-controlled magnetrons for wireless power transfer [J]. IEEE transactions on microwave theory and techniques, 2020, 68(11): 4951 – 4959. DOI: 10.1109/TMTT.2020.3007187
- [26] MITANI T, SHINOHARA N, MATSUMOTO H. Development of a pulse-driven phase-controlled magnetron [C]/IEEE International Vacuum Electronics Conference. IEEE, 2007: 1 – 2. DOI: 10.1109/IVELEC.2007.4283396
- [27] ADLER R. A study of locking phenomena in oscillators [J]. Proceedings of the IEEE, 1973, 61(10): 1380 – 1385. DOI: 10.1109/PROC.1973.9292
- [28] Japan Electronics and Information Technology Industries Association Electro-tube History Study Group. History of electron tubes: the origin of electronics (in Japanese) [M]. Tokyo, Japan: Ohmsha, 1987: 166 – 169
- [29] WEGLEIN R D, LEACH H A. The noise behavior of an injection-locked magnetron reflection amplifier [C]/IEEE MTT-S International Microwave Symposium Digest. IEEE, 1987: 261 – 264. DOI: 10.1109/MWSYM.1987.1132379
- [30] TAHIR I, DEXTER A, CARTER R. Noise performance of frequency- and phase-locked CW magnetrons operated as current-controlled oscillators [J]. IEEE transactions on electron devices, 2005, 52(9): 2096 – 2103. DOI: 10.1109/TED.2005.854276
- [31] READ M, IVES R L, BUI T, et al. A 100-kW 1300-MHz magnetron with amplitude and phase control for accelerators [J]. IEEE transactions on plasma science, 2019, 47(9): 4268 – 4273. DOI: 10.1109/TPS.2019.2932264
- [32] YANG B, MITANI T, SHINOHARA N. Study on a 5.8GHz injection-locked magnetron for transferring data [C]/31st International Vacuum Nanoelectronics Conference (IVNC). IEEE, 2018: 1 – 2. DOI: 10.1109/IVNC.2018.8520193
- [33] MITANI T, SHINOHARA N, MATSUMOTO H, et al. Improvement of spurious noises generated from magnetrons driven by DC power supply after turning off filament current [J]. IEICE transactions on electron, 2003, E86-C(8): 1556 – 1563
- [34] YANG B, CHU J, MITANI T, et al. High-power simultaneous wireless information and power transfer system based on an injection-locked magnetron phased array [J]. IEEE microwave and wireless components letters, 2021, 31(12): 1327 – 1330. DOI: 10.1109/LMWC.2021.3104832

Biographies

YANG Bo (yang_bo@rish.kyoto-u.ac.jp) received the BE degree in electronic information engineering from China University of Petroleum (Qingdao), China in 2008, the ME and PhD degrees in electrical engineering from Kyoto University, Japan in 2018 and 2020. From 2019 to 2021, he conducted research on high-power wireless power transfer systems, supported by Research Fellowships for Young Scientists sponsored by the Japan Society for the Promotion of Science (JSPS). He is currently researching high-power microwave wireless power transmission at the Research Institute for Sustainable Humanosphere, Kyoto University. From 2008 to 2015, he was an RF engineer with the DAIHEN Group, China.

MITANI Tomohiko received the BE degree in electrical and electronic engineering, ME degree in informatics, and PhD degree in electrical engineering from Kyoto University, Japan in 1999, 2001, and 2006, respectively. In 2003, he was an assistant professor with the Radio Science Center for Space and Atmosphere, Kyoto University. Since 2012, he has been an associate professor with the Research Institute for Sustainable Humanosphere, Kyoto University. His current research interests include the experimental study of magnetrons, microwave power transmission systems, and applied microwave engineering. Dr. MITANI is a member of the Institute of Electronics, Information and Communication Engineers (IEICE) and the Japan Society of Electromagnetic Wave Energy Applications (JEMEA). He has been a board member of JEMEA since 2015. He was the treasurer of IEEE MTT-S Kansai Chapter from 2014 to 2021.

SHINOHARA Naoki received the BE degree in electronic engineering, and the ME and PhD degrees in electrical engineering from Kyoto University, Japan in 1991, 1993, and 1996, respectively. Since 1996, he has been with the Radio Atmospheric Science Center, Kyoto University, where he has been a research associate since 2000, an associate professor since 2001, and a professor since 2010. He was the founder and Advisory Committee member of IEEE Wireless Power Transfer Conference, the vice chair of URSI commission D, the executive editor of *International Journal of Wireless Power Transfer* (Cambridge Press), the first chair and Technical Committee member of IEICE Wireless Power Transfer, an adviser of Japan Society of Electromagnetic Wave Energy Applications, the vice chair of Space Solar Power Systems Society, the chair of Wireless Power Transfer Consortium for Practical Applications (WiPoT), and the chair of Wireless Power Management Consortium (WPMC).

ZHANG Huaqing received the BE, ME and PhD (Eng) degrees in electrical engineering from Chongqing University, China in 2000, 2003 and 2008, respectively. He joined the School of Electrical Engineering, Chongqing University as a research associate in 2003 and has been a professor since 2014. His research interests include microwave power transmission applications, power signal processing, and electromagnetic field theory and applications. He is a member of several special committees (Space Solar Power Station, Wireless Energy Transmission, and Electrical Theory and New Technology). He is vice president of the Electromagnetic Field Teaching and Textbook Research Association.

An Overview of SWIPT Circuits and Systems



Ricardo TORRES^{1,2}, Diogo MATOS^{1,2},
Felisberto PEREIRA^{2,5}, Ricardo CORREIA^{2,3,4},
Nuno Borges CARVALHO^{1,2}

(1. Department of Electronics, telecommunications and information, University of Aveiro, Aveiro 3810, Portugal;

2. Institute of Telecommunications, Aveiro 3800, Portugal;

3. CISED-Research Center in Digital Services, Polytechnic of Viseu, Viseu 3500, Portugal;

4. Sinuta SA., Estarreja 3860, Portugal;

5. AlmaScience Colab, Madan Parque, Caparica 2829-516, Portugal)

DOI: 10.12142/ZTECOM.202202003

<https://kns.cnki.net/kcms/detail/34.1294.TN.20220518.0925.002.html>,
published online May 19, 2022

Manuscript received: 2022-04-18

Abstract: From a circuit implementation perspective, this paper presents a brief overview of simultaneous wireless information and power transmission (SWIPT). By using zero-power batteryless wireless sensors, SWIPT mixes wireless power transmission with wireless communications to allow the truly practical implementation of the Internet of Things as well as many other applications. In this paper, technical backgrounds, problem formation, state-of-the-art solutions, circuit implementation examples, and system integrations of SWIPT are presented.

Keywords: simultaneous wireless information and power transmission (SWIPT) systems; backscatter communication; low power communication

Citation (IEEE Format): R. Torres, D. Matos, F. Pereira, et al., "An overview of SWIPT circuits and systems," *ZTE Communications*, vol. 20, no. 2, pp. 13 - 18, Jun. 2022. doi: 10.12142/ZTECOM.202202003.

1 Introduction

In addition to radio frequency (RF) waves' ability to transmit information, a viable energy source for powering low-power devices used in wireless sensor networks (WSN) or Internet of Things (IoT) applications should also be considered. The scientific community has explored this characteristic of radio waves, resulting in the proposal of a simultaneous wireless information and power transmission (SWIPT) system.

A careful design that incorporates wireless power transfer (WPT) capabilities should be considered to improve the devices' data storage or increase computing capabilities. This integration has facilitated the interest in the concept of passive wireless sensors, which may play an important role in an IoT scenario with sensors without batteries deployed everywhere sensing the environment. Nowadays, more IoT sensors bring the increase of batteries to be deployed, which will have a negative ambient impact. Battery-powered tags can improve communication distance but have limitations in

battery cost and replacement. Thus, the alternatives to the battery systems are based on the energy harvester (EH) technology or other different sources (solar^[1], motion or vibration^[2], and ambient RF^[3]). To overcome the problems from the EH and batteries, the concept of WPT has been explored to supply the tags with power.

In Ref. [4], a solution combining inductive WPT and ultra-high frequency (UHF) radio frequency identification (RFID) was presented, and by combining these two technologies it was possible to increase the tag sensitivity by 21 dB. However, with inductive WPT, the proximity of the tag to the power source is a huge obstacle to those systems, and to overcome the problem created by the short distance required in inductive wireless power transfer, electromagnetic wireless power transfer has emerged. It consists in using the power contained in RF waves and, through conditioning circuits such as RF to (direct current) DC converters, transforming this power into the current.

Regarding electromagnetic WPT, a comparison between different rectifier typologies and different stage levels was presented in Ref. [5]. The results show a high dependence between the received power and the most efficient topology. In Ref. [6], the authors presented a structure with a two-tone

This work is funded by FCT/MCTES through national funds and EU funds under the project UIDB/50008/2020-UIDP/50008/2020.

signal at 1.8 GHz and 2.4 GHz, which improved the voltage output by 20% higher on average than a single-tone input. The authors in Ref. [7] presented a reader which was configured to transmit power in continuous waves (CW). The tag used a storage capacitor that could charge up to 5.5 V after the rectification. After the storage capacitor was charged, it powered the tag that performed sensing and communication, reflecting the carrier wave. This process was proven at 1 m between the reader and the tag. The same principle was used in Ref. [8].

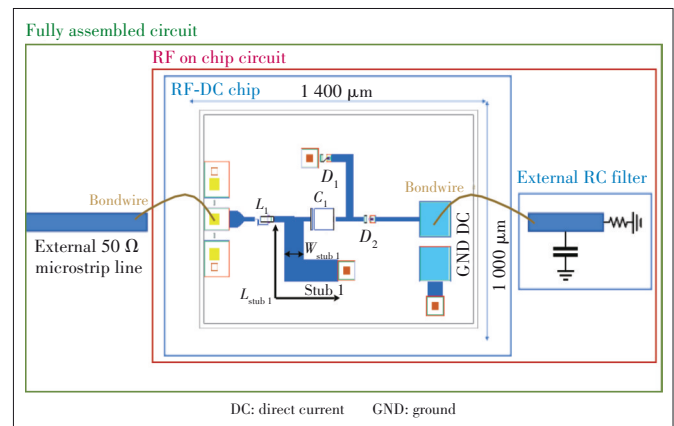
This paper describes the works presenting SWIPT systems or devices that are part of SWIPT systems, power conditioning circuits such as RF-DC converters, or backscatter communication circuits.

This paper is organized as follows. Section 2 presents some examples of work in the WPT area, Section 3 exposes backscatter communication systems, SWIPT systems are presented in Section 4, and the conclusions are drawn in Section 5.

2 Wireless Power Transfer Energy Harvesters

As mentioned previously, the increase of IoT devices raises the need for power and EH is a clean solution to that. Moreover, with new 5G bands (above 20 GHz), new opportunities emerge, due to the possibility of developing compact devices, using higher transmitted power, and using antenna arrays instead of single elements. Integrated circuits (IC) are also a solution to developing compact and quite cheap circuits, and Gallium Arsenide (GaAs) technology has evolved in recent years, making it a suitable technology for low-power systems.

In Ref. [9] the authors presented a hybrid solution combining an RF-DC converter chip, based on a 2-stage Dickson charge pump/voltage multiplier that was developed by resorting to a 100 μm GaAs technology foundry. In contrast to conventional circuits developed with IC technologies, the authors in Ref. [9] developed a DC low-pass filter externally to the chip, using a conventional microstrip substrate connected by bond wires, as shown in Fig. 1. The chip is composed of a matching network (values are shown in Fig. 1) that matches the input impedance to the diode's impedance. The external RC filter will allow tuning the circuit for different scenarios and frequencies. For example, when measuring the chip using a probe station, the RC network is not the same if the circuit is connected to an antenna, since the 50 Ω microstrip line and bond-wire would influence the chip response. This enables optimization of the circuit for different scenarios and different frequencies of operation. The substrate used is the Rogers RO4003C, with $\epsilon_r=3.48$ and $h=0.508$ mm. With this circuit, for the case of on-chip measurement, 51 % efficiency is achieved for an input power of 15 dBm. In the fully assembled prototype, some de-



▲ Figure 1. RF-DC block diagram circuit for different scenarios, where $L_1=0.12$ nH, $C_1=2.7$ pF, $L_{\text{stub}1}=372$ μm , $W_{\text{stub}1}=90$ μm , $W_{D1}=W_{D2}=10$ (N° of fingers), with the chip area of 1 400 $\mu\text{m} \times 1$ 000 μm ^[9]

viation is found, and the peak of efficiency appears at 23 GHz with efficiency of 54% and the input power of 13 dBm. Moreover, both circuits present promising results at other frequencies.

Using this approach, it is possible to power up a sensor even without the use of a battery pack, allowing the possibility of maximizing the service time of IoT sensors.

3 Wireless Information

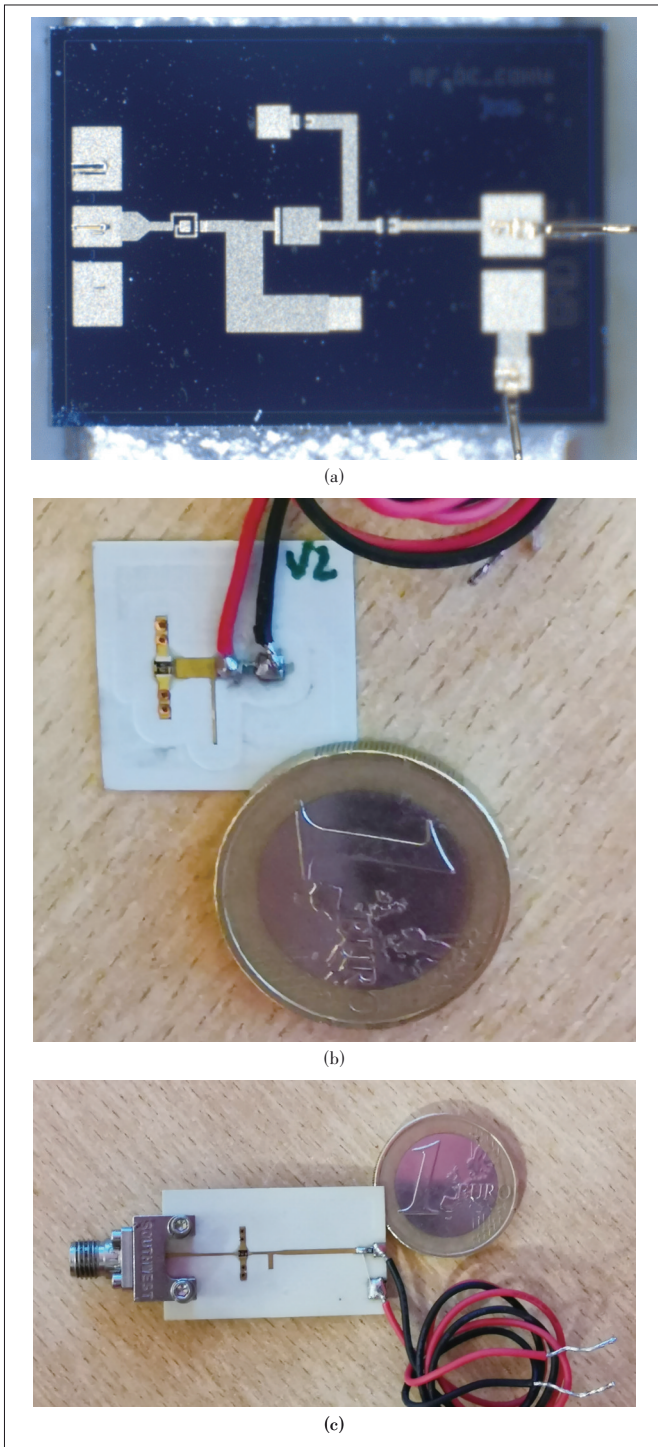
3.1 High Order Backscatter Communication

If the objective is to create an information layer on top of the power layer for the IoT sensors, the wireless communication layer should consume the minimum amount of energy possible. Traditional super-heterodyne approaches are not a viable solution in this scenario, since the energy cost is high for these approaches. One of the alternatives proposed by the authors in Ref. [10] is to use backscatter systems combined with WPT.

Backscatter systems are normally low bit-rate solutions, because they operate in amplitude shift keying, or binary phase shift keying modulation formats, creating different impedances at the antenna plane for the generation of such modulation schemes. Nevertheless, it is possible to combine some basic modulations to obtain better modulation formats for IoT applications, like the quadrature amplitude modulation (QAM) which combines the amplitude and phase modulation.

This technique uses the combination to change the antenna impedance, and each impedance will correspond to a symbol used to transmit the digital message. DASKALAKIS et al.^[11] presented a low-power sensor tag. The tag could create up to 4 different antenna impedances, modulate data using four-pulse amplitude modulation (PAM) to increase the transmitted bit rate, and send it to a low-cost software-defined radio (SDR) reader. The tag requires no batteries and is supplied with an energy harvester, consuming only 27 μW .

In Ref. [12], the authors presented a novel modulator that



▲ Figure 2. (a) Microscopic photograph of the chip, (b) on-chip scenario prototype, and (c) fully assembled circuit prototype^[9]

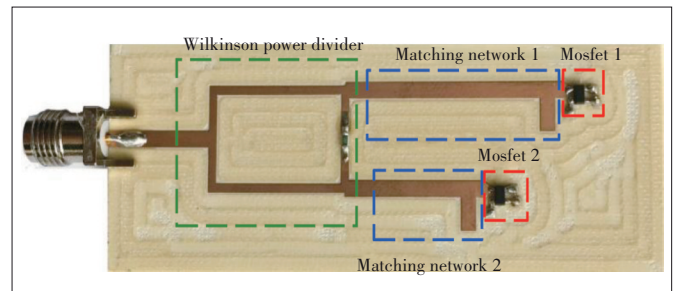
worked with a Wilkinson power divider with a phase shift and two transistors working as switches to generate M-QAM, as can be seen in Fig. 3. This modulation technique permits high-bandwidth and low-power wireless communications. The presented circuit has an energy consumption as low as 6.7 pJ/bit for a bit rate of 120 Mbit/s.

In Ref. [13], the authors implemented the same approach presented previously, but in this case, they used a 130 nm BiCMOS foundry technology. The objective was to achieve a low-power and high-speed M-QAM backscatter modulator for millimeter wave frequencies, as shown in Fig. 4. The authors showed that the modulator presented the lowest dynamic power consumption reported at the time, which was 6.96 μ W, and could achieve 16, 32, and 64-QAM modulations in a range of 20 GHz to 28 GHz with a low value of error vector magnitude (EVM).

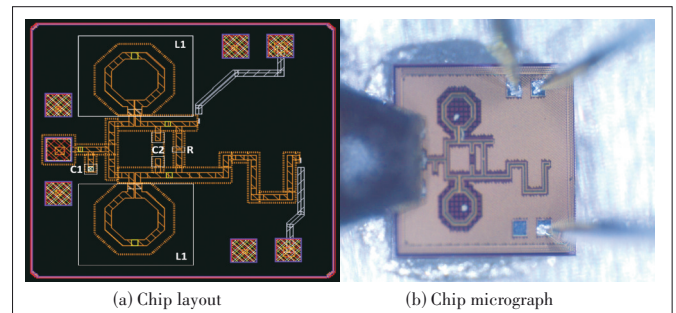
Moreover, backscatter could also be used with ambient electromagnetic waves, as in Ref. [14], which was based on the circuit of Ref. [13] and was possible to perform PAM modulation. In this case, the authors were interested in signal bands that are usually found on our daily basis, such as frequency modulation (FM)-100 MHz, industrial, scientific and medical (ISM)-400 MHz, digital video broadcasting-terrestrial (DVB-T)-700 MHz, or global system for mobile communications (GSM)-900 MHz. To demodulate the received signal, the authors have used a low-cost SDR that covers the bands of interest. The authors demonstrated that their system could demodulate signals in an extensive range of input power (-10 dBm to -60 dBm) and several data rate values (5 kbit/s to 50 kbit/s) in the mentioned frequencies.

3.2 All Digital Backscatter Communication

To minimize the costs of producing backscatter tags and increase the microcontroller unit (MCU) capability to receive and store data from the sensor networks, TORRES et



▲ Figure 3. Photograph of the 16-quadrature amplitude modulation (QAM) backscatter circuit^[12]



▲ Figure 4. BiCMOS high-order backscatter modulator, in which $C_1 = 385.117$ fF, $L_1 = 0.3$ nH, $C_2 = 30.012$ fF, $R = 100$ Ω , with the chip area of 0.92 mm²^[13]

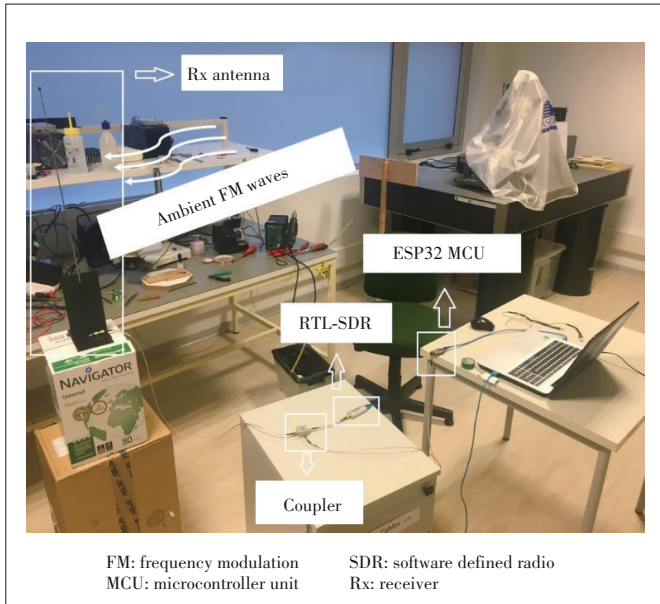
al.^[15] showed a fully digital ambient backscatter system that operates with ambient FM sources, with a power of approximately -70 dBm. In this system, the backscatter module uses an ESP32 MCU and a telescopic monopole as an antenna. The variation of a digital I/O pin causes an impedance variation in the connected antenna reflecting the incoming FM waves with an amplitude shift keying (ASK) modulation and can be demodulated by a low-cost RTL-SDR USB dongle, as shown in Fig. 5.

The solution presented enables a large number of applications that can benefit from the different technologies used with the commercial modules tested, such as Wi-Fi, Bluetooth, and ambient backscatter communications.

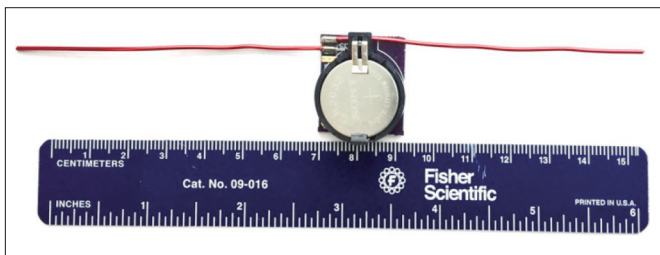
In Ref. [16], the authors produced a digital backscatter tag connecting a dipole, the two red wires in Fig. 6, to a digital I/O pin of the PIC16 MCU, presenting a digital backscatter tag.

4 SWIPT System

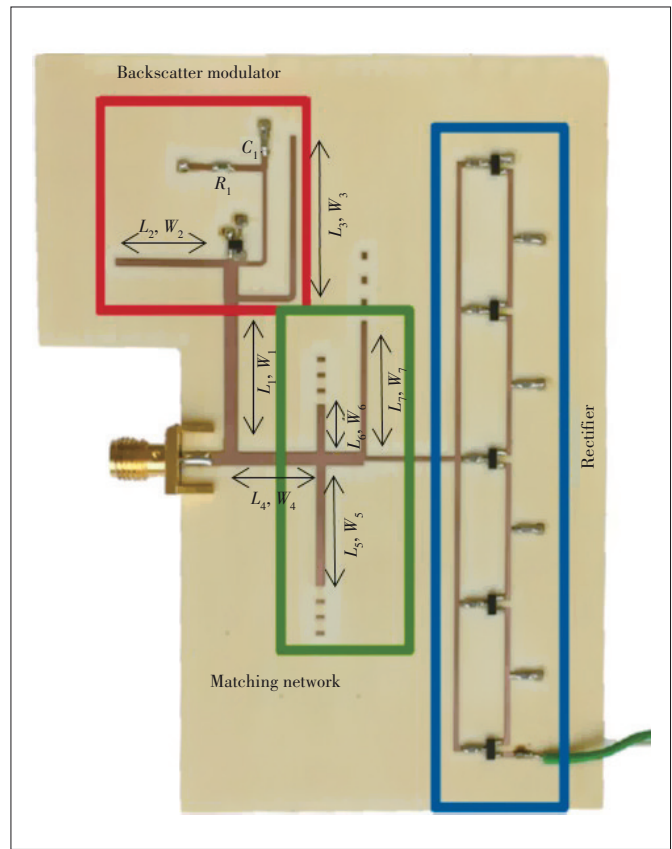
The authors in Refs. [10] and [17], as shown in Fig. 7, presented a solution using dual-band wireless power and data transfer, a system with a backscatter modulator combined with WPT. In this solution, two frequencies were consid-



▲ Figure 5. Real ambient FM measurements setup^[15]



▲ Figure 6. Photo of digital backscatter prototype^[16]



▲ Figure 7. Photograph of implemented system with backscatter modulator combined with wireless power transfer (WPT), element values of which are $L_1 = 21.2$ mm, $W_1 = 1.87$ mm, $L_2 = 15.1$ mm, $W_2 = 1.0$ mm, $L_3 = 21.9$ mm, $W_3 = 0.8$ mm, $L_4 = 11.3$ mm, $W_4 = 1.87$ mm, $L_5 = 17.1$ mm, $W_5 = 1.2$ mm, and $L_6 = 6.7$ mm^[17]

ered: one was used to power the tag and the other to perform the communication through backscatter. In this circuit, it is possible to find three main blocks. In the communications part, the red square in Fig. 7, the backscatter modulator will vary the impedance seen by the antenna, causing a reflection or absorption of the incident wave. The matching network is presented in green in Fig. 7, which is designed to provide backscatter load modulation at one frequency and continuous flow of WPT at other frequencies, and the five-stage Dickson multiplier provides sufficient DC power to supply the micro-controller. A similar approach, using different frequencies for energy and communication, was presented in Ref. [18], in which a different circuit for the RF-DC conversion was used for each frequency. The authors in Ref. [19] used two different frequencies for RF communication and WPT. They also used 5.8 GHz to power up a portion of radio connected to a battery with an RF-DC converter, and a wake-on radio (WOR) will only activate the battery for the primary transceiver. Nevertheless, the system is not passive and uses the WPT to activate the primary transceiver. Despite having passive tags for communication, it is of utmost importance to improve the data rate in the sensors in

order to reduce the power consumption and extend the read range.

5 Conclusions

In this paper, a brief review of SWIPT systems is presented, especially the combination of wireless power transmission and backscatter communications. The use of higher order modulation formats allows the implementation of such systems, reducing significantly the need for batteries in these sensors and paving the path for Internet of Everything in the future.

Acknowledgement:

Felisberto PEREIRA would like to thank to Lisboa 2020 Programme, Centro 2020 programme, Portugal 2020, European Union, through the European Social Fund who supported LISBOA-05-3559-FSE-000007 and CENTRO-04-3559-FSE-000094 operations as well as to Fundação para a Ciência e Tecnologia (FCT) and Agência Nacional de Inovação (ANI).

References

- [1] SAMPLE A, SMITH J R. Experimental results with two wireless power transfer systems [J]. 2009 IEEE radio and wireless symposium, 2009: 16 – 18. DOI: 10.1109/RWS.2009.4957273
- [2] ROUNDY S, WRIGHT P K, RABAEY J. A study of low level vibrations as a power source for wireless sensor nodes [J]. Computer Communications, 2003, 26(11): 1131 – 1144
- [3] SAMPLE A, SMITH J R. Experimental results with two wireless power transfer systems [C]//IEEE Radio & Wireless Symposium. IEEE, 2009:16 – 18
- [4] KRACEK J, ŠVANDA M, MAZANEK M, et al. Implantable semi-active UHF RFID tag with inductive wireless power transfer [J]. IEEE antennas and wireless propagation letters, 2016, 15: 1657 – 1660. DOI: 10.1109/LAWP.2016.2520663
- [5] BORGES L M, CHÁVEZ-SANTIAGO R, BARROCA N, et al. Radio-frequency energy harvesting for wearable sensors [J]. Healthcare technology letters, 2015, 2(1): 22 – 27. DOI: 10.1049/hlt.2014.0096
- [6] KUHN V, SEGUIN F, LAHUEC C, et al. A multi-tone RF energy harvester in body sensor area network context [C]//Proceedings of 2013 Loughborough Antennas & Propagation Conference (LAPC). IEEE, 2013: 238 – 241. DOI: 10.1109/LAPC.2013.6711891
- [7] YEAGER D J, HOLLEMAN J, PRASAD R, et al. NeuralWISP: A wirelessly powered neural interface with 1-m range [J]. IEEE transactions on biomedical circuits and systems, 2009, 3(6): 379 – 387. DOI: 10.1109/TBCAS.2009.2031628
- [8] SAMPLE A P, YEAGER D J, POWLEDGE P S, et al. Design of an RFID-based battery-free programmable sensing platform [J]. IEEE transactions on instrumentation and measurement, 2008, 57(11): 2608 – 2615. DOI: 10.1109/tim.2008.925019
- [9] MATOS D, CORREIA R, Carvalho N B. Millimeter-wave hybrid RF-DC converter based on a Gaas chip for IoT-WPT applications [J]. IEEE microwave and wireless components letters, 2021, 31(6): 787 – 790
- [10] CORREIA R, BORGES CARVALHO N, KAWASAKI S. Continuously power delivering for passive backscatter wireless sensor networks [J]. IEEE transactions on microwave theory and techniques, 2016, 64(11): 3723 – 3731. DOI: 10.1109/TMTT.2016.2603985
- [11] DASKALAKIS S N, CORREIA R, GOUSSETIS G. Four-PAM modulation of ambient FM backscattering for spectrally efficient low-power applications [J]. IEEE transactions on microwave theory and techniques, 2018, 66(12): 5909 – 5921
- [12] CORREIA R, CARVALHO N B. Ultrafast backscatter modulator with low-power consumption and wireless power transmission capabilities [J]. IEEE microwave and wireless components letters, 2017, 27(12): 1152 – 1154
- [13] MATOS D, DA CRUZ JORDÃO M D, CORREIA R, et al. Millimeter-wave BiCMOS backscatter modulator for 5 G-IoT applications [J]. IEEE microwave and wireless components letters, 2021, 31(2): 173 – 176. DOI: 10.1109/LMWC.2020.3042709
- [14] MATOS D, TORRES R, CORREIA R, et al. Ultra-wideband 4-PAM backscatter modulator based on BiCMOS technology for IoT/WPT applications [C]//Proceedings of 2021 IEEE Wireless Power Transfer Conference. IEEE, 2021: 1 – 4. DOI: 10.1109/WPTC51349.2021.9458113
- [15] TORRES R, CORREIA R, CARVALHO N B. All digital ambient backscatter system [C]//Proceedings of 2020 IEEE Wireless Power Transfer Conference. IEEE, 2020: 327 – 330. DOI: 10.1109/WPTC48563.2020.9295547
- [16] DADKHAH A, ROSENTHAL J, REYNOLDS M S. ZeroScatter: zero-added-component backscatter communication using existing digital I/O pins [C]//Proceedings of 2019 IEEE Topical Conference on Wireless Sensors and Sensor Networks (WiSNet). IEEE, 2019: 1 – 3. DOI: 10.1109/WISNET.2019.8711796
- [17] PEREIRA F, CORREIA R, CARVALHO N B. Passive sensors for long duration internet of things networks [J]. Sensors, 2017, 17(10). DOI: 10.3390/s17102268
- [18] JANKOWSKI-MIHUŁOWICZ P, WĘGLARSKI M. A method for measuring the radiation pattern of UHF RFID transponders [J]. Metrology and measurement systems, 2016, 23(2): 163 – 172. DOI: 10.1515/mms-2016-0018
- [19] LERDSITSOMBOON W, KENNETH O K. Technique for integration of a wireless switch in a 2.4 GHz single chip radio [J]. IEEE journal of solid-state circuits, 2011, 46(2): 368 – 377. DOI: 10.1109/JSSC.2010.2090089

Biographies

Ricardo TORRES (ricardo.torres@ua.pt) received the MS degree in electronics and telecommunications engineering in 2020 from University of Aveiro, Portugal, where he is currently working towards the PhD degree. He has been a researcher with Institute of Telecommunications, Portugal since 2019 and his main research interest include microwave electronic circuits, backscatter communication, and software-defined radio.

Diogo MATOS received the MS degree in electronics and telecommunications engineering in 2018 from the University of Aveiro, Portugal, where he is working toward the PhD degree. He was a hardware electrical design engineer in EVOLEO Technologies, Portugal. His current research interests include wireless power transfer, energy harvesting, wireless passive sensors for space applications, backscatter communications, and MMIC design. He is a member of the IEEE Microwave Theory and Techniques Society. He is also a reviewer of *IEEE Transactions on Microwave Theory and Techniques*.

Felisberto PEREIRA received the MS and PhD degrees in electrical engineering from University of Aveiro, Portugal, in 2017 and 2021, respectively. Currently he works as a senior researcher at Almascience, Portugal, a company focused on paper electronics. From 2017 to 2021 he was a researcher at Institute of Telecommunications, Portugal. His research interests include the areas of

sensors, energy harvesting and backscatter communications. PEREIRA published more than 15 scientific works, including five publications in peer-reviewed international journals. He also won three awards in international conferences regarding wireless power transfer and backscatter technologies.

Ricardo CORREIA received the MS degree in electronics and telecommunications engineering from the University of Aveiro, Portugal in 2009, and the PhD degree in electrical engineering at University of Aveiro, Portugal in 2019. He was an automation and electrical engineer and a researcher in embedded systems and signal processing. He is currently a researcher at Sinuta SA, Portugal, where he works on the transmission and reception system of electronically oriented signals for next generation satellite constellations. He is also a collaborator at the Institute of Telecommunications, University of Aveiro. His current research interests include wireless power transfer, energy harvesting, wireless passive sensors for space applications, and low power communications. Mr. CORREIA is a member of the IEEE Microwave Theory and Techniques Society. He is also a reviewer for the *IET Microwaves, Antennas and Propagation*, *Wireless Power Transfer Journal* and the *IEEE Transactions on Microwave Theory and Techniques*. He was a recipient of the 2016 URSI/ANACOM Prize awarded by the URSI Portuguese Section and Portuguese National Authority of Communications. He won the second prize in the PhD category of 2019 Fraunhofer Portugal challenge.

Nuno Borges CARVALHO received the doctoral degree in electronics and telecommunications engineering from the University of Aveiro, Portugal in

2000, respectively. He is currently a full professor and a senior research scientist with the Institute of Telecommunications, University of Aveiro and an IEEE Fellow. He coauthored *Intermodulation in Microwave and Wireless Circuits* (Artech House, 2003), *Microwave and Wireless Measurement Techniques* (Cambridge University Press, 2013), *White Space Communication Technologies* (Cambridge University Press, 2014), and *Wireless Power Transmission for Sustainable Electronics* (Wiley, 2020). He has been a reviewer and author of over 200 papers in magazines and conferences. He is the editor in chief of the *Cambridge Wireless Power Transfer Journal*, an associate editor of the *IEEE Microwave Magazine* and former associate editor of the *IEEE Transactions on Microwave Theory and Techniques* and *IET Microwaves Antennas and Propagation Journal*. He is the co-inventor of six patents. His main research interests include software-defined radio front-ends, wireless power transmission, nonlinear distortion analysis in microwave/wireless circuits and systems, and measurement of nonlinear phenomena. He has recently been involved in the design of dedicated radios and systems for newly emerging wireless technologies. Dr. CARVALHO is a member of the IEEE MTT ADCOM, the past-chair of the IEEE Portuguese Section, MTT-20 and MTT-11 and the member of the technical committees, MTT-24 and MTT-26. He is also the Chair of the URSI Commission A (Metrology Group). He was the recipient of the 1995 University of Aveiro and the Portuguese Engineering Association Prize for the best 1995 student at the University of Aveiro, the 1998 Student Paper Competition (Third Place) of the IEEE Microwave Theory and Techniques Society (IEEE MTTS) International Microwave Symposium (IMS), and the 2000 IEEE Measurement Prize. He is a distinguished lecturer for the RFID-council and was a distinguished microwave lecturer for the IEEE Microwave Theory and Techniques Society. In 2022 he is the IEEE-MTT President-Elect.



Optimal Design of Wireless Power Transmission Systems Using Antenna Arrays

SUN Shuyi, WEN Geyi

(Research Center of Applied Electromagnetics, Nanjing University of Information Science and Technology, Nanjing 210044, China)

DOI: 10.12142/ZTECOM.202202004

<https://kns.cnki.net/kcms/detail/34.1294.TN.20220429.2114.002.html>, published online May 5, 2022

Manuscript received: 2022-04-18

Abstract: Three design methods for wireless power transmission (WPT) systems using antenna arrays have been investigated. The three methods, corresponding to three common application scenarios of WPT systems, are based on the method of maximum power transmission efficiency (MMPTE) between two antenna arrays. They are unconstrained MMPTE, weighted MMPTE, and constrained MMPTE. To demonstrate the optimal design process with the three methods, a WPT system operating at 2.45 GHz is designed, simulated, and fabricated, in which the transmitting (Tx) array, consisting of 36 microstrip patch elements, is configured as a square and the receiving (Rx) array, consisting of 5 patch elements, is configured as an L shape. The power transmission efficiency (PTE) is then maximized for the three application scenarios, which yields the maximum possible PTEs and the optimized distributions of excitations for both Tx and Rx arrays. The feeding networks are then built based on the optimized distributions of excitations. Simulations and experiments reveal that the unconstrained MMPTE, which corresponds to the application scenario where no radiation pattern shaping is involved, yields the highest PTE. The next highest PTE belongs to the weighted MMPTE, where the power levels at all the receiving elements are imposed to be equal. The constrained MMPTE has the lowest PTE, corresponding to the scenario in which the radiated power pattern is assumed to be flat along with the Rx array.

Keywords: wireless power transmission system; antenna arrays; antenna pattern synthesis; feeding network

Citation (IEEE Format): S. Y. Sun and G. Y. Wen, "Optimal design of wireless power transmission systems using antenna arrays," *ZTE Communications*, vol. 20, no. 2, pp. 19 – 27, Jun. 2022. doi: 10.12142/ZTECOM.202202004.

1 Introduction

The wireless power transmission (WPT) can be traced back to the experiment demonstrated by Nicola TESLA using Hertz's theory of radio wave transmission^[1]. During the last decades, the application of WPT technology has been extended to various fields such as the solar power satellite, microwave hyperthermia, implantable devices and electric vehicles^[2-3]. The WPT systems are usually divided into two categories. One is to use the magnetic induction, for example, two closely spaced coils respectively used as transmitting (Tx) and receiving (Rx); the other is to use two antennas located in the near- or far-field region of each other^[4-8].

Many efforts have been devoted to enhancing the power transmission efficiency (PTE) for WPT systems and various design criteria have been proposed. Very recently, LI et al. proposed several methods for the design of antenna arrays for a microwave WPT system^[9-10]. In Ref. [9], a clustering method named the k -means algorithm was adopted to determine the optimal subarray configuration which yields the maximum beam collection efficiency (BCE). GOWDA et al. demon-

strated a WPT system using two patch antenna arrays^[11]. The excitations of the Tx array are assumed to be equal in amplitude and their phases are properly controlled in order to focus the field at the target plane. The Rx array is designed with dimensions slightly larger than the area of -3 dB region in order to intercept the incident fields while the feeding network for the Rx array is designed with a uniform distribution for both amplitudes and phases. In fact, most previous publications have focused on improving the PTE by adjusting the excitations of the Tx array and ignoring the design of Rx feeding networks. The Rx array is usually connected to a feeding network with a uniform distribution of excitations and the received power is collected at the feeding point^[12]. Metamaterial, substrate integrated waveguide, and spatial light modulators have also been used in near field multi-target focusing and shaping in complex media^[13-15]. Algorithms have also been investigated for near-field applications, such as time reversal, phase conjunction, the steepest descent method, Bayesian compressive sensing, and convex optimization^[16-18].

Most previous design methods for WPT systems have been demonstrated to be effective. In order to evaluate these methods, a performance index is needed to characterize the WPT systems. Examining all the wireless systems for either information or power transmission, their design has the ultimate goal

This project is supported by the National Natural Science Foundation of China under Grant No. 61971231.

to maximize the PTE between the Tx and Rx antennas. For this reason, the PTE is made for a performance index to evaluate all the wireless systems. In fact, the PTE may be used as a performance index for all antenna designs. One can make use of the PTE as an objective function to be optimized to design various antenna arrays and WPT systems, and such an optimization process has been referred to as the method of maximum power transmission efficiency (MMPTE)^[19-35]. For example, a WPT system using a 6×6 patch array as the Tx array and a 4×4 patch array as the Rx array was investigated in Ref. [24], where both the Tx and Rx arrays are optimally designed in terms of MMPTE. The measured PTE reaches 39.4% for a separation distance of 40 cm, which is much higher than a similar design reported in Ref. [11]. Recently, the MMPTE has further been applied to the design of antenna arrays to achieve a flat-top beam in both near- and far-field regions by introducing a constraint to MMPTE so that the power distribution along with the Rx elements is the same. In this case, one needs to solve a quadratically constrained quadratic program (QCQP) problem. By linearizing the QCQP, an analytical solution to the optimal distribution of excitations can be obtained. Based on this procedure, a radio frequency identification (RFID) bookshelf reader antenna array and an RFID antenna array used to track the servers placed in a metal cabinet have been proposed^[34-35]. Both antenna arrays can generate a wide and flat electric field intensity distribution in the near-field region and a complicated environment, with a fluctuation of less than 3 dB across the whole shelf, which is much better than previously reported results. A method for adjusting the distribution of the end-fire gains in the far-field region of the bidirectional antenna array has also been proposed by introducing a weighting diagonal matrix into the MMPTE^[31], where higher gain could be achieved with a smaller array size compared with other similar designs.

Therefore, there have been three different formulations of MMPTE, developed for the design of various antenna arrays. In this paper, the above three formulations will be applied to the design of WPT systems which correspond to three different practical scenarios. The MMPTE, free of weighting coefficients or constraints, will be referred to as unconstrained MMPTE and can be applied to the scenario where the power is transmitted between two antenna arrays without pattern shaping. The MMPTE with a weighting matrix will be referred to as the weighted MMPTE and is suitable for the application where the power levels are required to be different among the receiving elements. The MMPTE with constraints will be referred to as constrained MMPTE and can be applied to the scenario where the radiation pattern must be flat along the receiving antenna elements, e. g., several closely spaced identical electronic devices are wirelessly powered. For ease of comparison, the three methods will be applied to the design of the same WPT system operating at 2.45 GHz, in which the Tx array consists of 36 patch elements and is configured as a square, and

the Rx array consists of 5 patch elements and is configured as an L shape. The Tx and Rx arrays are separated by a distance of 15 cm. The three methods yield three feeding schemes for both Tx and Rx arrays, corresponding to three different application scenarios.

The paper is organized as follows. Section 2 introduces the general power transmission formula between two antennas. Section 3 discusses the three different formulations of MMPTE, which are dedicated to the design of WPT systems. Section 4 describes the design of the aforementioned WPT system, including the selection of antenna elements, the array configurations, the determination of the optimal distribution of excitations, and the design of feeding networks. Section 5 demonstrates the simulation and experimental results, including the near-field patterns and the realized PTEs for the three different designs. Some conclusions are drawn in Section 6.

2 General Power Transmission Formula for Two Antennas

Consider a power transmission system consisting of antennas 1 and 2. Let S_i ($i = 1, 2$) denote the closed surface that encloses antenna i only. When antenna 1 is transmitting and antenna 2 is receiving, the PTE, defined by the ratio of the power received by antenna 2 to the transmitting power of antenna 1^[19-20], is given by

$$\text{PTE} = \frac{\left| \int_{S_1 \text{ or } S_2} (\mathbf{E}_1 \times \mathbf{H}_2 - \mathbf{E}_2 \times \mathbf{H}_1) \cdot \mathbf{u}_n dS \right|^2}{4 \text{Re} \int_{S_1} (\mathbf{E}_1 \times \bar{\mathbf{H}}_1) \cdot \mathbf{u}_n dS \text{Re} \int_{S_2} (\mathbf{E}_2 \times \bar{\mathbf{H}}_2) \cdot \mathbf{u}_n dS}, \quad (1)$$

where \mathbf{u}_n is unit outward normal to the surface, and \mathbf{E}_i and \mathbf{H}_i denote the fields generated by antenna i when antenna j ($j \neq i$) is receiving. The PTE reaches the maximum if the following conjugate matching condition, $\mathbf{E}_1 = \bar{\mathbf{E}}_2$ and $\mathbf{H}_1 = -\bar{\mathbf{H}}_2$, is satisfied, on a closed surface that encloses either antenna 1 or 2. For a WPT system consisting of two planar apertures of regular shapes, the optimization of Eq. (1) yields an eigenvalue equation that can be solved analytically. The eigenvectors of the eigenvalue equation are the optimized aperture field distributions while the corresponding eigenvalues give the PTE^[36-39]. For two circular apertures of radius R_1 and R_2 separated by a distance D , a key parameter in the design of the WPT system is (the ratio of two areas)

$$C = \frac{R_1 R_2}{\lambda D}, \quad (2)$$

where λ is the wavelength. It shows that the PTE increases and approaches 100% as C goes up. Given the requirements of PTE, the transmission distance D , and the operating frequency, one can use Eq. (2) to determine the minimum aper-

ture sizes to meet the requirements.

The optimized aperture field distribution after optimizing Eq. (1) is a continuous function with a spherical phase distribution and a Gaussian-like amplitude distribution. Physically this implies that the Tx and Rx antennas must focus on each other, which is only possible when the Tx and Rx antennas are in the Fresnel region of each other.

3 MMPTE for Design of WPT Systems Using Antenna Arrays

In practice, it is challenging to achieve a continuous aperture field distribution with a single antenna aperture. One possible strategy for addressing the challenge is to approximate the continuous aperture field distribution using an antenna array. The aperture is first discretized into a number of elements, each of which is then replaced by an antenna element. The aperture field may be discretized so that its value over each element is considered a constant and is then used to feed the corresponding antenna element. Such an approach is, however, problematic since the mutual coupling among the antenna elements may cause severe distortion in the radiated field.

Instead of realizing a continuous aperture field distribution via an antenna array, one can directly consider the power transmission between two antenna arrays. The theory of MMPTE between two antenna arrays was first proposed by one of the authors in Ref. [19] in 2010, and has evolved into a powerful and universal method for the design of various antenna arrays during the last decade^[20-35]. The basic idea behind the MMPTE relies on the recognition that all wireless systems for both information and power transmission have to be optimally designed in the sense that the PTE between Tx and Rx has to be maximized (or minimized if no coupling is allowed between Tx and Rx). Therefore, by properly introducing a test receiving antenna array, the optimal design of antenna arrays reduces to the optimal design of WPT systems, and the best possible antenna performance is thus guaranteed.

A WPT system consists of m Tx antenna elements and n Rx antenna elements, which forms an $(m+n)$ -port network enclosed by the small dotted rectangle in Fig. 1, and it can be characterized by the scattering parameters as follows

$$\begin{bmatrix} [b_t] \\ [b_r] \end{bmatrix} = \begin{bmatrix} [S_{tt}] & [S_{tr}] \\ [S_{rt}] & [S_{rr}] \end{bmatrix} \begin{bmatrix} [a_t] \\ [a_r] \end{bmatrix}, \quad (3)$$

where the subscript t and r respectively stand for Tx and Rx, and

$$\begin{aligned} [a_t] &= [a_1, a_2, \dots, a_m]^T, \\ [a_r] &= [a_{m+1}, a_{m+2}, \dots, a_{m+n}]^T, \\ [b_t] &= [b_1, b_2, \dots, b_m]^T, \\ [b_r] &= [b_{m+1}, b_{m+2}, \dots, b_{m+n}]^T, \end{aligned} \quad (4)$$

respectively denote the normalized incident and reflected waves for the Tx array and the Rx array. The PTE, denoted by T , between Tx and Rx arrays is defined as the ratio of the total power delivered to the Rx array to the input power into the Tx array. Assuming that both the Tx and Rx arrays are well matched (a general discussion for a non-matched system can be found in Ref. [21]), we have^[19-21]:

$$T = \frac{[a_t]^H [A] [a_t]}{[a_t]^H [a_t]}, \quad (5)$$

where $[A] = [S_{rt}]^H [S_{rt}]$ is a matrix determined by the scattering parameters of the whole system and the superscript H denotes the Hermitian operation.

3.1 Unconstrained MMPTE

When the PTE defined by Eq. (5) is required to be stationary, an eigenvalue equation can be obtained as follows^[19-20]

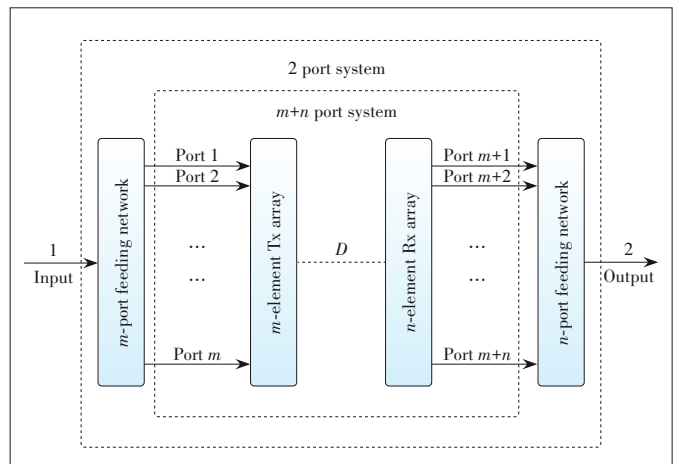
$$[A] [a_t] = T [a_t], \quad (6)$$

where the largest eigenvalue gives the maximum PTE, and the corresponding eigenvector $[a_t]$ gives the optimal distribution of excitations for the Tx array. Once the optimal distribution of excitations for the Tx array is known, the optimal distribution of excitations for the Rx array is then given by

$$[b_r] = [S_{rt}] [a_t]. \quad (7)$$

The above procedure does not involve any constraint and is therefore referred to as unconstrained MMPTE (UMMPTE). With one test receiving antenna placed in the direction where the radiation intensity needs to be maximized or minimized, the UMMPTE can be used to design focused antennas^[22-26], smart antennas^[27-30], and end-fire antennas^[31].

It can be shown that the optimized distribution of excitations obtained from Eq. (6) becomes uniformly distributed in



▲ Figure 1. Equivalent network

both amplitude and phase if the Tx and Rx arrays are in the far-field region of each other. In order to avoid this trivial case, one must properly select the aperture size for both Tx and Rx arrays so that they are in the Fresnel region of each other.

3.2 Weighted MMPTE

The second formulation of the MMPTE introduces a weighting matrix $[W] = \text{diag}(w_1, w_2, \dots, w_n)$ to achieve a prescribed power distribution among the Rx elements in the near- or far-field region. In this case, the received power distribution by the Rx elements is modified by the weighting matrix as follows

$$[b'_r] = [W][b_{m+1}, b_{m+2}, \dots, b_{m+n}]^T = [w_1 b_{m+1}, w_2 b_{m+2}, \dots, w_n b_{m+n}]^T. \quad (8)$$

Replacing $[b_r]$ in Eq. (4) with $[b'_r]$ and following the same procedure as UMMPTTE, we obtain the distribution of excitations for the Tx array, which will generate the desired power distribution among the Rx elements as prescribed by the weighting matrix $[W]$. The above procedure is called weighted MMPTE (WMMPTTE). For example, the weighting matrix can be properly selected so that the power levels at all the receiving elements are identical.

$$|w_1 b_{m+1}| = |w_2 b_{m+2}| = \dots = |w_n b_{m+n}|. \quad (9)$$

The optimal distribution of excitations for the Rx array is then given by

$$[b'_r] = [W][S_{rr}][a_t]. \quad (10)$$

By adjusting the weighting matrix $[W]$, the radiation pattern can also be shaped according to a prescribed manner. For example, the WMMPTTE can be used to design multiple beam antennas^[31].

3.3 Constrained MMPTE

A constraint can also be introduced to MMPTE to realize the desired field pattern in the near- or far-field region. In this case, one needs to solve a QCQP problem. For example, in order to achieve a uniform electric field distribution along with the Rx elements, the PTE can be maximized with the following constraints

$$|b_{m+1}| = |b_{m+2}| = \dots = |b_{m+n}|, \quad (11)$$

which guarantees that the radiated field from the Tx array is equally distributed along with the Rx array elements. We also introduce an n -dimensional weighting diagonal matrix $[W]$. Then the following equivalent normalized quadratic optimization problem with linear constraints can be obtained:

$$\begin{aligned} & \max [a_t]^H [A][a_t], \\ & \text{s.t. } [S_{rr}][a_t] = [W][y], \end{aligned} \quad (12)$$

where $[y]$ represents an n -dimensional vector, the element value of which is a constant. By using the method of Lagrange multiplier, the optimized distribution of excitations can be obtained as follows^[35]:

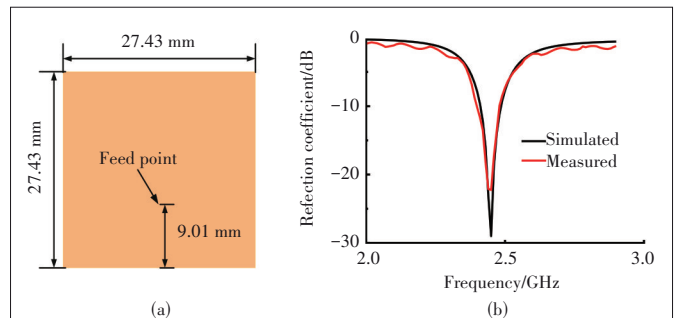
$$[a_t] = [A]^{-1}[S_{rr}]^H([S_{rr}][A]^{-1}[S_{rr}]^H)^{-1}[W][y]. \quad (13)$$

The optimal distribution of excitations for the Rx array is given by Eq. (7). The constrained MMPTE (CMMPTTE) can be used to shape radiation patterns in various complicated environments^[34-35].

4 Design of WPT Systems

The UMMPTTE, WMMPTTE, and CMMPTTE are naturally applicable to the design of WPT systems, and they are all optimal in a certain sense and correspond to three different application scenarios of WPT systems as mentioned above. The three optimization methods will now be applied to the design of the same WPT system so that a comparison can be easily made. As shown in Fig. 2(a), the antenna element used for both Tx and Rx arrays is a coaxial-fed square patch. The reflection coefficient of the patch element is shown in Fig. 2(b), and the antenna element is resonant at 2.45 GHz. As illustrated in Fig. 3, the Tx array consists of 36 elements, equally spaced with a separation of 0.5λ (λ is the wavelength of 2.45 GHz in free space) and arranged as a square shape and built on a 3 mm-thick FR4 substrate (relative permittivity of $\epsilon_r = 4.4$, and loss tangent of 0.02). The Rx array consists of 5 elements, arranged as an L shape with a separation distance of 1.25λ and also built on a 3 mm-thick FR4. Here an L shape for Rx array is purposely selected so that its elements are off the center line of the Tx array to make the design more challenging. The separation between the Tx and Rx arrays is 15 cm. After including the feeding systems, the (36+5)-port power transmission system can be considered a two-port network enclosed by the large dotted square in Fig. 1.

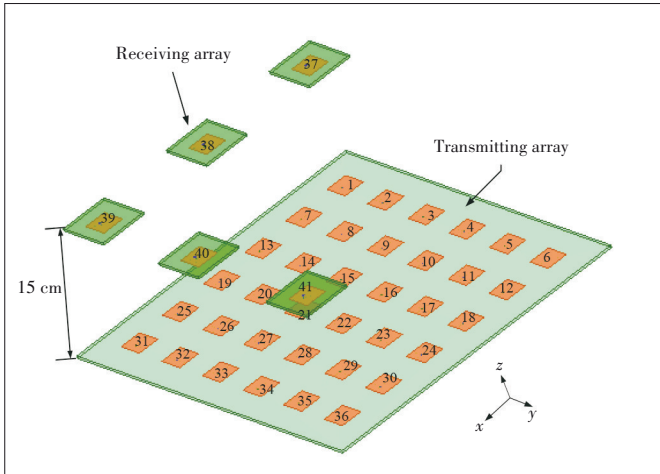
Once the WPT system is set up, the scattering parameters



▲ Figure 2. (a) Element of antenna arrays and (b) simulated and measured reflection coefficient of the Tx array

for the (36+5)-port network can be obtained either by simulation or by measurement. In this paper, the simulation tool Ansys HFSS is used to determine the network parameters. For ease of comparison, three application scenarios are considered. The first scenario corresponds to UMMPTe, where no pattern shaping is required on the Rx side. The second scenario corresponds to WMMPTe, where the received power levels at the Rx elements are constrained to be identical. The third scenario corresponds to CMMPTe, where the radiated field pattern along with the Rx array is constrained to be flat. For WMMPTe and CMMPTe, a weighting matrix $[W]$ is introduced and adjusted to ensure that the constraints are achieved. For the WPT system shown in Fig. 3, the weights for WMMPTe and CMMPTe are listed in Table 1.

The optimized distributions of excitations for the Rx and Tx arrays in the three application scenarios can be obtained from Eqs. (5) – (8), and are listed in Tables 2 and 3 respectively. It can be seen from Table 2 that the optimized distribution of excitations for Rx arrays obtained from WMMPTe and CMMPTe has a uniform amplitude distribution, and the phase distribution for CMMPTe is also uniform. The three feeding networks for the Rx arrays can be built from Table 2, and they are illustrated in Fig. 4. Based on Table 3, the three feeding networks for Tx arrays can be built and are illustrated in Fig. 5. All the feeding



▲ Figure 3. Wireless power transmission (WPT) system

▼ Table 1. Weights for CMMPTe and WMMPTe

Parameter	w_1	w_2	w_3	w_4	w_5
CMMPTe	1.2207	0.9	1.184	0.838	1.206
WMMPTe	0.9	0.1	0.89	1	0.95

CMMPTe: constrained MMPTE WMMPTe: weighted MMPTE

▼ Table 2. Optimized distribution of excitations for Rx arrays

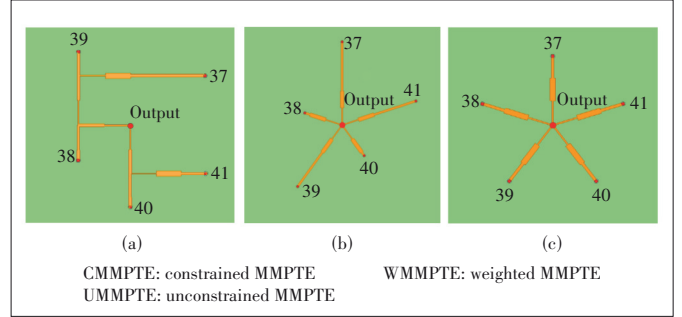
Port Number	37	38	39	40	41
UMMPTe	0.14∠9	0.58∠146	0.38∠1	0.66∠144	0.23∠0
WMMPTe	0.44∠-29	0.44∠-149	0.44∠14	0.44∠-140	0.44∠0
CMMPTe	0.44∠0	0.44∠0	0.44∠0	0.44∠0	0.44∠0

CMMPTe: constrained MMPTE

Rx: receiving

UMMPTe: unconstrained MMPTE

WMMPTe: weighted MMPTE



▲ Figure 4. Feeding networks for Rx arrays: (a) UMMPTe, (b) WMMPTe and (c) CMMPTe

▼ Table 3. Optimized distribution of the excitations for Tx arrays

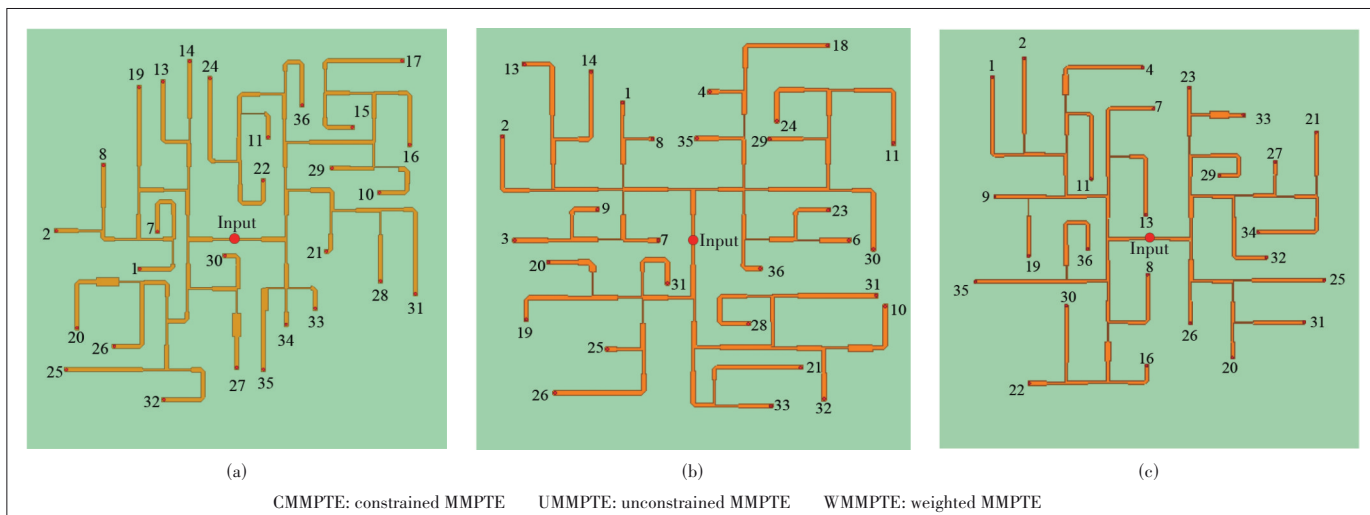
Port Number	UMMPTe	WMMPTe	CMMPTe
1	0.10∠-2	0.22∠-37	0.14∠49
2	0.13∠26	0.19∠4	0.07∠87
3	0.07∠81	0.11∠78	0.05∠-107
4	0.04∠-127	0.10∠-137	0.11∠-31
5	0.06∠19	0.04∠5	0.01∠-103
6	0.07∠128	0.09∠147	0.05∠-87
7	0.16∠-66	0.24∠-23	0.33∠120
8	0.15∠-60	0.19∠-7	0.29∠145
9	0.04∠36	0.12∠102	0.19∠-142
10	0.08∠168	0.09∠-176	0.02∠-17
11	0.08∠-83	0.08∠-15	0.13∠131
12	0.07∠10	0.07∠41	0.01∠-170
13	0.29∠-168	0.15∠-167	0.16∠114
14	0.19∠-162	0.14∠-166	0.04∠164
15	0.10∠-16	0.04∠-1	0.07∠-68
16	0.13∠62	0.07∠26	0.16∠24
17	0.09∠163	0.07∠148	0.06∠-4
18	0.07∠-130	0.10∠-118	0.09∠-29
19	0.26∠157	0.28∠172	0.13∠101
20	0.08∠-142	0.14∠-159	0.15∠-68
21	0.23∠-61	0.22∠-60	0.11∠-138
22	0.11∠-30	0.07∠-16	0.07∠-79
23	0.05∠41	0.13∠125	0.19∠-138
24	0.11∠89	0.12∠106	0.04∠-138
25	0.18∠-34	0.19∠2	0.25∠118
26	0.20∠-46	0.19∠11	0.38∠154
27	0.11∠-144	0.07∠-154	0.14∠-165
28	0.21∠-161	0.15∠-169	0.05∠152
29	0.15∠-55	0.13∠10	0.26∠146
30	0.16∠21	0.21∠23	0.09∠87
31	0.32∠-10	0.30∠13	0.10∠38
32	0.19∠-40	0.20∠16	0.26∠119
33	0.29∠166	0.25∠179	0.09∠103
34	0.31∠-170	0.19∠-162	0.14∠116
35	0.20∠-64	0.24∠-4	0.33∠121
36	0.17∠0	0.24∠0	0.16∠57

CMMPTe: constrained MMPTE

Tx: transmitting

UMMPTe: unconstrained MMPTE

WMMPTe: weighted MMPTE



▲ Figure 5. Feeding networks for Tx arrays: (a) UMMPTE, (b) WMPTE, and (c) CMMPTE

networks have been built by the transmission line theory. The amplitude distribution of the feeding network is controlled by the power dividers while the phase distribution is controlled by the length of the feeding line. Note that one can ignore those patch elements with very small amplitudes of excitations during the design of the feeding networks. For example, the patch elements 3, 4, 5, 6, 9, 12, 18, and 23 in UMMPTE are insignificant and can thus be neglected. Since too many details are involved, the dimensions of the feeding networks are not labeled in Figs. 4 and 5.

In practice, the design of a WPT system must meet the PTE requirement for a given transmission distance. The PTE depends on a number of factors, including the antenna elements, element spacing, transmission distance, aperture size, substrate material, environment, and array configurations. The design procedure of the WPT system using antenna arrays can be summarized as follows.

1) Set up the WPT system. According to the PTE requirement and transmission distance, one needs to determine the aperture sizes of both Tx and Rx arrays so that they are in the Fresnel region of each other. The antenna elements, the inter-element spacing, and array configurations can be determined by the application scenarios.

2) Determine the scattering parameters. Once the WPT system is set up, one needs to determine the proper weighting coefficients to achieve the desired radiation pattern. The scattering parameters can be obtained by simulation or by measurement. It is noted that the scattering parameters contain all the information about the WPT system, including mutual couplings, array configuration as well as environments.

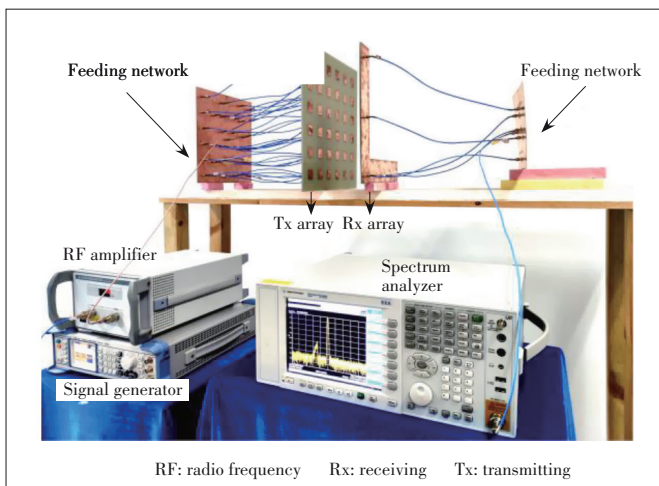
3) Find the optimal distribution of excitations for the array elements. The optimal distributions of excitations for Tx and Rx arrays can be determined from Eqs. (5) - (8). For UMMPTE, one needs to solve an eigenvalue equation; for WMPTE and CMMPTE, the optimal distribution can be ob-

tained analytically.

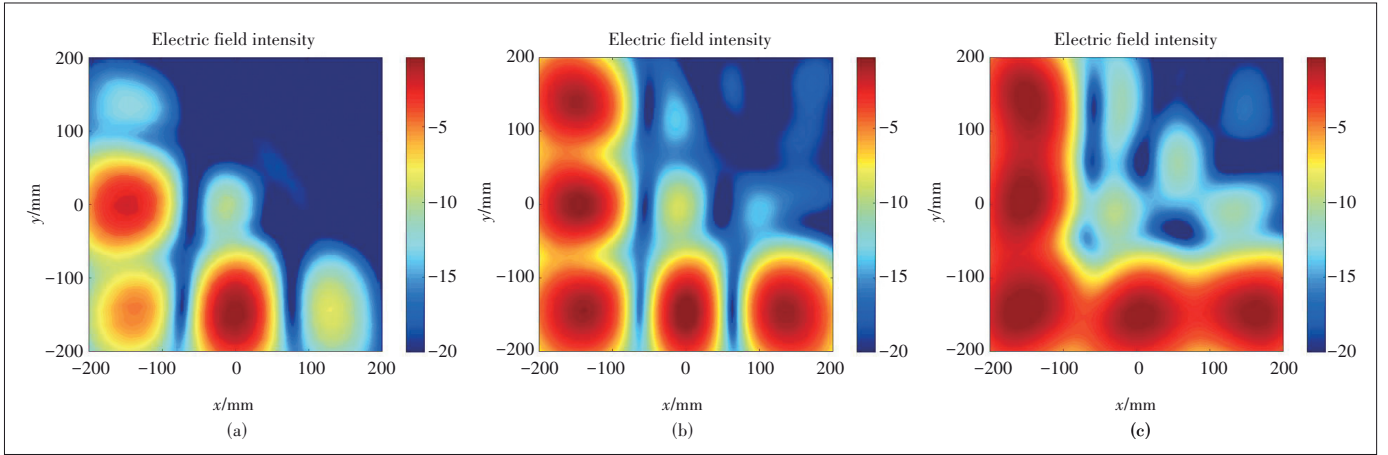
4) Build the feeding networks. The feeding networks for both Tx and Rx arrays can be built from the optimized distribution of excitations using the transmission line theory. The amplitude distribution is achieved by power dividers and the phase distribution is controlled by the lengths of the feeding lines.

5 Results and Discussions

The setup of the WPT system is shown in Fig. 6. Both the Tx and Rx arrays are connected to a dedicated feeding network to realize the optimized distribution of excitations so that the highest PTE can be reached under three different application scenarios. The input power to the Tx array is set to 30 dBm and is provided by a radio frequency (RF) amplifier connected to a signal generator. The normalized field patterns generated by the three Tx arrays are respectively plotted in Figs. 7 (a), 7(b), and 7(c), and the numerical values of



▲ Figure 6. Setup of wireless power transmission (WPT) system



▲ Figure 7. Simulated electric field patterns from (a) unconstrained MMPTE (UMMPTE), (b) weighted MMPTE (WMMPTE), and (c) constrained MMPTE (CMMPTE)

the received power at the spots where the test receiving antenna elements reside are listed in Table 4.

For UMMPTE, the received power is not evenly distributed along with the receiving elements, and the received power level at ports 38 and 40 is significantly higher than the rest, which guarantees that the total power received by the L-shaped Rx array is maximized. For WMMPTE and CMMPTE, the fluctuation of the received power distribution is less than 1 dB along with the receiving elements. Note that the received power obtained from CMMPTE is lower than that obtained from WMMPTE. The reason is that the former requires that the radiated power pattern is flat along with the receiving elements while the latter only requires that the received power levels at the receiving elements are all equal.

The total measured losses of the three sets of feeding networks (Tx combined with Rx) are 3.5 dB, 3.6 dB and 3.5 dB, respectively. The measured transmission coefficients of the two-port system defined by the large dotted square in Fig. 1 are plotted in Fig. 8 and the values of $|S_{21}|$ for the three application scenarios are -10.1 dB, -11.7 dB and -13.1 dB at 2.45 GHz, respectively. The transmission coefficient S_{21} of the two-port network can be used to calculate the power transmission efficiency T of the WPT system including the feeding networks through

$$T = 10^{|S_{21}|/10} \times 100\% . \quad (14)$$

In terms of Eq. (14), the measured PTEs of the system are

▼ Table 4. Received power distributions at spots where the receiving antennas are positioned

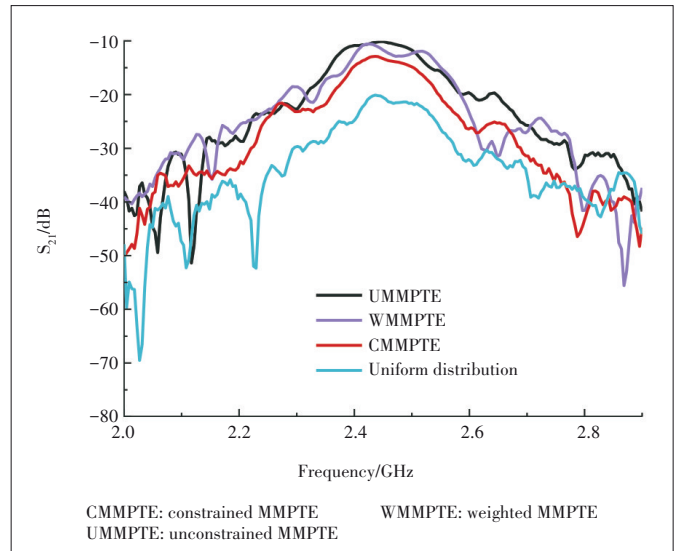
Port Number	37/dBm	38/dBm	39/dBm	40/dBm	41/dBm
UMMPTE	7.2	17.8	14.9	19.6	11.3
WMPTE	14.7	14.9	14.6	14.8	14.4
CMMPTE	13.5	13.4	13.5	13.2	12.8

CMMPTE: constrained MMPTE

WMMPTE: weighted MMPTE

UMMPTE: unconstrained MMPTE

found to be 21.8%, 14.8%, and 10.7% respectively. The simulation and measured PTEs are listed in Table 5, and they are compared with the usual design with uniform distribution of excitations for both Tx and Rx (i.e., without optimization). The PTE of the latter is only 2.2% and is significantly lower than the three optimized results. The highest PTE is given by UMMPTE since it does not involve any constraints. The lowest PTE is given by CMMPTE as it requires that the radiated energy is equally distributed along the whole path of the



▲ Figure 8. Measured $|S_{21}|$ of the wireless power transmission (WPT) system

▼ Table 5. Comparison of PTEs

Methods	Simulated PTE/%	Measured PTE/%
UMMPTE	22.4	21.8
WMMPTE	15.1	14.8
CMMPTE	11.4	10.7
Uniform distribution	2.5	2.2

CMMPTE: constrained MMPTE

UMMPTE: unconstrained MMPTE

PTE: power transmission efficiency

WMMPTE: weighted MMPTE

L-shape, while WMMPTE only requires that the radiated energy is equally distributed at the locations where the Rx elements are placed.

6 Conclusions

Three application scenarios for the WPT system have been investigated by MMPTE, which respectively correspond to the unconstrained MMPTE, the weighted MMPTE, and the constrained MMPTE. The three application scenarios have been implemented by the same WPT system, in which the Tx array consists of 36 microstrip patch elements and is configured as a square while the Rx array consists of 5 patch elements and is configured as an L shape. The WPT system, operating at 2.45 GHz, is designed, simulated and prototyped. The first scenario does not put any constraints on the radiated field patterns; the second scenario requires that the received power levels at all Rx elements are equal; the third scenario requires that radiated field pattern along the Rx array is flat. By maximizing the PTE between the Tx and Rx arrays, the optimized distributions of excitations for both Tx and Rx arrays are obtained analytically or by solving an eigenvalue equation. Based on the optimized distribution of excitations, the feeding networks for both Tx and Rx can be built by using the theory of the transmission line. Simulation and experimental results indicate that the first scenario, where no constraints are involved, yields the highest PTE. The last two scenarios are seldom studied in previous publications.

The three optimization methods proposed for the design of WPT systems apply to any environment and any antenna array. The weighted MMPTE and the constrained MMPTE can be used to achieve various field patterns or power distributions on the Rx side of the WPT systems, and at the same time to maintain the highest possible PTE.

It is noted that the MMPTE can be formulated in terms of other circuit parameters such as the impedance parameters or admittance parameters, and the discussions are the same as for the scattering parameters^[40].

References

- [1] BROWN W C. The history of power transmission by radio waves [J]. *IEEE transactions on microwave theory and techniques*, 1984, 32(9): 1230 – 1242. DOI: 10.1109/TMTT.1984.1132833
- [2] SHINOHARA N. *Wireless power transfer via radiowaves* [M]. New York, USA: John Wiley & Sons, 2014
- [3] OKRESS E C, BROWN W, MORENO T. Microwave power engineering [J]. *IEEE Spectrum*, 1964, 1(10): 76 – 76. doi: 10.1109/MSPEC.1964.6501190
- [4] SHINOHARA N. Development of high efficient phased array for microwave power transmission of Space Solar Power Satellite/Station [C]//*Proceedings of 2010 IEEE Antennas and Propagation Society International Symposium*. IEEE, 2010: 1 – 4. DOI: 10.1109/APS.2010.5562088
- [5] MASSA A, OLIVERI G, VIANI F, et al. Array designs for long-distance wireless power transmission: state-of-the-art and innovative solutions [J]. *Proceedings of the IEEE*, 2013, 101(6): 1464 – 1481. DOI: 10.1109/JPROC.2013.2245491
- [6] NGUYEN P T, ABBOSH A M, CROZIER S. 3-D focused microwave hyperthermia for breast cancer treatment with experimental validation [J]. *IEEE transactions on antennas and propagation*, 2017, 65(7): 3489 – 3500. DOI: 10.1109/TAP.2017.2700164
- [7] CHOW E Y, YANG C L, OUYANG Y H, et al. Wireless powering and the study of RF propagation through ocular tissue for development of implantable sensors [J]. *IEEE transactions on antennas and propagation*, 2011, 59(6): 2379 – 2387. DOI: 10.1109/TAP.2011.2144551
- [8] LI S Q, MI C C. Wireless power transfer for electric vehicle applications [J]. *IEEE journal of emerging and selected topics in power electronics*, 2015, 3(1): 4 – 17. DOI: 10.1109/jestpe.2014.2319453
- [9] LI X, DUAN B Y, SONG L W. Design of clustered planar arrays for microwave wireless power transmission [J]. *IEEE transactions on antennas and propagation*, 2019, 67(1): 606 – 611. DOI: 10.1109/TAP.2018.2876192
- [10] LI X, LUK K M, DUAN B Y. Multiobjective optimal antenna synthesis for microwave wireless power transmission [J]. *IEEE transactions on antennas and propagation*, 2019, 67(4): 2739 – 2744. DOI: 10.1109/TAP.2019.2893312
- [11] GOWDA V R, YURDUSEVEN O, LIPWORTH G, et al. Wireless power transfer in the radiative near field [J]. *IEEE antennas and wireless propagation letters*, 2016, 15: 1865 – 1868. DOI: 10.1109/LAWP.2016.2542138
- [12] YI X J, CHEN X, ZHOU L, et al. A microwave power transmission experiment based on the near-field focused transmitter [J]. *IEEE antennas and wireless propagation letters*, 2019, 18(6): 1105 – 1108. DOI: 10.1109/lawp.2019.2910200
- [13] MOSK A P, LAGENDIJK A, LEROSEY G, et al. Controlling waves in space and time for imaging and focusing in complex media [J]. *Nature photonics*, 2012, 6(5): 283 – 292. DOI: 10.1038/nphoton.2012.88
- [14] PENDRY J B, SCHURIG D, SMITH D R. Controlling electromagnetic fields [J]. *Science*, 2006, 312(5781): 1780 – 1782. DOI: 10.1126/science.1125907
- [15] CHENG Y J, XUE F. Ka-band near-field-focused array antenna with variable focal point [J]. *IEEE transactions on antennas and propagation*, 2016, 64(5): 1725 – 1732. DOI: 10.1109/tap.2016.2540646
- [16] ZHAO D S, ZHU M. Generating microwave spatial fields with arbitrary patterns [J]. *IEEE antennas and wireless propagation letters*, 2016, 15: 1739 – 1742. DOI: 10.1109/LAWP.2016.2530825
- [17] HUANG Z X, CHENG Y J. Near-field pattern synthesis for sparse focusing antenna arrays based on Bayesian compressive sensing and convex optimization [J]. *IEEE transactions on antennas and propagation*, 2018, 66(10): 5249 – 5257. DOI: 10.1109/TAP.2018.2860044
- [18] CHOU H T, HUNG K L, CHOU H H. Design of periodic antenna arrays with the excitation phases synthesized for optimum near-field patterns via steepest descent method [J]. *IEEE transactions on antennas and propagation*, 2011, 59(11): 4342 – 4345. DOI: 10.1109/TAP.2011.2164221
- [19] WEN G Y. *Foundations of Applied Electrodynamics* [M]. Chichester, UK: John Wiley & Sons, 2010. DOI: 10.1002/9780470661369
- [20] WEN G Y. *Foundations for radio frequency engineering* [M]. Singapore: World Scientific, 2013. DOI: 10.1142/9040
- [21] WEN G Y. The method of maximum power transmission efficiency for the design of antenna arrays [J]. *IEEE open journal of antennas and propagation*, 2021, 2: 412 – 430. DOI: 10.1109/OJAP.2021.3066310
- [22] WANG X Y, YANG G M, WEN G Y. A new design of focused antenna arrays [J]. *Microwave and optical technology letters*, 2014, 56(10): 2464 – 2468. DOI: 10.1002/mop.28616
- [23] LONG S, WEN G Y. Optimal design of focused antenna arrays [J]. *IEEE transactions on antennas and propagation*, 2014, 62(11): 5565 – 5571. DOI: 10.1109/tap.2014.2357421
- [24] JIANG Y H, WEN G Y, YANG L S, et al. Circularly-polarized focused microstrip antenna arrays [J]. *IEEE antennas and wireless propagation letters*, 2015, 15: 52 – 55. DOI: 10.1109/LAWP.2015.2428931
- [25] HE X P, WEN G Y, WANG S Y. Optimal design of focused arrays for microwave-induced hyperthermia [J]. *IET microwaves, antennas & propagation*, 2015, 9(14): 1605 – 1611. DOI: 10.1049/iet-map.2014.0696
- [26] HE X P, WEN G Y, WANG S Y. A hexagonal focused array for microwave hy-

- perthermia: Optimal design and experiment [J]. *IEEE antennas and wireless propagation letters*, 2016, 15: 56 – 59. DOI: 10.1109/LAWP.2015.2429596
- [27] TONG H P, WEN G Y. Optimal design of smart antenna systems for handheld devices [J]. *IET microwaves, antennas & propagation*, 2016, 10(6): 617 – 623. DOI: 10.1049/iet-map.2015.0339
- [28] WAN W, WEN G Y, GAO S. Optimum design of low-cost dual-mode beam-steerable arrays for customer-premises equipment applications [J]. *IEEE access*, 2018, 6: 16092 – 16098. DOI: 10.1109/ACCESS.2018.2813299
- [29] MIAO X B, WAN W, DUAN Z, et al. Design of dual-mode arc-shaped dipole arrays for indoor base-station applications [J]. *IEEE antennas and wireless propagation letters*, 2019, 18(4): 752 – 756. DOI: 10.1109/LAWP.2019.2901967
- [30] TING L, WEN G Y. Design of MIMO beamforming antenna array for mobile handsets [J]. *Progress in electromagnetics research C*, 2019, 94: 13 – 28. DOI: 10.2528/PIERC19030807
- [31] GUO H D, WEN G Y. Design of bidirectional antenna array with adjustable endfire gains [J]. *IEEE antennas and wireless propagation letters*, 2019, 18(8): 1656 – 1660. DOI: 10.1109/LAWP.2019.2926525
- [32] YANG X D, WEN G Y, SUN H C. Optimum design of wireless power transmission system using microstrip patch antenna arrays [J]. *IEEE antennas and wireless propagation letters*, 2017, 16: 1824 – 1827. DOI: 10.1109/LAWP.2017.2682262
- [33] SUN H C, WEN G Y. Optimum design of wireless power transmission systems in unknown electromagnetic environments [J]. *IEEE access*, 2017, 5: 20198 – 20206. DOI: 10.1109/ACCESS.2017.2757002
- [34] GU X Z, WEN G Y. Design of a near-field RFID antenna array in metal cabinet environment [J]. *IEEE antennas and wireless propagation letters*, 2019, 18(1): 79 – 83. DOI: 10.1109/LAWP.2018.2880965
- [35] XIAO C, WEN G Y. An optimization method for the synthesis of flat-top radiation patterns in the near- and far-field regions [J]. *IEEE transactions on antennas and propagation*, 2019, 67(2): 980 – 987. DOI: 10.1109/TAP.2018.2882653
- [36] WEN G Y. Theoretical study for microwave power transmission [J]. *Journal of electronics and information technology*, 1998, 20(4): 538 – 545
- [37] KAY A. Near-field gain of aperture antennas [J]. *IRE transactions on antennas and propagation*, 1960, 8(6): 586 – 593. DOI: 10.1109/tap.1960.1144905
- [38] BORGIOTTI G. Maximum power transfer between two planar apertures in the Fresnel zone [J]. *IEEE transactions on antennas and propagation*, 1966, 14(2): 158 – 163. DOI: 10.1109/TAP.1966.1138660
- [39] SHERMAN J W. Properties of focused aperture in the Fresnel region [J]. *IRE transactions on antennas and propagation*, 1962, 10(4): 399 – 408. DOI: 10.1109/TAP.1962.1137900
- [40] YUAN Q W, AOKI T. Practical applications of universal approach for calculating maximum transfer efficiency of MIMO-WPT system [J]. *Wireless power transfer*, 2020, 7(1): 86 – 94. DOI: 10.1017/wpt.2020.7

Biographies

SUN Shuyi received the BS degree in information and communication engineering from Nanjing University of Information Science and Technology, China in 2020. Her research interest mainly focuses on antenna design.

WEN Geyi (wgy@nuist.edu.cn) is a National Distinguished Professor with the Nanjing University of Information Science and Technology, China and the Director of the Research Center of Applied Electromagnetics. He is the author of the *Foundations for Radio Frequency Engineering*, the *Foundations of Applied Electrodynamics* (Wiley, 2010), the *Advanced Electromagnetic Field Theory* (in Chinese, National Defense Publishing House, 1999), and the *Modern Methods for Electromagnetic Computations* (in Chinese, Henan Science and Technology Press, 1994). He is an IEEE Fellow.

Dynamic Power Transmission Using Common RF Feeder with Dual Supply



DUONG Quang-Thang¹, VO Quoc-Trinh²,

PHAN Thuy-Phuong¹, OKADA Minoru¹

(1. Nara Institute of Science and Technology, Nara 630-0192, Japan;
2. FPT University Da Nang, Da Nang 50500, Vietnam)

DOI: 10.12142/ZTECOM.202202005

<https://kns.cnki.net/kcms/detail/34.1294.TN.20220509.1032.004.html>,
published online May 10, 2022

Manuscript received: 2022-04-18

Abstract: This paper proposes the design concept of a dynamic charging system for electric vehicles using multiple transmitter coils connected to a common radio frequency (RF) feeder driven by a pair of two power supplies. Using a common RF feeder for multiple transmitter coils reduces the power electronic redundancy compared to a conventional system, where each transmitter coil is individually driven by one switched-mode power supply. Currently, wireless charging of electric vehicles is recommended to operate in the frequency range of 85 kHz and beyond. In this frequency range, the signal wavelength is shorter than about 3.5 km. Therefore, a charging pad longer than several hundred meters is subject to the standing wave effect. In such a case, the voltage significantly varies along the RF feeder, resulting in a variation in the received power level when the receiver moves. Specifically, the received power significantly deteriorates when the receiver is nearby a node of the voltage standing wave. In this paper, we employ a pair of two power sources which are electrically separated by an odd-integer number of the quarter wavelength to drive the RF feeder. As a result, the voltage standing wave generated by one power source is complemented by that of the other, leading to stable received power and transmission efficiency at all the receiver's positions along with the charging pad. Simulation results at the 85 kHz frequency band verify the output power stabilization effect of the proposed design. It is worth noting that the proposed concept can also be applied to simultaneous wireless information and power transfer (SWIPT) for passive radio frequency identification (RFID) tags by raising the operation frequency to higher industrial, scientific and medical (ISM) bands, e.g., 13.56 MHz and employing similar modulation methods as in the current RFID technology.

Keywords: dynamic charging; common RF feeder; standing wave; dual power supply

Citation (IEEE Format): Q.-T. Duong, Q.-T. Vo, T.-P. Phan, et al., "Dynamic power transmission using common RF feeder with dual supply," *ZTE Communications*, vol. 20, no. 2, pp. 28 - 36, Jun. 2022. doi: 10.12142/ZTECOM.202202005.

1 Introduction

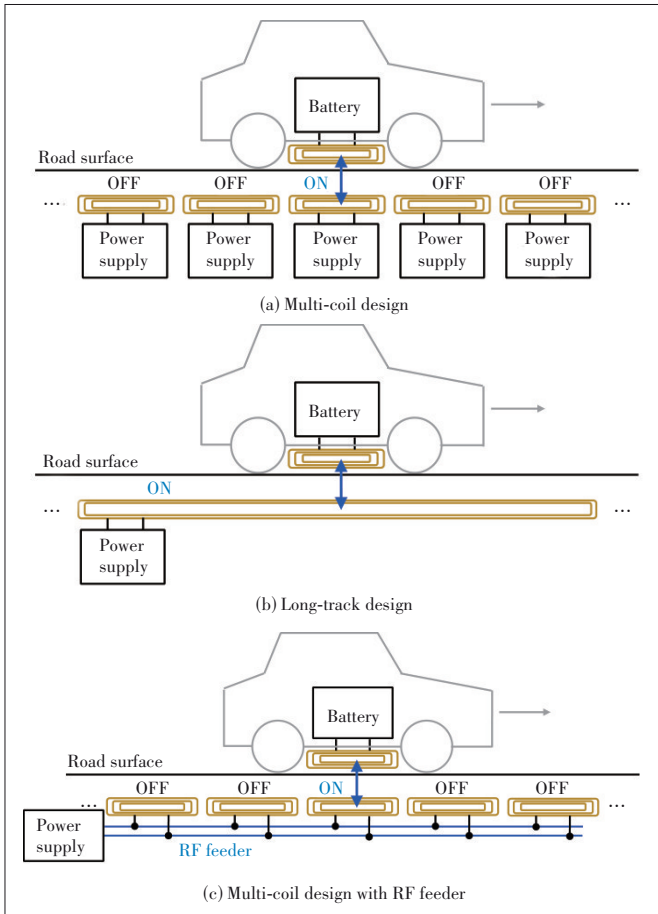
Dynamic charging for moving electric vehicles (EVs) is considered a complement to the capacity limitation of battery technology^[1-5] in increasing the driving range, reducing the battery size and the manufacturing cost. Currently, dynamic charging is being developed based on magnetic induction^[6], where an AC-driven transmitter coil buried under the road wirelessly induces an electric current in the receiver coil usually placed under the chassis of EVs. The wireless energy transmission principle is simple. However, designing an effective and practical dynamic charging system is very challenging because of the large scale of infrastructure, the high charging power level, the strict requirements on safety for human bodies and devices nearby, and the requirements on cost and efficiency.

Several dynamic charging systems have been proposed so

far. Considering the ground infrastructure, the current dynamic charging techniques can be classified into two basic designs: the multi-coil design^[7-8] and long-track design^[9-10]. As illustrated in Fig. 1(a), in the multiple-coil design, many transmitter coils are installed under and along the road to provide a wide charging range for the EV while it is on the move. Meanwhile, in the long-track design in Fig. 1(b), the wide charging range is provided by only one elongated transmitter coil. In terms of structure, the multiple-coil design is more complex compared to the long-track design. However, by sensing the EV position, the multiple-coil design can turn on only the transmitter coil right under the EV to focus the magnetic energy, prevent a leaked electromagnetic (EM) field to surrounding space, and achieve high power transfer efficiency. On the contrary, the long-track design suffers from low efficiency and a large leaked EM field because it generates the EM field across the whole charging range. For that reason, the multiple-coil design is a preferable option if its structure is simplified by some means.

The complexity of the multiple-coil design in Fig. 1(a)

This work was supported in part by JSPS KAKENHI under Grant Nos. 20K14736 and 19K04376.



▲ Figure 1. Dynamic charging systems for electric vehicles (EVs)

comes from the fact that many coils need to be installed and, more importantly, the huge power electronic burden required to drive the coils. Conventionally, each transmitter coil is equipped with a switched-mode power supply to convert 50 Hz/60 Hz AC into a radio frequency (RF) signal for efficient wireless energy transmission. For instance, in order to carry out dynamic charging on a 100 m road by using transmitter coils with the size of 1 m×1 m, one hundred power supplies of output from several kW to several tens of kW are required. The number of power sources increases when further extending the charging range. In fact, the conventional driving mechanism is redundant because at any time instant there is only one power source in operation while the others are in the waiting state. To reduce such a power electronic redundancy, an RF feeder line should be used to carry signals from one central power source to the coils as illustrated in Fig. 1(c). In such a system, by controlling the switches that connect the feeder to the coils, the automatic coil activation/deactivation effect in the conventional multiple-coil design can be realized. Also, the multiple-coil design with a common RF feeder is flexible in satisfying the required power level in practical applications. Power supply with high output may be used when the system is deployed in roads with many EVs. Lower

output sources may be used in not-crowded road deployment.

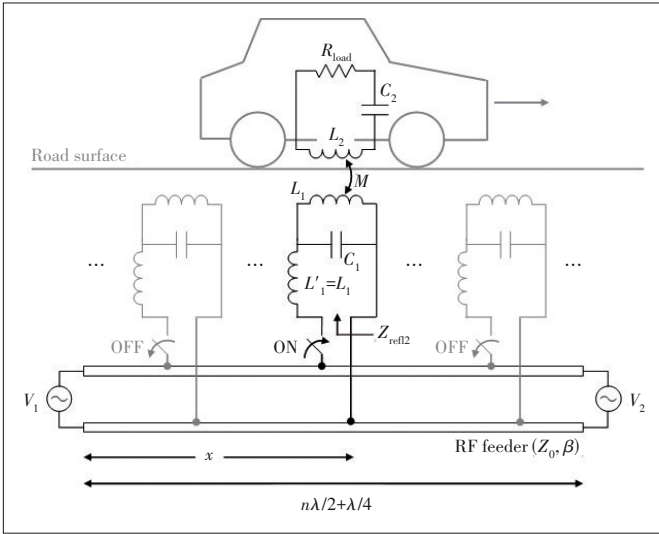
The multiple-coil structure with a common RF feeder is a promising design for dynamic charging. However, this design suffers from a standing wave problem when extending the charging range. Currently, the 85 kHz frequency range is recommended for wireless charging of EVs. In this frequency range, the signal wavelength is about 3.5 km. Therefore, if the RF feeder length is about several hundreds of meters or more, the signal strength variation along the feeder becomes significant. In the extreme, if the feeder length is longer than a quarter wavelength of about 882 m, there will be nodes and anti-nodes in the voltage standing wave^[11] pattern along the feeder. In such a case, the EV receives high power if it nears an anti-node but receives very low power if it nears a node. In order to deal with this problem, we propose a multiple-coil charging system using a common RF feeder driven by a pair of two power supplies located at its two ends. In our design, the two power sources are electrically separated by an odd-integer number of the quarter wavelength. Thus, voltage standing waves generated by the two power supplies will compensate for each other in stabilizing the received power for the EV.

It is worth noting that the proposed concept can be applied to short-range wide-coverage simultaneous wireless information and power transfer (SWIPT) for passive radio frequency identification (RFID) tags. This application can be realized by raising the operating frequency to an industrial, scientific and medical (ISM) band in the MHz range, e. g., 6.78 MHz or 13.56 MHz, and reducing the dimensions of each coil to several centimeters. The power transmission has the same principle as that in the dynamic charging mechanism mentioned above; the information transmission methods are similar to those in current RFID technology. For instance, communications from the power transmitter (transponder) to the power receiver (tag) can use amplitude modulation, and communications in the reverse direction can employ load modulation.

In this paper, for simplicity, we focus on the dynamic charging application for EVs using the operating frequency of 85 kHz. Following theoretical analysis, system-level simulations using LTspice will be provided to confirm the receive power stabilization effects of the proposed concept.

2 Design Concept of Proposed Dynamic Charging System

We consider a dynamic charging system for EVs as described in Fig. 2. For simplicity, let us assume that the charging pad is serving one receiver (EV) at a time. Similar to many conventional dynamic charging systems, the proposed system consists of many transmitter coils buried under the road to deliver power to the receiver moving from the left to the right in the figure. The difference in our design is that all the transmitter coils and their associated compensation circuits are connected to a common RF feeder. In doing so, our system significantly reduces power electronic redundancy compared to the



▲ Figure 2. Proposed dynamic charging system

conventional system using one power supply for one transmitter coil. The RF feeder is a transmission line of any configuration, but preferably the one with low loss and ease of installment. In this paper, to avoid detailed discussion on the feeder, let us assume that the feeder is a lossless transmission line having real-valued characteristic impedance Z_0 .

The common RF is driven by a pair of two power sources which are designed to operate within a certain frequency band f , with the angular frequency $\omega = 2\pi f$. Here, it is worth noting that our system does not require perfect frequency and time synchronizations between the two power supplies. The two source frequencies may be respectively slightly shifted from each other. The frequency shifts should be random so that the two sources do not interfere with each other, but these shifts should be small enough so that the system can be considered to resonate at f . These requirements are easily satisfied because the actual frequencies of power supplies are always different from their designed value. There are no need for frequency and phase control between the sources.

Given the operation frequency range f , the electrical length of the RF feeder should be an odd-integer number of the quarter wavelength

$$L_e = \lambda/4 + n\lambda/2 = (2n + 1)\lambda/4, \quad (1)$$

where $\lambda = cf$ is the wavelength and n is an integer. This does not mean that the proposed system is effective only when the length of the charging pad takes one of these special values. If the charging pad has the length L_p that is different from L_e , a circuit equivalent to a transmission line portion having characteristic impedance Z_0 and length $(L_e - L_p)$ can be inserted into the feeder for compensation. Here, for the sake of simplicity let us assume that the actual length of the charging pad is also equal to L_e given by Eq. (1). Under this condition, the following effects are expected:

- The RF feeder is seen as a quarter wavelength resonator at the frequency f , which enables efficient power transmission from the sources to the transmitter coils.

- The voltage standing wave patterns generated by the two sources compensate for each other. At positions where the voltage generated by the first source is small, the voltage generated by the second is large, and vice versa. This effect guarantees a stable received power for the EV when it moves along the charging pad.

- The condition of the feeder length also separates the two sources from each other. The internal resistance of one source is seen as a very large impedance by the other. This effect prevents energy transfer between the sources.

Without loss of generality, let us assume that all the transmitter coils have identical inductances denoted by L_1 as shown in Fig. 2. The inductance of the receiver coil is denoted by L_2 and the mutual inductance between the receiver and each of the transmitter coils is M . The strength of coupling between L_1 and L_2 is represented by a coupling coefficient $k = M/\sqrt{L_1 L_2}$ which takes value from 0 to 1. The larger the value of k , the stronger the coupling. As for wireless charging of EVs, the coupling coefficient usually takes a value of around 0.1, or at most around 0.2.

The load resistance is denoted by R_{load} . The system is assumed to be equipped with a mechanism that can automatically turn on only the transmitter coil right below the EV and turn off the others to prevent losses and leaked EM fields to the surrounding space. The receiver coil L_2 is resonated in series with a capacitor C_2 while each transmitter coil is compensated by an inductor-capacitor-inductor (LCL) circuit^[12-13]. The LCL circuit helps to create a largely reflected impedance of the load on the RF feeder, therefore the voltage standing wave patterns will not change so much while the EV is moving. As the standing wave patterns compensate each other, the received power is expected to be stable against the EV movement. This effect will be explained in Section 3. Another effect of the LCL circuits is that they keep the currents in the coils small when not coupled with the load. This effect provides the second protection for the transmitter coils in addition to the automatic turn-on/turn-off mechanism. The resonance condition of the compensation circuits is given by

$$\omega = \frac{1}{\sqrt{L_1 C_1}} = \frac{1}{\sqrt{L_2 C_2}}. \quad (2)$$

3 Principle of Output Power Stabilization

In Fig. 2, voltages of the power sources are denoted by V_1 and V_2 , respectively. Distance from the first source to the receiver position is denoted by x . The phase constant of the RF feeder is denoted by β . As mentioned above, the RF feeder is assumed to be a lossless transmission line with a real-valued

characteristic impedance Z_0 . The phase constant therefore can be calculated as $\beta = 2\pi/\lambda$.

When the RF feeder is lossless and the internal resistances of the sources are negligibly small, the power transfer efficiency of the whole system is dominated by the coupling link between the receiver coil and each transmitter coil. Via the mutual coupling M , the load resistance R_{load} and the receiver resistance r_2 reflect an impedance Z_{refl1} onto the transmitter coil L_1 .

$$Z_{\text{refl1}} = \frac{(\omega M)^2}{r_2 + R_{\text{load}}} . \quad (3)$$

Consequently, via the LCL circuit on the transmitter coil, the impedance Z_{refl1} and the transmitter resistance r_1 reflect another impedance Z_{refl2} onto the RF feeder at position x .

$$Z_{\text{refl2}} = \frac{(\omega L_1)^2}{r_1 + Z_{\text{refl1}}} = \frac{(\omega L_1)^2}{r_1 + \frac{(\omega M)^2}{r_2 + R_{\text{load}}}} . \quad (4)$$

Often, wireless charging coils are designed so that their internal resistances are small. Therefore, the reflected impedance Z_{refl2} can be approximated as

$$Z_{\text{refl2}} \approx \left(\frac{L_1}{M}\right)^2 R_{\text{load}} . \quad (5)$$

This means Z_{refl2} is approximately a multiplication of load resistance R_{load} by $(L_1/M)^2$ times. Also, as the inductances L_1 and L_2 take similar values, the ratio L_1/M is approximately equal to $1/k$, which may take values around 10. As a result, the reflected impedance Z_{refl2} is a multiplication of R_{load} by about 100 times. If $R_{\text{load}} = 5 \Omega$, $Z_{\text{refl2}} \approx 500 \Omega$; if $R_{\text{load}} = 10 \Omega$, $Z_{\text{refl2}} \approx 1000 \Omega$, and so on. Thus, due to the effect of the LCL circuit, the reflected impedance Z_{refl2} usually takes quite a large value. This effect is needed to conserve the voltage standing waves, which are designed to compensate each other to stabilize the output power for the load.

When ignoring losses in the RF feeder and the internal resistances of the power sources, losses arise mainly in the transmission from each transmitter coil to the receiver coil. Power transfer efficiency from the transmitter coil L_1 to the load R_{load} via the mutual inductance M is given by

$$\eta = \frac{(\omega M)^2 R_{\text{load}}}{r_1 (r_2 + R_{\text{load}})^2 + (r_2 + R_{\text{load}})(\omega M)^2} . \quad (6)$$

As shown in Eq. (6), the power transfer efficiency from the transmitter coil to the receiver coil depends on the load resistance. The efficiency takes its maximum value when the load resistance is given by

$$R_{\text{load}}^{\text{opt}} = r_2 \sqrt{1 + \frac{(\omega M)^2}{r_1 r_2}} . \quad (7)$$

The maximum value of η associated with the load resistance $R_{\text{load}}^{\text{opt}}$ is

$$\eta_{\text{max}} = 1 - \frac{2}{1 + \sqrt{1 + \frac{(\omega M)^2}{r_1 r_2}}} . \quad (8)$$

The proposed system can be simplified as shown in Fig. 3, where the coupling link between the transmitter coil and the receiver coils is represented by the reflected impedance Z_{refl2} placed on the RF feeder at position x . The output power P_{out} at the load can be expressed as

$$P_{\text{out}} = \eta(P_{\text{in1}} + P_{\text{in2}}) , \quad (9)$$

where P_{in1} and P_{in2} are respectively the input power by the first and the second sources.

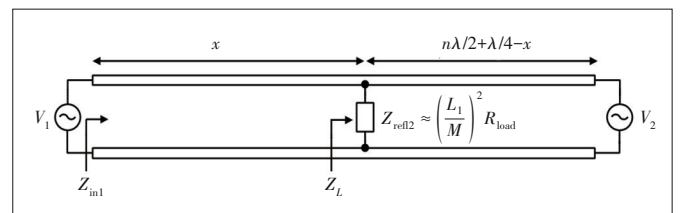
Now, let us consider the input power by the sources. Because the two power sources operate at slightly different frequencies around ω , their signals do not interfere with each other. Therefore, we can separately consider the power transmissions from each source to the load via the common RF feeder. In doing so, the common RF feeder can be considered in two parts: the first part is x [m] long from the first source to the receiver position, and the second part is $[(2k+1)\lambda/4 - x]$ [m] long from the receiver position to the second source. Looking from the first source, the second part is approximately terminated in a short circuit. Based on the transmission line theory^[11], the input impedance of the second part can be expressed as

$$Z_2 = jZ_0 \tan\beta [(2n+1)\lambda/4 - x] . \quad (10)$$

This impedance is connected in parallel with the reflected impedance Z_{refl2} of the load, resulting in a composite impedance Z_L expressed by

$$Z_L = \frac{Z_2 Z_{\text{refl2}}}{Z_2 + Z_{\text{refl2}}} = \frac{jZ_0 \tan\beta [(2n+1)\lambda/4 - x] Z_{\text{refl2}}}{jZ_0 \tan\beta [(2n+1)\lambda/4 - x] + Z_{\text{refl2}}} . \quad (11)$$

This impedance becomes the terminating impedance for the first part of the feeder. As a result, the input of the whole



▲ Figure 3. Simplified circuit of proposed system

feeder seen from the first power source is

$$Z_{in1} = Z_0 \frac{Z_L + jZ_0 \tan \beta x}{Z_0 + jZ_L \tan \beta x} \quad (12)$$

Substituting Z_L in Eq. (11) into Eq. (12) and exploiting the relation $\tan \beta \left[\frac{(2k+1)\lambda}{4} - x \right] = \frac{1}{\tan \beta x}$, we simplify Z_{in1} as follows.

$$Z_{in1} = Z_0 \frac{jZ_0 \tan \beta [(2n+1)\lambda/4 - x] Z_{refl2} + jZ_0 \tan \beta x}{jZ_0 \tan \beta [(2n+1)\lambda/4 - x] + Z_{refl2}} = \frac{j[\tan \beta [(2n+1)\lambda/4 - x] + \tan \beta x] Z_0 Z_{refl2} - Z_0^2 \tan \beta x \tan \beta [(2n+1)\lambda/4 - x]}{jZ_0 \tan \beta [(2n+1)\lambda/4 - x] + Z_{refl2} [1 - \tan \beta [(2n+1)\lambda/4 - x] \tan \beta x]} = \frac{Z_{refl2}}{\cos^2 \beta x} + jZ_0 \tan \beta x \quad (13)$$

The power factor of the input impedance Z_{in1} is

$$\cos \theta_{in1} = \frac{1}{\sqrt{1 + \frac{Z_0}{4Z_{refl2}} \sin^2 2\beta x}} \quad (14)$$

The input power by the first source can then be expressed as

$$P_{in1} = \frac{V_1^2}{2Re\{Z_{in1}\}} \cos^2 \theta_{in1} = \frac{V_1^2 \cos^2 \beta x}{2Z_{refl2}} \cdot \frac{1}{1 + \frac{Z_0}{4Z_{refl2}} \sin^2 2\beta x} \quad (15)$$

Formulation of power transmission from the second source can be carried out in a similar manner to that for the first power source. Looking from the second source, the first part of the RF feeder is approximately terminated in a short circuit. The first part and the reflected impedance are connected in parallel and form a composite impedance that terminates the second part of the feeder. In the transmission from the second source, the two parts of the RF feeder reverse their positions as in the transmission from the first. Therefore, the input impedance of the loaded feeder seen from the second source Z_{in2} can be straightforwardly obtained from Eq. (13) by replacing the length of the first part, x , with that of the second, $(2n+1)\lambda/4 - x$, and vice versa.

$$Z_{in2} = \frac{Z_{refl2}}{\sin^2 \beta x} + jZ_0 \cot \beta x \quad (16)$$

The power factor of the input impedance Z_{in2} is

$$\cos \theta_{in2} = \frac{1}{\sqrt{1 + \frac{Z_0}{4Z_{refl2}} \sin^2 2\beta x}} = \cos \theta_{in1} \quad (17)$$

which is identical to that of the input impedance Z_{in1} . The input power by the second source can then be expressed as

$$P_{in2} = \frac{V_2^2}{2Re\{Z_{in2}\}} \cos^2 \theta_{in2} = \frac{V_2^2 \sin^2 \beta x}{2Z_{refl2}} \cdot \frac{1}{1 + \frac{Z_0}{4Z_{refl2}} \sin^2 2\beta x} \quad (18)$$

Eventually, the received power at the load can be expressed as

$$P_{out} = \eta (P_{in1} + P_{in2}) = \frac{V_1^2 \cos^2 \beta x + V_2^2 \sin^2 \beta x}{2Z_{refl2}} \cos \theta_{in1} \quad (19)$$

In the proposed system, the reflected impedance Z_{refl2} is sufficiently large. In such a case, the power factors are approximately $\cos \theta_{in1} = \cos \theta_{in2} \approx 1$. As a result, the input power P_{in1} and P_{in2} can be approximated as

$$P_{in1} \approx \frac{V_1^2 \cos^2 \beta x}{2Z_{refl2}} \quad (20)$$

$$P_{in2} \approx \frac{V_2^2 \sin^2 \beta x}{2Z_{refl2}} \quad (21)$$

Eqs. (20) and (21) show that when the receiver moves along the road, the input power P_{in1} and P_{in2} exhibit two standing wave patterns shifted by a quarter wavelength. When the receiver is near the position $x = n\lambda/2$, it draws more power from the first source and less power from the second. Reversely, when the receiver is near the position $x = \lambda/4 + n\lambda/2$, it draws more power from the second source and less power from the first. In this way, the two power sources compensate each other in stabilizing output power for the load. Furthermore, the source voltages should be set identically as $V_1 = V_2 = V_0$, so that the output power can be approximated as

$$P_{out} \approx \eta \frac{V_0^2 \cos^2 \beta x + V_0^2 \sin^2 \beta x}{2Z_{refl2}} = \eta \frac{V_0^2}{2Z_{refl2}} \quad (22)$$

As a result, the total power that the receiver receives will be stabilized for all positions of the receiver along the RF feeder.

4 Computer Simulation Results

This section provides computer simulations to confirm the output power stabilization effect of the proposed system. We use LTspice software to emulate the system configuration described in Fig. 2. In the simulations, the system is designed to operate at the frequency $f = 85$ kHz. The two power sources are

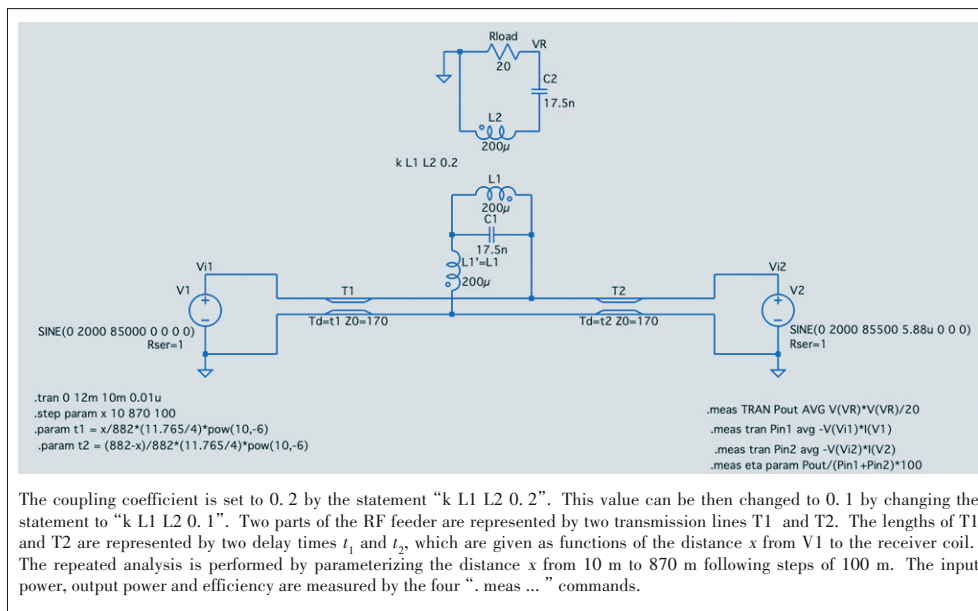
set to operate at the frequencies of 85 kHz and 85.5 kHz, respectively. Here, the frequency shift $\Delta f = 0.5$ kHz is not that important. It can be any value as long as it guarantees that the two power sources operate independently in the resonant frequency band of the system. Also, the phase shift between the two sources is chosen randomly. The source voltages are identically $V_1 = V_2 = 2$ kV, and their internal resistances are set identically to 1Ω .

The RF feeder is assumed to be a two-wire transmission line consisting of two parallel conductors with a diameter of 10 mm. The center-to-center distance between the two conductors of the RF feeder is 21.8 mm, corresponding to the characteristic impedance $Z_0 \approx 120 \cosh^{-1} 21.8/10 = 170 \Omega$. The parameters of the coils, resonant capacitors and the coupling coefficient are listed in Table 1. The simulation circuit configuration is illustrated in Fig. 4. The mutual coupling coefficient between the transmitting coil and receiving coil is set to be 0.1 or 0.2. A lossless transmission line model is used to emulate the RF feeder. The RF feeder length is 882 m (a quarter wave-

▼ **Table 1. Simulation parameters for circuit in Fig. 4**

Symbol	Parameter	Value
L_1	Self-inductance of a transmitter coil	200 μ H
L_2	Self-inductance of a receiver coil	200 μ H
r_1	Internal resistance of a transmitter coil	0.5 Ω
r_2	Internal resistance of a receiver coil	0.5 Ω
Q_1	Q-factor of each transmitter coil	213
Q_2	Q-factor of each receiver coil	213
C_1	Resonant capacitor of LCL circuit	17.5 nF
C_2	Resonant capacitor of a receiver coil	17.5 nF
R_{load}	Load resistance	5 - 30 Ω

LCL: inductor-capacitor-inductor



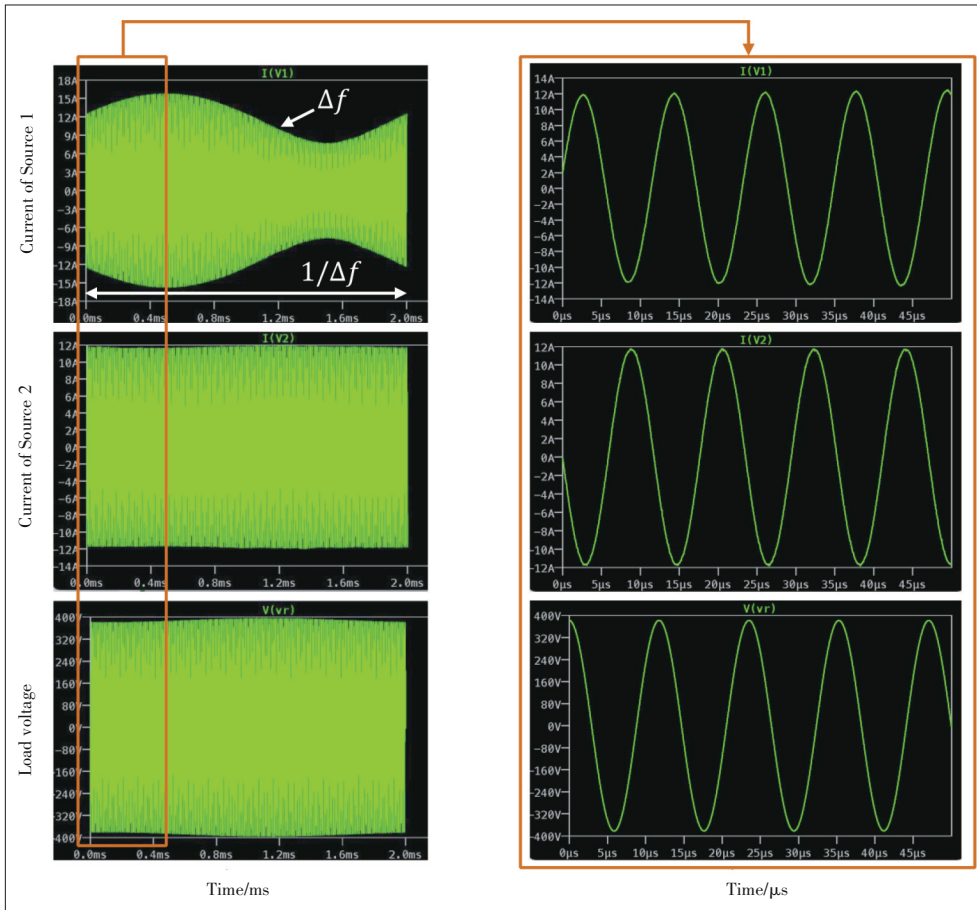
▲ **Figure 4. A snapshot of computer simulations with LTspice**

length) or 2 646 m (three quarter wavelengths). The power supplied by AC sources and received by the receiver is calculated over the steady-state period of 2 ms (from 10 ms to 12 ms) which is as sufficiently long as about 170 times the period of the operating frequency 85 kHz. The duration of 2 ms is also equal to one period $1/\Delta f$ of the frequency shift to make the average power calculations accurate. This can be confirmed by Fig. 5 which shows snapshots of waveforms for $x = 10$ m.

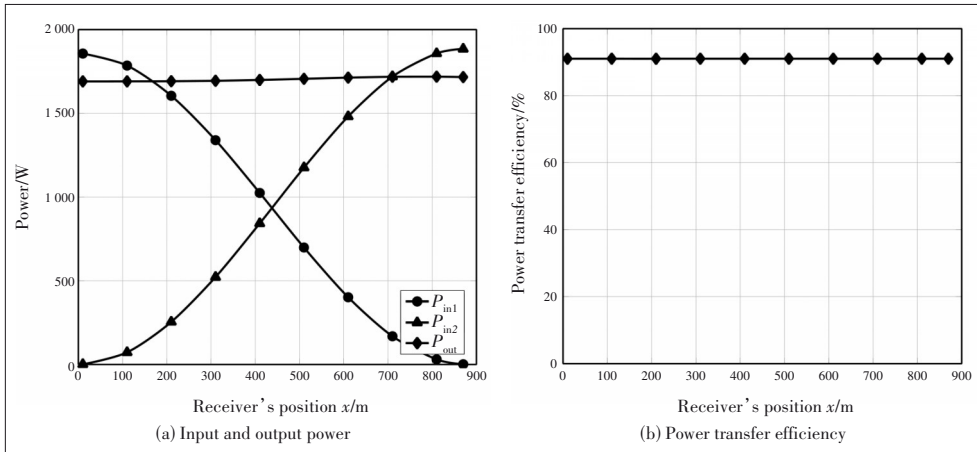
Fig. 6(a) plots the input power from each power source and the out power received at the load when the receiver moves along the RF feeder. Here, the feeder length is a quarter wavelength. The coupling coefficient between each transmitter and the receiver is $k = 0.1$. According to this value of k , the optimal load resistance $R_{load} = 10.7 \Omega$ is chosen to achieve the theoretical maximum efficiency $\eta_{max} = 91\%$ following Eqs. (7) and (8). In this case, the reflected impedance of the load onto the RF feeder is estimated as $Z_{refl2} = 1073 \Omega$ which is sufficiently larger (about 6.3 times) compared to the characteristic impedance 170Ω of the feeder. This setting satisfies the conditions for achieving stable output power, which is mentioned in our theoretical analysis in Section 3. As shown in Fig. 6(a), the input power from the first source P_{in1} gradually decreases from 1.8 kW to nearly 0 kW when the receiver moves from the position $x = 0$ m to the position $x = 882$ m $= \lambda/4$. This variation of P_{in1} with x almost follows the $\cos^2 \beta x$ function shown in Eq. (20). Reversely, the input power from the second source P_{in2} gradually increases from 0 kW to nearly 1.8 kW for the same movement of the receiver, which almost follows the $\sin^2 \beta x$ function shown in Eq. (21). More importantly, the output power P_{out} at the load is stable at around 1.7 kW regardless of the position of the receiver. As a result, as can be seen from Fig. 6(b), the power transfer efficiency is stable at 91%,

which agrees with the calculation following Eq. (8). Fig. 7 confirms similar characteristics of the input power, output power and efficiency for the case where the feeder length is three quarter wavelengths. All of these results agree with our theoretical analysis in Section 3.

Fig. 8 demonstrates the results for the case $k = 0.1$, $R_{load} = 5 \Omega$, and $L_e = \lambda/4$. In this case, the input power still follows the theoretical analysis in Eqs. (20) and (21), the power transfer efficiency is stable but the output power slightly varies when the receiver is moving. This is because the reflected impedance of the load becomes $Z_{refl2} = 500 \Omega$, which is nearly 3 times



▲ Figure 5. Snapshots of waveforms for $x = 10$ m indicating that the analysis is in steady-state



▲ Figure 6. Simulation results for $k = 0.1$, $R_{load} = 10.7 \Omega$ (optimal load), and $L_e = \lambda/4$

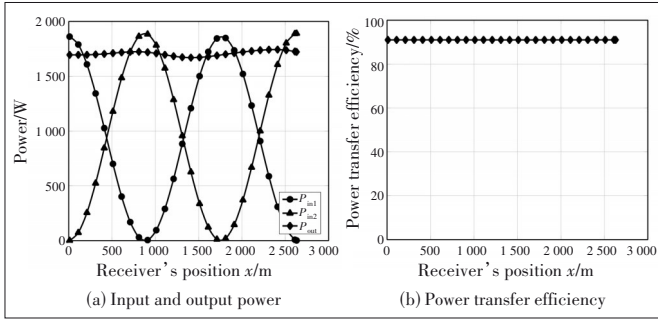
the characteristic impedance of the feeder. As the reflected impedance Z_{refl2} is not sufficiently large, the receiver movement affects the voltage standing wave patterns and deteriorates their mutual compensation. As can be seen from Fig. 8(a), the total power of about 3.7 kW has been input from the sources. This power level is larger than that in Fig. 5. This is because when Z_{refl2} decreases, the input power increases as shown in

Eqs. (20) – (22). Fig. 9 demonstrates the results for the case $k = 0.1$ and $R_{load} = 15 \Omega$. In this case, the power transfer efficiency and the output power are stable; the input power level decreases to about 1.4 kW. This is because Z_{refl2} has increased to 1500Ω , which is nearly 9 times Z_0 .

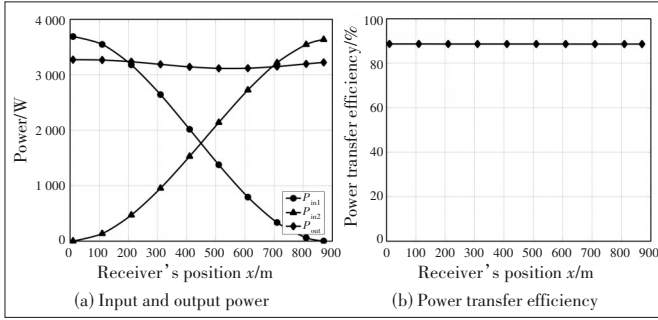
Figs. 10 – 12 demonstrate the simulation results for the case of stronger coupling with $k = 0.2$ and load resistance of 10Ω , 21.3Ω (optimal load) and 30Ω , respectively. Fig. 10(a) exhibits a small fluctuation in the output power because in this case the reflected impedance $Z_{refl2} = (1/0.2)^2 \times 10 = 250 \Omega$, which is not sufficiently larger (only nearly 1.5 times) compared to the characteristic impedance $Z_0 = 170 \Omega$. Meanwhile, Figs. 11(a) and 12(a) show stable output power because in these cases, the reflected impedance becomes 532.5Ω and 750Ω , which are quite larger (3.1 times and 4.4 times, respectively) compared to Z_0 . The power transfer efficiency is observed as 94%, 95.3% and 95%, respectively for each value of the load resistance. The efficiencies increase compared to the results in Figs. 6 – 8 because the coupling coefficient is doubled. The input power level also increases to 7.6 kW, 3.7 kW and 2.7 kW, respectively for each value of the loads. The reason for the increase in input power level is that the reflected impedance has decreased.

5 Conclusions

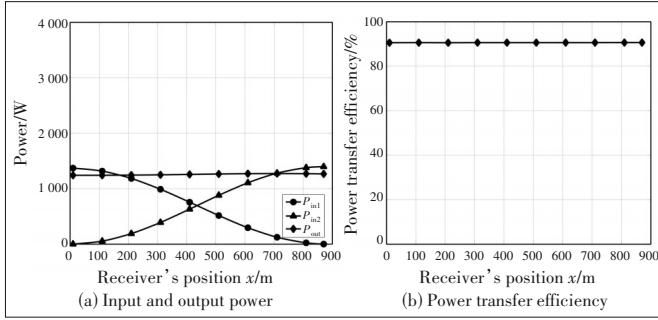
In this paper, we have proposed the design concept of a dynamic charging system for the EV using multiple transmitter coils connected to a common RF feeder driven by a pair of two power supplies. The computer simulations at the 85 kHz band confirm that the voltage standing waves generated by a pair of two sources mutually compensate each other and deliver stable output power regardless of the receiver position along the road. In summary, the



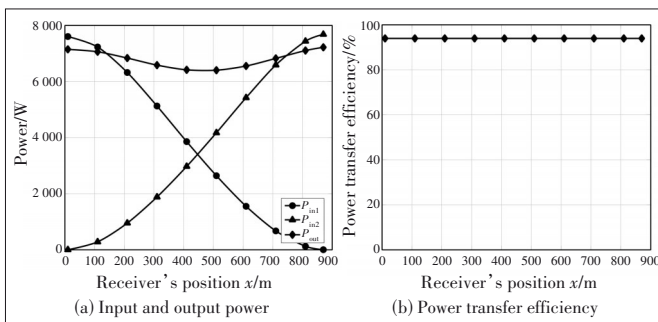
▲ Figure 7. Simulation results for $k = 0.1$, $R_{load} = 10.7 \Omega$ (optimal load), and $L_e = 3\lambda/4$



▲ Figure 8. Simulation results for $k = 0.1$, $R_{load} = 5 \Omega$, and $L_e = \lambda/4$



▲ Figure 9. Simulation results for $k = 0.1$, $R_{load} = 15 \Omega$, and $L_e = \lambda/4$

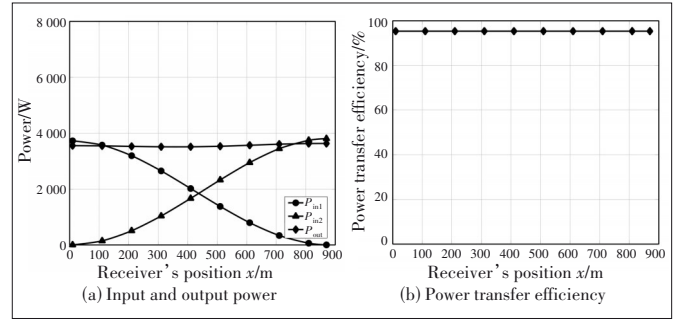


▲ Figure 10. Simulation results for $k = 0.2$, $R_{load} = 10 \Omega$, and $L_e = \lambda/4$

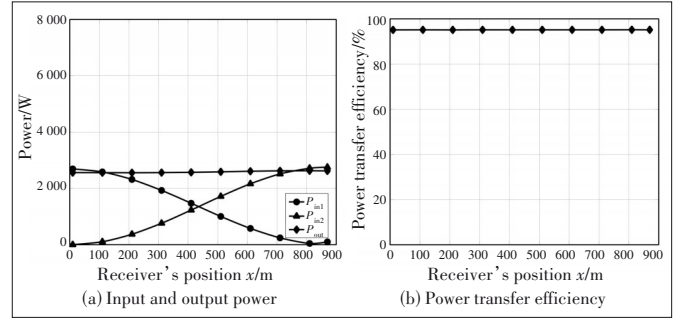
advantages of our proposed system are as follows.

- The proposed charging pad can obtain attractive effects as in any multi-coil charging system, activating only the transmitter coil right under the receiver, focusing the magnetic energy toward the receiver, achieving effective power transmission, and reducing EM leakage to surrounding space.

- Using a common RF feeder for all transmitter coils, our



▲ Figure 11. Simulation results for $k = 0.2$, $R_{load} = 21.3 \Omega$ (optimal load), and $L_e = \lambda/4$



▲ Figure 12. Simulation results for $k = 0.2$, $R_{load} = 30 \Omega$, and $L_e = \lambda/4$

system reduces the power electronic redundancy compared to conventional multiple coil systems, where each transmitter coil is individually driven by one switched-mode power supply.

- Our system can deliver stable output power and achieve stable power transfer efficiency regardless of the receiver position along with the charging pad.

- The proposed system can be easily applied in practice. Although the electrical length of the RF feeder is required to be an odd-integer number of the quarter wavelength, the length of the proposed charging pad can be flexibly chosen according to the practical applications as long as the copper loss is small enough. The difference in the actual length and the required electrical length can be resolved by inserting a compensation circuit into the feeder. Also, the proposed system does not require any time and frequency synchronization between the two sources as long as they operate at slightly different frequencies within the resonant point around the target frequency band. The requirement that the reflected impedance of the load onto the feeder should be large is not so strict and can be satisfied easily. As can be seen from the simulation results in Section 4, a reflected impedance of about 1.4 times the characteristic impedance is enough for a quite stable output power profile.

- The proposed concept can also be applied to SWIPT for passive RFID tags by raising the operating frequency to an ISM MHz band and employing similar modulation methods as in the current RFID technology.

References

- [1] YILMAZ M, KREIN P T. Review of battery charger topologies, charging power levels, and infrastructure for plug-in electric and hybrid vehicles [J]. *IEEE transactions on power electronics*, 2013, 28(5): 2151 – 2169. DOI: 10.1109/TPEL.2012.2212917
- [2] CHOI S Y, GU B W, JEONG S Y, et al. Advances in wireless power transfer systems for roadway-powered electric vehicles [J]. *IEEE journal of emerging and selected topics in power electronics*, 2015, 3(1): 18 – 36. DOI: 10.1109/JESTPE.2014.2343674
- [3] SHIN J, SHIN S, KIM Y, et al. Design and implementation of shaped magnetic-resonance-based wireless power transfer system for roadway-powered moving electric vehicles [J]. *IEEE transactions on industrial electronics*, 2014, 61(3): 1179 – 1192. DOI: 10.1109/TIE.2013.2258294
- [4] XIA N H, YUAN Z P, ZHU Y M, et al. Integrated receiver with high misalignment tolerance used in dynamic wireless charging [J]. *IET electric power applications*, 2020, 14(10): 1918 – 1924. DOI: 10.1049/iet-epa.2019.0163
- [5] VU V-B, DAHIDAH M, PICKERT V, et al. A high-power multiphase wireless dynamic charging system with low output power pulsation for electric vehicles [J]. *IEEE journal of emerging and selected topics in power electronics*, 2020, 8(4): 3592 – 3608. DOI: 10.1109/JESTPE.2019.2932302
- [6] COVIC G A, BOYS J T. Inductive power transfer [J]. *Proceedings of the IEEE*, 2013, 101(6): 1276 – 1289. DOI: 10.1109/JPROC.2013.2244536
- [7] MILLER J M, ONAR O C, WHITE C, et al. Demonstrating dynamic wireless charging of an electric vehicle: the benefit of electrochemical capacitor smoothing [J]. *IEEE power electronics magazine*, 2014, 1(1): 12 – 24. DOI: 10.1109/MPEL.2014.2300978
- [8] ZHU Q W, WANG L F, GUO Y J, et al. Applying LCC compensation network to dynamic wireless EV charging system [J]. *IEEE transactions on industrial electronics*, 2016, 63(10): 6557 – 6567. DOI: 10.1109/TIE.2016.2529561
- [9] LEE W Y, HUH J, CHOI S Y, et al. Finite-width magnetic mirror models of mono and dual coils for wireless electric vehicles [J]. *IEEE transactions on power electronics*, 2013, 28(3): 1413 – 1428. DOI: 10.1109/TPEL.2012.2206404
- [10] COVIC G A, BOYS J T. Modern trends in inductive power transfer for transportation applications [J]. *IEEE journal of emerging and selected topics in power electronics*, 2013, 1(1): 28 – 41. DOI: 10.1109/JESTPE.2013.2264473
- [11] POZAR D M. *Microwave engineering*, 4th ed [M]. Hoboken, USA: John Wiley & Sons, 2011
- [12] LAN J Y, YANG N, LI K Y. A novel resonant network for a WPT system with constant output voltage [C]//*IEEE Conference on Energy Internet and Energy System Integration (EI2)*. IEEE, 2017: 1 – 5. DOI: 10.1109/EI2.2017.8245235
- [13] CAI C S, WANG J H, FANG Z J, et al. Design and optimization of load-independent magnetic resonant wireless charging system for electric vehicles [J]. *IEEE access*, 2018, 6: 17264 – 17274. DOI: 10.1109/ACCESS.2018.2810128

Biographies

DUONG Quang-Thang (thang@is.naist.jp) received the BE, ME, and PhD degrees in communications engineering from Osaka University, Japan in 2009, 2011, and 2014, respectively. He is currently an assistant professor with the Nara Institute of Science and Technology, Japan. His research interests include broadband wireless access techniques, channel estimation, information theory, error correcting codes, wireless power transfer, and simultaneous wireless information and power transfer. He is a member of the Institute of Electrical, Information and Communication Engineers (IEICE) and the Institute of Electrical and Electronics Engineers (IEEE). He is the recipient of the Young Engineer Award and the Michiyuki Uenohara Memorial Award from the IEEE Microwave Theory and Techniques Society (IEEE-MTTS) Japan Chapter in 2019.

VO Quoc-Trinh received the BE degree in electronics & telecommunications engineering from the Da Nang University of Science and Technology, Vietnam in 2010, and the ME degree in electronics engineering from International University-Vietnam National University, Vietnam in 2013, and the DEng degree from the Nara Institute of Science and Technology, Japan in 2021. He is currently a lecturer with FPT University Da Nang, Vietnam. His current research interests include wireless power transfer, digital signal processing, and wireless channel estimation.

PHAN Thuy-Phuong received the BE degree in electronics and communication engineering from The University of Da Nang, Vietnam in 2018. She is currently pursuing an ME degree with the Nara Institute of Science and Technology, Japan. Her current research interests include wireless power transfer and wireless communication systems.

OKADA Minoru received the BE degree from the University of Electro-Communications, Japan in 1990, and the ME and PhD degrees from Osaka University, Japan in 1992 and 1998, respectively, all in communications engineering. In 2000, he joined the Graduate School of Information Science, Nara Institute of Science and Technology, Japan, as an associate professor and became a professor. From 1993 to 2000, he was a research associate with Osaka University. From 1999 to 2000, he was a visiting research fellow with the University of Southampton, UK. His research interest is wireless communications, including WLAN, WiMAX, CDMA, OFDM, and satellite communications. He was a recipient of the Young Engineer Award from the Institute of Electrical, Information, and Communication Engineers (IEICE) in 1999. He is a member of the Institute of Television Engineers of Japan, IEICE of Japan, and the Information Processing Society of Japan.



Polarization Reconfigurable Patch Antenna for Wireless Power Transfer Related Applications

SHEN Jun, ZHAO Tianxiang, LIU Xueguan

(Soochow University, Suzhou 215006, China)

DOI: 10.12142/ZTECOM.202202006

<https://kns.cnki.net/kcms/detail/34.1294.TN.20220509.0944.002.html>,
published online May 9, 2022

Manuscript received: 2022-04-18

Abstract: A polarized reconfigurable patch antenna is proposed in this paper. The proposed antenna is a dual cross-polarized patch antenna with a programmable power divider. The programmable power divider consists of two branch line couplers (BLC) and a digital phase shifter. By adjusting the phase of the phase shifter, the power ratio of the power divider can be changed, and thus the feed power to the antenna input port can be changed to reconfigure the antenna polarization. The phase-controlled power divider and the cross dual-polarized antenna are designed, fabricated and tested, and then they are combined to realize the polarized reconfigurable antenna. By moving the phase of the phase shifter, the antenna polarization is reconfigured into vertical polarization (VP), horizontal polarization (HP), and circular polarization (CP). The test is conducted at the frequency of 915 MHz, which is widely used for simultaneous wireless information and power transfer (SWIPT) in radio-frequency identification (RFID) applications. The results demonstrate that when the antenna is configured as CP, the axial ratio of the antenna is less than 3 dB, and when the antenna is configured as HP or VP, the axial ratio of the antenna exceeds 20 dB. Finally, experiments are conducted to verify the influence of antenna polarization changes on wireless power transmitting. As expected, the reconfigured antenna polarization can help improve the power transmitting efficiency.

Keywords: power transfer; branch line coupler; polarization reconfigurable; dual cross polarization antenna

Citation (IEEE Format): J. Shen, T. X. Zhao, and X. G. Liu, "Polarization reconfigurable patch antenna for wireless power transfer related applications," *ZTE Communications*, vol. 20, no. 2, pp. 37 - 42, Jun. 2022. doi: 10.12142/ZTECOM.202202006.

1 Introduction

Nowadays, the wireless power transfer (WPT) technology is widely used to charge electronic devices and activate passive wireless sensors^[1]. The microwave power can be transmitted over long distances under suitable conditions, but it needs the support of high-efficiency antennas with high levels of performance ensured by antenna matching. The matching mentioned here includes not only the matching between the antenna and the feeding circuit, but also the polarization matching between the transmitting antenna and the receiving antenna. Otherwise, in the case of the crossed polarization between the transmitting antenna and the receiving antenna, power will be lost. In order to minimize the adverse effects of cross polarization, antennas are usually designed for circular polarization (CP)^[2]. However, during the wireless power transmission, there is a 3 dB power loss between CP and linear polarization. In order to reduce power loss caused by polarization mismatching for better energy transmission, the antenna polarization reconfiguration technology can be used. There has been a lot of work and research on reconfiguring the antenna po-

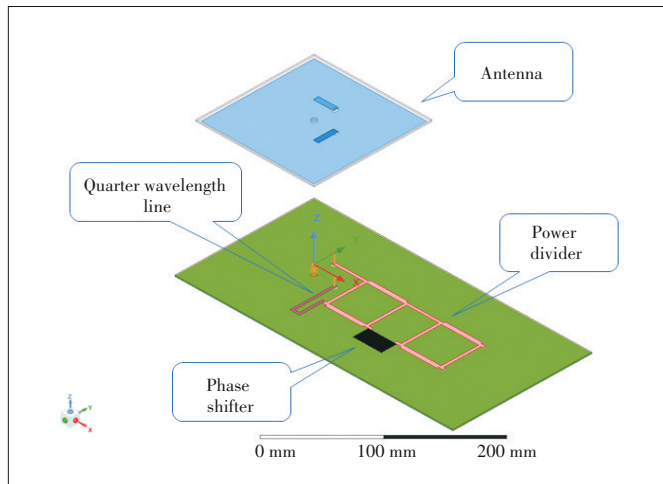
larizations. Re-routing the surface current in the radiating element can reconfigure the antenna polarization^[3-5], but it is easy to generate nonlinear components of the injected signal and cause additional power loss. The reconfigurable feeding network controlled by PIN diodes can also change the antenna polarization from linear to circular^[6]. The radio frequency (RF) switch can be used to select antennas with different polarizations to achieve different antenna polarizations^[7-9]. The 1:1 power divider with or without an additional quarter-wave phase line can drive the linear polarization or CP of the antenna, and the diode can be switched on and off to select the feeding circuit that leads to different polarizations^[10]. Diodes can also choose different quasi-cross-shaped coupling slots to activate different polarizations^[8]. Metasurface applications with feed port changes are another way to reconfigure antenna polarization^[11-12]. In addition to PIN diodes, varactor diodes are selected as a switch to feed different feed networks to achieve different antenna polarizations^[13], and there is also a single-pole double-throw switch that selects feed networks to reconfigure the antenna polarization^[14].

This paper proposes a new type of polarization reconfigurable antenna. Different from previous works that reconfigure the limited number of antenna polarizations, this antenna can be programmed for linear polarization at any angle or for CP. With the programmable antenna polarization, the wireless power can be transferred more efficiently. It also provides the possibility to transfer the wireless power and wireless information with different antenna polarizations to get better isolation between wireless power and wireless information. Section 2 will introduce the design of the proposed antenna, including the power divider design and antenna design, as well as the overall structure of the antenna. In Section 3, the prototype of the antenna is fabricated, the actual performance of the antenna is tested and demonstrated, and the antenna is used to simulate on-site wireless power transfer. Finally, Section 4 concludes the paper.

2 Design Principle of Antenna

2.1 Antenna Structure

The proposed reconfigurable antenna is shown in Fig. 1. The antenna has two substrates, both of which are FR4 (flame retardant 4) materials with dielectric constant $\epsilon_r=4.4$, loss tangent $\tan\delta=0.02$ and a thickness of 1.6 mm. The radiating element is located on the top substrate and consists of a square



▲ Figure 1. Physical configuration of the proposed antenna

patch element and two open stubs. The square patch element is printed on the top substrate. Two stubs are printed on the other side of the top substrate. The capacitors are formed between the two stubs and the square patch, and the RF signal is coupled to the patch element through the capacitor and radiates to the space. The feeding network is located on the bottom substrate and consists of a programmable power divider and quarter-wavelength phase lines. The feeding network and the patch antenna are connected by two copper pillars. One of the copper pillars connects a power divider output and a stub, and the other copper pillar connects the other stub and the other end of the quarter-wavelength phase line. The programmable power divider consists of two branch line couplers (BLCs) and a digital phase shifter. The digital phase shifter is located between the two BLCs and is used to adjust the power ratio between the two outputs of the power divider.

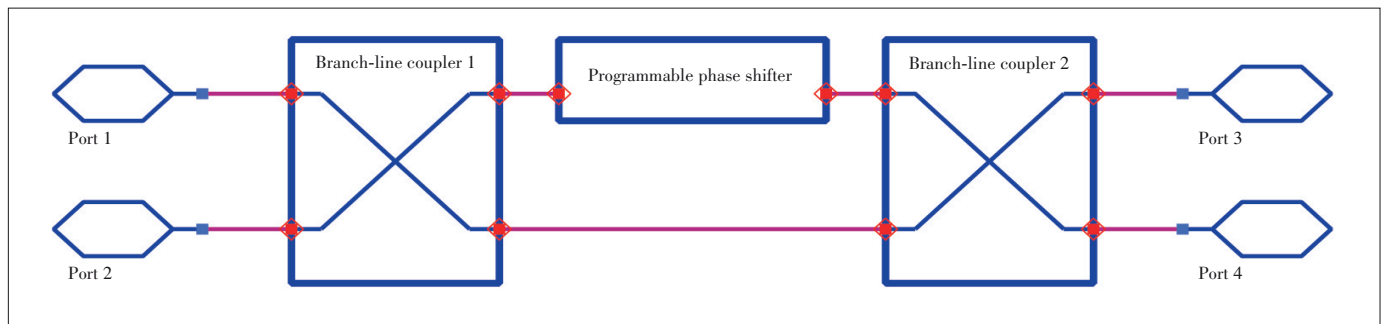
2.2 Design of Power Divider

The schematic diagram of the programmable power divider is shown in Fig. 2. The power is injected into Port 1. Port 2 is terminated by a matching load. The re-allocated power is output from Ports 3 and 4. When the phase of the phase shifter changes, the RF signal power ratio between Ports 3 and 4 of the power splitter will change accordingly.

The scattering matrix of the proposed power divider can be written as follows [15], where φ is the phase of the phase shifter.

$$[S] = je^{\frac{j\varphi}{2}} \begin{bmatrix} 0 & 0 & \sin\left(\frac{\varphi}{2}\right) & -\cos\left(\frac{\varphi}{2}\right) \\ 0 & 0 & -\cos\left(\frac{\varphi}{2}\right) & \sin\left(\frac{\varphi}{2}\right) \\ \sin\left(\frac{\varphi}{2}\right) & -\cos\left(\frac{\varphi}{2}\right) & 0 & 0 \\ -\cos\left(\frac{\varphi}{2}\right) & \sin\left(\frac{\varphi}{2}\right) & 0 & 0 \end{bmatrix}. \quad (1)$$

Therefore, the output power ratio of Ports 3 and 4 can be described as follows.



▲ Figure 2. Schematic of power divider

$$b_3 = je^{\frac{j\varphi}{2}} \sin\left(\frac{\varphi}{2}\right), \tag{2}$$

$$b_4 = -je^{\frac{j\varphi}{2}} \cos\left(\frac{\varphi}{2}\right), \tag{3}$$

$$\text{PowerRatio} = \left(\tan\left(\frac{\varphi}{2}\right)\right)^2. \tag{4}$$

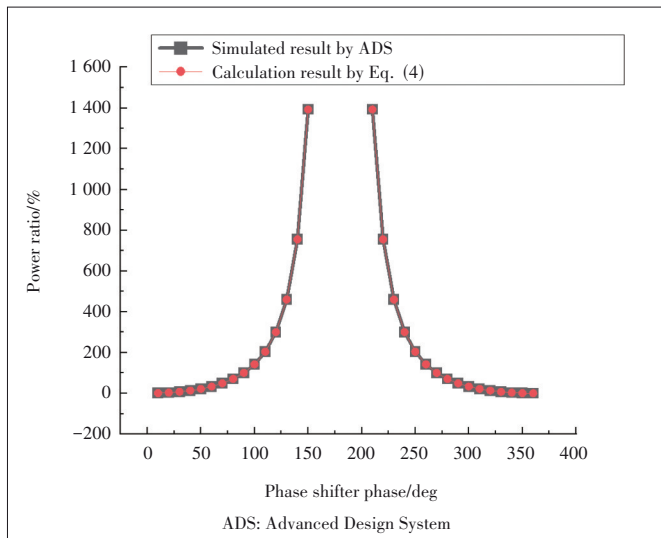
It can be seen from Eq. (4) that the output power ratio is continuous and a function of the phase shifter phase correlation. In order to verify the correctness of Eq. (4), a simulation was carried out in the commercial software Advanced Design System (ADS), and the comparison between simulation and calculation results is shown in Fig. 3. As we can see, these two curves are exactly the same.

There are typical values for this power divider. When the phase of the phase shifter is set to 90 degrees, $\varphi = 90^\circ$, the power ratio is 1, and the power of Port 3 and that of Port 4 are the same. When the phase of the phase shifter is set to 0 degrees, $\varphi = 0^\circ$, the power ratio is 0 and all the radio frequency power is allocated to Port 4 at this time. When the phase of the phase shifter is set to 180 degrees, $\varphi = 180^\circ$, the power ratio is infinite and all the radio frequency power is allocated to Port 3 at this time.

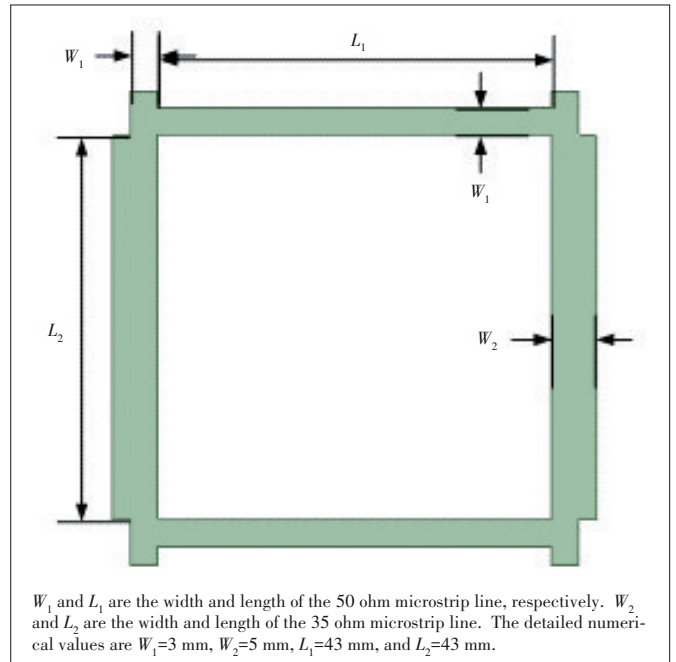
Branch line couplers are designed on the 1.6 mm FR4 board, and the center frequencies are both 915 MHz, as shown in Fig. 4.

2.3 Antenna Geometry

As described in Section 2.1, the patch is on the bottom of the top substrate and the two open stubs are on the top of the top substrate. The top substrate is supported by a conducting post at the center. The open stubs are connected to the two outputs of the power divider by copper pillars and excite the patch capacitively. The antenna geometry is shown in Fig. 5.

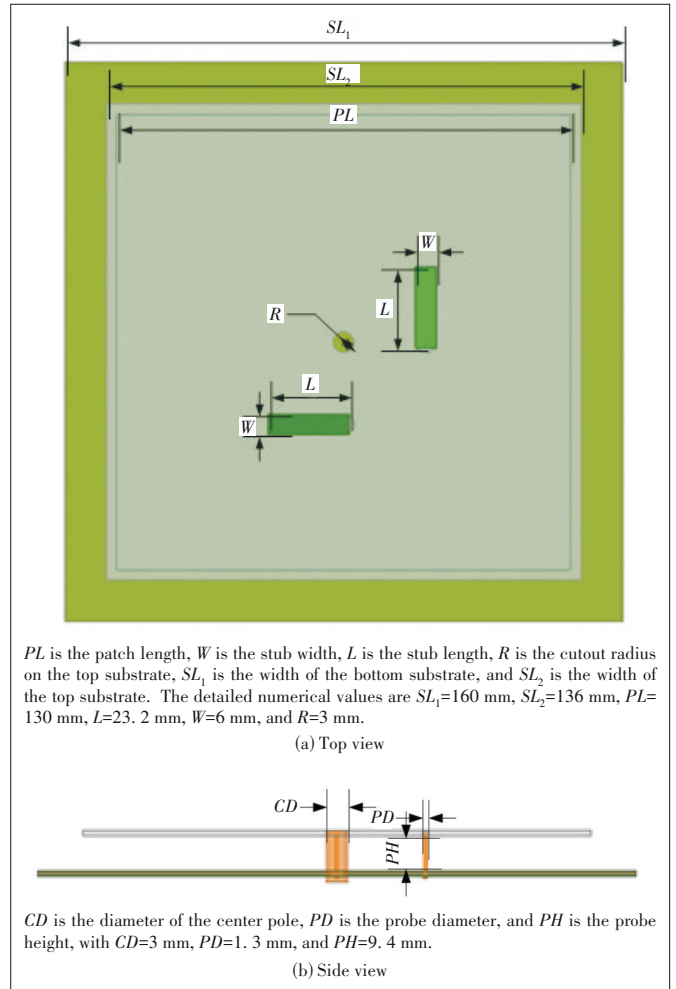


▲ Figure 3. Equation verification: power ratio versus phase



W_1 and L_1 are the width and length of the 50 ohm microstrip line, respectively. W_2 and L_2 are the width and length of the 35 ohm microstrip line. The detailed numerical values are $W_1=3$ mm, $W_2=5$ mm, $L_1=43$ mm, and $L_2=43$ mm.

▲ Figure 4. Branch line coupler structure



PL is the patch length, W is the stub width, L is the stub length, R is the cutout radius on the top substrate, SL_1 is the width of the bottom substrate, and SL_2 is the width of the top substrate. The detailed numerical values are $SL_1=160$ mm, $SL_2=136$ mm, $PL=130$ mm, $L=23.2$ mm, $W=6$ mm, and $R=3$ mm.

(a) Top view

CD is the diameter of the center pole, PD is the probe diameter, and PH is the probe height, with $CD=3$ mm, $PD=1.3$ mm, and $PH=9.4$ mm.

(b) Side view

▲ Figure 5. Cross polarization antenna structure

This antenna is a dual cross polarized antenna with good import impedance match, high isolation and exactly the same feeding structure^[16] which is required by this wireless power transmitting antenna.

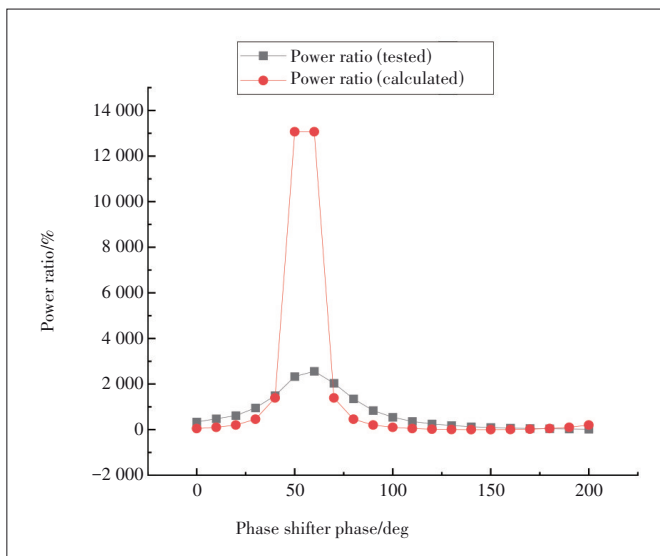
The input probes (copper pillars) excite two orthogonal modes, TM₁₀ and TM₀₁. These two modes have the same resonant frequency which is decided by the patch size. High isolation between the two probes can be achieved by adjusting the probe inductance and stub capacitance. At the frequency decided by the patch size, the TM₁₀ electric field is theoretically zero along the center line of the patch where the feed probe for the TM₀₁ mode is located, and the TM₀₁ electric field is zero along the center line of the patch where the feed probe for the TM₁₀ mode is located. Therefore, high isolation between probes is achieved at the desired frequency.

3 Test Results and Discussion

For the purpose of test and tuning for each part of the proposed antenna, the prototypes of the radiation element, BLC and digital phase shifter are fabricated separately. A quarter wavelength phase cable is used as a 90° phase line and connected to Port 3 of the power divider.

3.1 Test of Power Divider

The power ratio versus the phase of the power divider was measured and the comparison of the measured and calculated results by Eq. (4) is shown in Fig. 6. As the recorded phase values are the absolute phase shifter phases but not the phase differences which are defined as φ between two BLCs, the red curve in Fig. 3 is the calculation result after calibration. When the phase shifter phase is set to an absolute value of 150°, the power ratio is 1, which means that the phase difference between the two paths connecting the two BLCs is 90°. When the phase shifter phase is set to 60°, the power at Port 4 is the

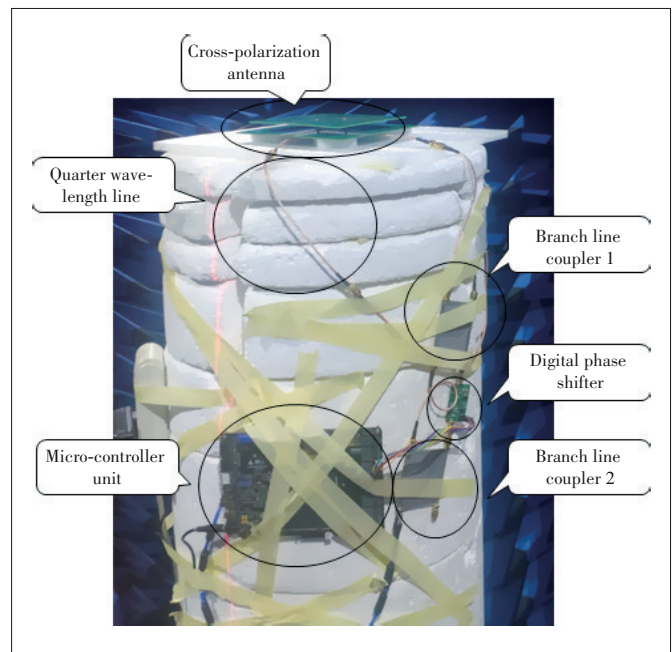


▲ Figure 6. Power divider: power ratio versus phase

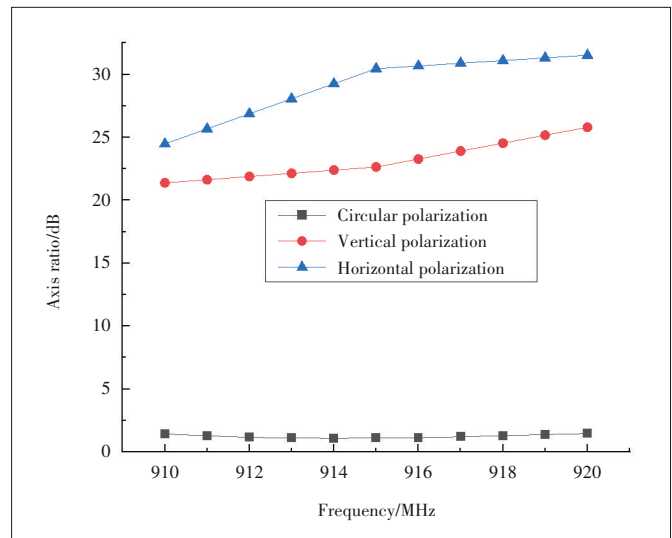
maximum. When the phase shifter phase is set to 200°, the power at Port 3 is the maximum. Therefore, when the absolute value of the phase shifter is set to 60°, the phase difference is 0; when the absolute value of the phase is set to 200°, the phase difference is 180°.

3.2 Test of Antenna

The antenna test was carried out inside a chamber as shown in Fig. 7, and the test frequency is 915 MHz. Typically, when the phase shifter phase was set to 60°, 150° and 200°, the gain and axial ratio of the antenna were tested. The axis ratio (AR) result is shown in Fig. 8. When the phase is 150°, the antenna polarization is configured as CP and the AR is about 1 dB.



▲ Figure 7. Antenna test setup inside the chamber

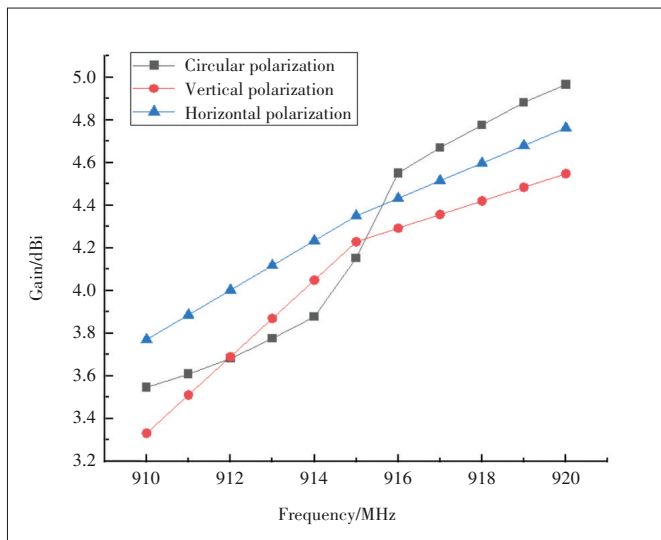


▲ Figure 8. Tested Axis Ratio (AR) results of the proposed antenna

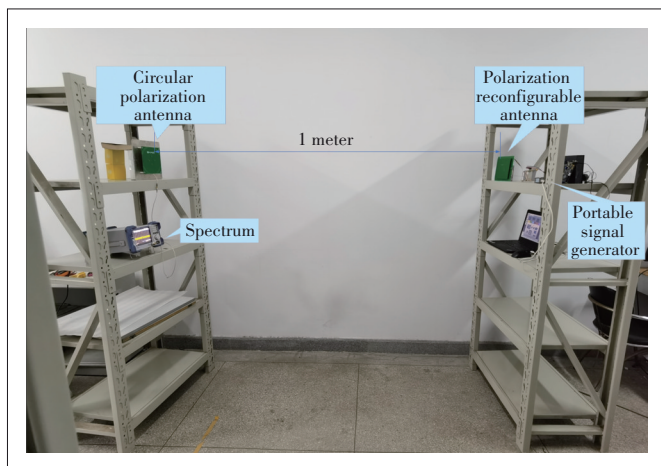
When the phase shifter phase is set to 60° and 230° , the antenna is configured as horizontal polarization (HP) and vertical polarization (VP), and the AR is higher than 20 dB. The results show the reconfigurable antenna polarization controlled by the phase shifter, which is in line with the design expectations. The gain result of the antenna is shown in Fig. 9. The gain of the antenna does not change much when the polarization of the antenna changes. It demonstrates the stable gain performance with the phase shifter phase changing.

3.3 Test of Wireless Power Transfer Field

To verify the effect of antenna polarization during wireless power transfer, a simple simulation test was performed. As shown in Fig. 10, the power transmitter is on the left shelf and consists of a polarization reconfigurable antenna and a signal generator for transmitting wireless signals. The receiving end is on the right shelf and includes a circularly polarized antenna and a spectrum analyzer to measure the received wireless signal. The distance between the transmitter and receiver

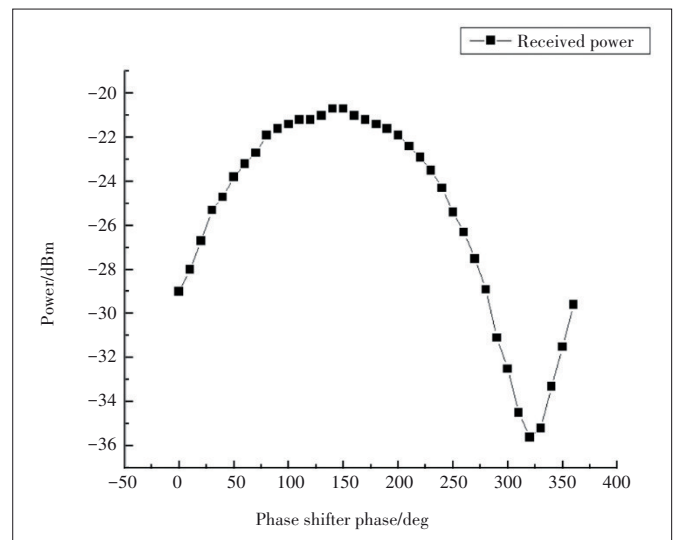


▲ Figure 9. Tested gain results of the proposed antenna



▲ Figure 10. Wireless power transfer field test setup

is 1 m, and they are at the same height. The signal generator generates a 915 MHz wireless signal, which is transmitted to the receiving end through a phase-controlled polarization reconfigurable antenna. The circularly polarized antenna at the receiving end receives the wireless signal, and the spectrum analyzer measures the amplitude of the received wireless signal. With the same frequency and amplitude of the transmitted signal, the phase shifter phase of the transmitting antenna is changed and the amplitude change of the received signal is recorded. The test results are shown in Fig. 11. As expected, when the phase shifter phase is set to 150° , the transmit antenna polarization is configured as circular which is the same as the receive antenna polarization. Meanwhile, the received power is the maximum.



▲ Figure 11. Antenna polarization during wireless power transfer

4 Conclusions

This paper proposes a method to further improve wireless power transfer by reconfiguring the antenna polarization, which is controlled by a programmable phase shifter. Experiments show that different antenna polarizations can be configured through programmable phase shifters without changing the antenna gain performance. The wireless power transmission simulation experiment demonstrates that tuning the transmitting antenna polarization to match the receiving antenna polarization can improve the efficiency of wireless power transmission. This makes it possible for the automated antenna polarization adaption during wireless power transfer.

References

[1] KANG E, HUN SEO C, CHOO H. High gain array antenna using the high-order mode for wireless power transfer applications [C]//IEEE Wireless Power Transfer

- Conference. IEEE, 2020: 205 – 207. DOI: 10.1109/WPTC48563.2020.9295568
- [2] SENNOUNI M A, ZBITOU J, ABOUD B, et al. Efficient rectenna design incorporating new circularly polarized antenna array for wireless power transmission at 2.45 GHz [C]//International Renewable and Sustainable Energy Conference (IRSEC). IEEE, 2014: 577 – 581. DOI: 10.1109/IRSEC.2014.7059874
- [3] ZHANG P P, CUI Y H, LI R L. A novel polarization reconfigurable circularly polarized antenna [C]//IEEE International Symposium on Antennas and Propagation & USNC/URSI National Radio Science Meeting. IEEE, 2017: 2215 – 2216. DOI: 10.1109/APUSNCURSINRSM.2017.8073150
- [4] BEGUM H, WANG X, LU M Y. A polarization-reconfigurable microstrip antenna design based on parasitic pin loading [C]//IEEE Radio and Wireless Symposium. IEEE, 2017: 135 – 137. DOI: 10.1109/RWS.2017.7885967
- [5] KUMAR M S, CHOUKIKER Y K. Circular patch frequency tunable antenna with switching polarization feed configuration [C]//International Conference on Vision Towards Emerging Trends in Communication and Networking (ViTE-CoN). IEEE, 2019: 1016 – 1018
- [6] QI C L, CUI Y H, LI R L. A quad-polarization reconfigurable omnidirectional antenna [C]//IEEE International Symposium on Antennas and Propagation & USNC/URSI National Radio Science Meeting. IEEE, 2018: 863 – 864. DOI: 10.1109/APUSNCURSINRSM.2018.8608619
- [7] WU F, LUK K M. A wideband high-efficiency polarization reconfigurable antenna for wireless communication [C]//IEEE International Symposium on Antennas and Propagation & USNC/URSI National Radio Science Meeting. IEEE, 2017: 1371 – 1372. DOI: 10.1109/APUSNCURSINRSM.2017.8072728
- [8] QIN J H, KONG X K, LIU S B. A wideband polarization reconfigurable antenna using quasi-cross-shaped coupling slot [C]//IEEE International Conference on Computational Electromagnetics. IEEE, 2018: 1 – 3. DOI: 10.1109/COMPEN.2018.8496484
- [9] PAN P X, GUAN B R. A wideband polarization reconfigurable antenna with six polarization states [C]//12th International Symposium on Antennas, Propagation and EM Theory (ISAPE). IEEE, 2018: 1 – 4. DOI: 10.1109/ISAPE.2018.8634224
- [10] JI L Y, QIN P Y, GUO Y J, et al. A wideband polarization reconfigurable antenna for WLAN applications [C]//10th European Conference on Antennas and Propagation (EuCAP). IEEE, 2016: 1 – 3. DOI: 10.1109/EuCAP.2016.7481800
- [11] HUA Y R, LI Z P, LUO Y Y, et al. Design of a polarization-reconfigurable and frequency-tunable active metasurface [C]//International Conference on Microwave and Millimeter Wave Technology (ICMMT). IEEE, 2020: 1 – 3. DOI: 10.1109/ICMMT49418.2020.9386337
- [12] ZHANG Z H, LI M, ZHANG Y M, et al. Design of polarization-reconfigurable antenna based on hybrid periodic metasurface [C]//IEEE International Conference on Computational Electromagnetics (ICCEM). IEEE, 2019. DOI: 10.1109/COMPEN.2019.8779069
- [13] DHANADE Y B, CHOUKIKER Y K. Frequency and polarization reconfigurable antenna for wireless communication [C]//International Conference of Electronics, Communication and Aerospace Technology (ICECA). IEEE, 2017: 287 – 290. DOI: 10.1109/ICECA.2017.8203689
- [14] KUMAR S M, CHOUKIKER Y K. Frequency and polarization reconfigurable microstrip antenna with switching feed configuration [C]//IEEE Indian Conference on Antennas and Propagation (InCAP). IEEE, 2018. DOI: 10.1109/INCAP.2018.8770929
- [15] OCERA A, GATTI R V, MEZZANOTTE P, et al. A MEMS programmable power divider/combiner for reconfigurable antenna systems [C]//European Microwave Conference. IEEE, 2005. DOI: 10.1109/EUMC.2005.1608933
- [16] SON H-W, PARK H, JEON H-G. Design of a circularly polarised radio-frequency identification reader antenna with high return loss [J]. IET microwaves, antennas & propagation, 2010, 5(15): 1844 – 1848. DOI: 10.1049/iet-map.2010.0386

Biographies

SHEN Jun received the BE degree in electronic and communications engineering from Soochow University, China in 2001, and is currently working toward the PhD degree at Soochow University. He is currently a research and teaching assistant with Soochow University. After his undergraduate studies, he spent almost 20 years in the industry as an electronic and communications engineer with Mitec, Powerwave, and Kaelus, where he was involved with advanced filters for cellular radio.

ZHAO Tianxiang received his BS degree in communication engineering from the School of Electronic and Information Engineering, Soochow University, China in 2020. His BS thesis dealt with the design of a single-port double-throw RF switch based on PIN diodes. He has been pursuing his MS degree at Soochow University since Sept. 2020. His research interest is UHF RFID technologies, especially RF switch matrix for bistatic RFID systems.

LIU Xueguan (txdzlxg@suda.edu.cn) received his bachelor's and master's degrees from Xidian University, China in 1986 and 1989 respectively. He is a professor and doctoral supervisor of the School of Electronic Information, Soochow University, China. He is also the director of Suzhou Microwave Millimeter Wave High-tech Research Key Laboratory and the director of Soochow University Radio Frequency and Wireless Communication Institute. His research interests are electromagnetic theory, radio frequency and wireless applications, and antenna design and microwave automatic measurement technology.



A Radio-Frequency Loop Resonator for Short-Range Wireless Power Transmission

WANG Xin¹, LI Wenbo², LU Mingyu³

(1. Chongqing University, Chongqing 400044, China;
2. Nanjing University of Aeronautics and Astronautics, Nanjing 211106, China;
3. West Virginia University Institute of Technology, Beckley, West Virginia 25801, USA)

DOI: 10.12142/ZTECOM.202202007

<https://kns.cnki.net/kcms/detail/34.1294.TN.20220505.1109.002.html>,
published online May 5, 2022

Manuscript received: 2022-04-18

Abstract: A microstrip loop resonator loaded with a lumped capacitor is proposed for short-range wireless power transmission applications. The overall physical dimensions of the proposed loop resonator configuration are as small as 3 cm by 3 cm. Power transmission efficiency of greater than 80% is achieved with a power transmission distance smaller than 5 mm via the strong coupling between two loop resonators around 1 GHz, as demonstrated by simulations and measurements. Experimental results also show that the power transmission performance is insensitive to various geometrical misalignments. The numerical and experimental results of this paper reveal a bandwidth of more than 50 MHz within which the power transmission efficiency is above 80%. As a result, the proposed microstrip loop resonator has the potential to accomplish efficient wireless power transmission and high-speed (higher than 10 Mbit/s) wireless communication simultaneously.

Keywords: loop resonator; lumped capacitive loading; radio frequency; short-range wireless power transmission

Citation (IEEE Format): X. Wang, W. B. Li, and M. Y. Lu, "A radio-frequency loop resonator for short-range wireless power transmission," *ZTE Communications*, vol. 20, no. 2, pp. 43 - 47, Jun. 2022. doi: 10.12142/ZTECOM.202202007.

1 Introduction

Wireless power transmission technology has been pursued by numerous researchers during the past several decades. In short-range wireless power transmission applications (that is, when the distance between a wireless power transmitter and a wireless power receiver is on the order of millimeter or centimeter), the inductive coupling technique is considered a highly efficient and cost-effective approach^[1-2]. Because the inductive coupling technique takes advantage of the non-radiative magnetic field, its operating frequency is typically below 1 MHz. In recent years, some research efforts have been made on using the radio-frequency band to accomplish efficient short-range wireless power transmission^[3-5]. Though the radio-frequency wave tends to be radiative, it is possible to achieve strong coupling between a pair of resonant structures such that the radiation is minimized. The radio-frequency short-range wireless power transmission systems (such as those demonstrated in Refs. [3 - 5]) appear competitive with the inductive coupling systems in terms of compactness and efficiency. A potential advantage associated with radio-frequency coupling is that it may enable broadband simultaneous information and power

transfer. Since the inductive coupling technique relies on low frequencies, it does not support wireless communications with high bit rates. In contrast, the radio-frequency band (on the order of 100 MHz or several GHz, for instance) can be leveraged to accomplish high-speed wireless communications in addition to wireless power transmission.

This paper proposes a compact microstrip loop resonator configuration with lumped capacitive loading for short-range wireless power transmission. The overall physical dimensions of the proposed loop resonator are as small as 3 cm by 3 cm. Simulation and measurement results demonstrate the power transmission efficiency is greater than 80% with a power transmission distance smaller than 5 mm via the strong coupling between two loop resonators around 1 GHz. Experimental data also show that the power transmission performance is insensitive to various geometrical misalignments. Also, the numerical and experimental results of this paper reveal a bandwidth of more than 50 MHz within which the power transmission efficiency is above 80%. As a result, the proposed microstrip loop resonator has the potential to accomplish efficient wireless power transmission and high-speed (higher than 10 Mbit/s) wireless communication simultaneously.

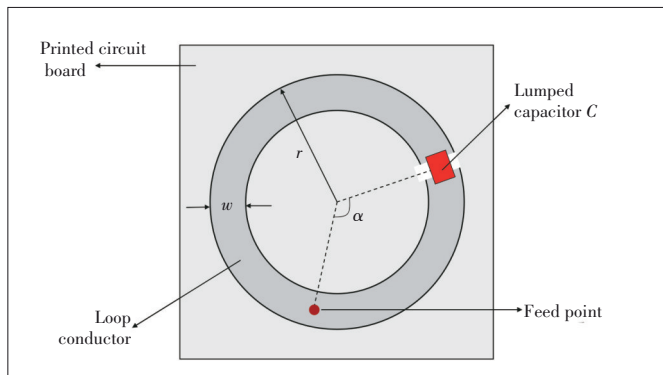
The rest of this paper is organized as follows. The proposed microstrip loop resonator is described and some simulation results are presented to demonstrate the high wireless power

This work was supported in part by the National Natural Science Foundation of China under Grant No. 61871220.

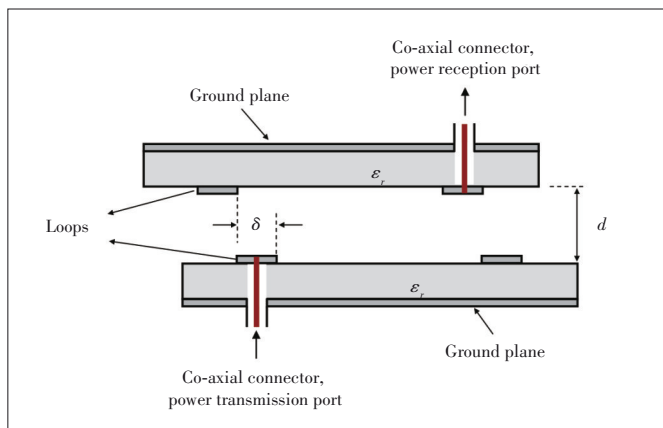
transmission efficiency of the proposed resonator in Section 2. The short-range wireless power transmission performance of the proposed microstrip loop resonator is verified by experimental results in Section 3. Finally, Section 4 concludes the paper.

2 Design of Microstrip Loop Resonator for Wireless Power Transmission

As illustrated by Figs. 1 and 2, a microstrip loop resonator is designed for wireless power transmission over a short distance. Fig. 1 depicts the top view of a circular loop conductor printed over a printed circuit board. The loop has a radius of r and width of w . The printed circuit board has a thickness of h , its substrate has ϵ_r as the dielectric constant, and the bottom side of the board is covered by a solid conducting ground plane. The loop is fed by a co-axial probe through the substrate. A lumped capacitor C is mounted across a gap over the loop. The angle between the gap and the feed point is α with respect to the loop center. Apparently, the loop structure can be modeled as an inductor. The loop structure and the lumped capacitor jointly lead to a resonant circuit. The resonant frequency can be adjusted by the loop's geometry and/or the value of C . In practice, the dependence of the loop resonator's performance on angle α is weak, as the capacitor's



▲ Figure 1. Design of the proposed microstrip loop resonator



▲ Figure 2. Two loop resonators (one transmitting and one receiving) for short-range wireless power transmission

physical size is much smaller than the wavelength. Wireless power could be transmitted between two loop resonators separated by distance d , as shown in Fig. 2. The two loop resonators in Fig. 2 are assumed to be identical to each other. Strong coupling between them is anticipated around the resonant frequency. The parameter δ in Fig. 2 denotes the lateral misalignment between the transmitting loop resonator and receiving loop resonator; in other words, the two loop resonators are aligned with each other when $\delta = 0$.

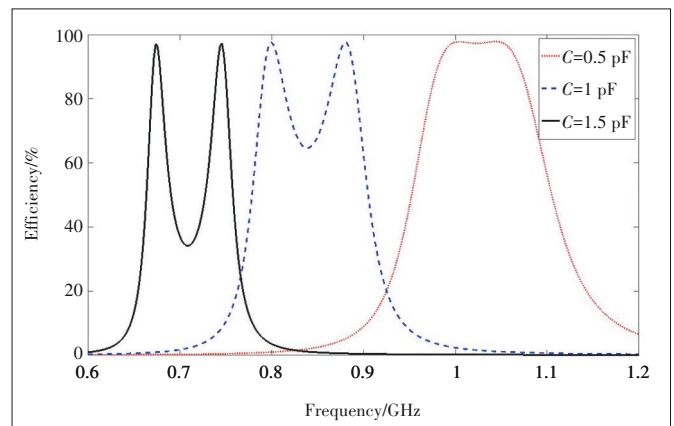
With the parameters tabulated in Table 1, the wireless power transmission configuration in Fig. 2 is simulated. The simulation results of power transmission efficiency are shown in Fig. 3, with three different values of the loading capacitance C . Specifically, the simulated power transmission efficiency is obtained from the scattering parameter S_{21} between the power transmission port (Port 1) and power reception port (Port 2) specified in Fig. 2. When $C = 0.5$ pF, the simulated power transmission efficiency is greater than 95% over a 50-MHz frequency band, which may accommodate wireless communications with a bit rate higher than 10 Mbit/s. The resonant frequency drops when C increases, as anticipated.

In the simulation results in Fig. 3, the two loop resonators are assumed to be perfectly aligned with each other geometrically. When there is an angular misalignment θ between them, the simulated power transmission efficiency data are plotted in Fig. 4. Because the proposed loop resonator has revolutionary symmetry, the power transmission performance is insensitive to the angular misalignment, as evidenced by Fig. 4.

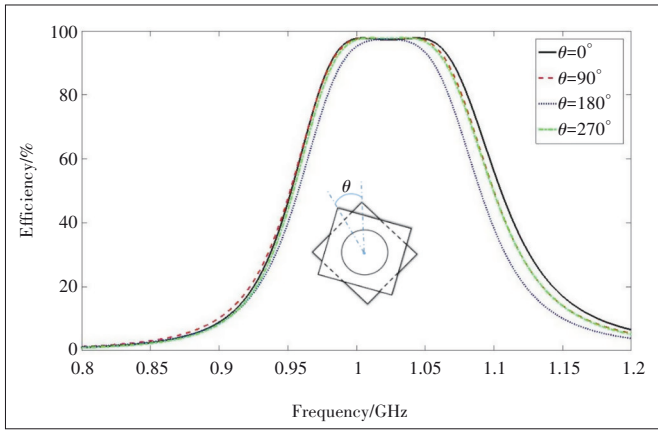
When the lateral misalignment δ between the two loop resonators varies, the simulated power transmission efficiency data are displayed in Fig. 5, with C fixed as 0.5 pF and d fixed as 4 mm. When δ is as large as 1 cm, the maximum power transmission efficiency drops to 50%. It is noted that the ra-

▼ Table 1. One set of parameters of the proposed microstrip loop resonator

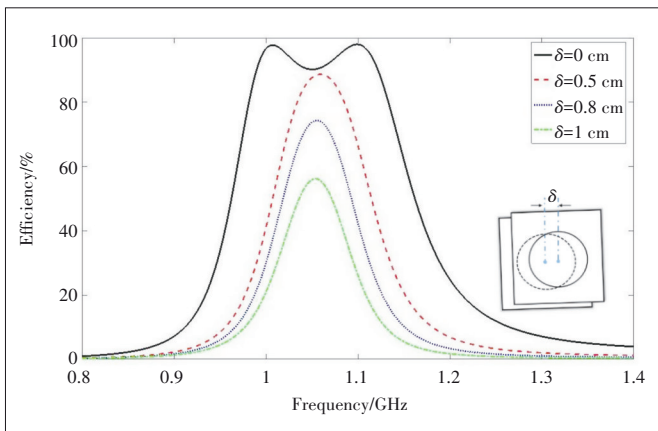
δ	r	w	h	d	α	ϵ_r
0	1 cm	1 mm	1.5 mm	5 mm	120°	3.38



▲ Figure 3. Simulated power transmission efficiency results with three different loading capacitance values and with parameters in Table 1



▲ Figure 4. Simulated power transmission efficiency results with various angular misalignment values of θ , when $C = 0.5 \text{ pF}$ and $d = 5 \text{ mm}$



▲ Figure 5. Simulated power transmission efficiency results with various values of lateral misalignment δ , when $C = 0.5 \text{ pF}$ and $d = 4 \text{ mm}$

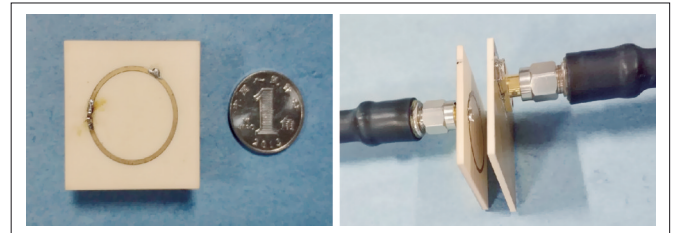
radius of the loop resonators is 1 cm. Thus, the power transmission performance associated with the proposed loop resonators appears quite insensitive to the lateral misalignment.

Overall, our simulation results indicate that 0.5 pF is the optimal capacitance value for C . Specifically, with $C = 0.5 \text{ pF}$ and with insignificant geometrical misalignments, it seems always possible to achieve power transmission efficiency greater than 80% when the distance d is smaller than 5 mm.

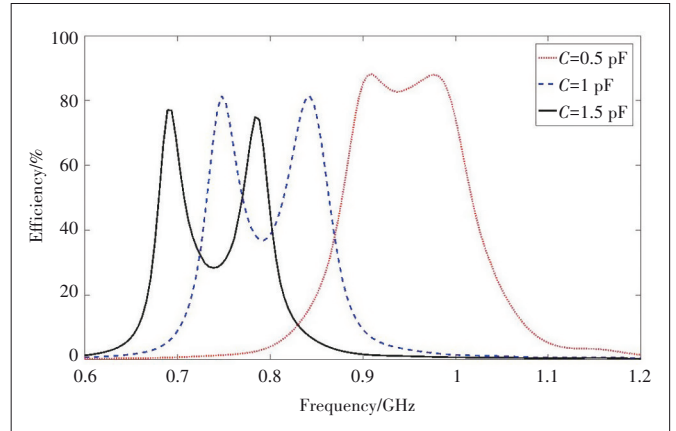
3 Experimental Results

Based on the simulation results presented in the previous section, the microstrip loop resonators with the parameters in Table 1 are fabricated and tested. Each loop resonator is printed over a printed circuit board with the dimension of $3 \text{ cm} \times 3 \text{ cm}$. The substrate material of the printed circuit boards is Arlon 25N (with $\epsilon_r = 3.38$ and loss tangent of 0.0025). Two photos of the fabricated prototype are shown in Fig. 6. The proposed loop resonator configuration is compact and low-cost. The scattering parameter $|S_{21}|$ is measured by a network analyzer manufactured by Radasun Instruments with model number AV3620A.

Fig. 7 shows the measured power transmission efficiency



▲ Figure 6. Photos of fabricated loop resonator and experimental setup



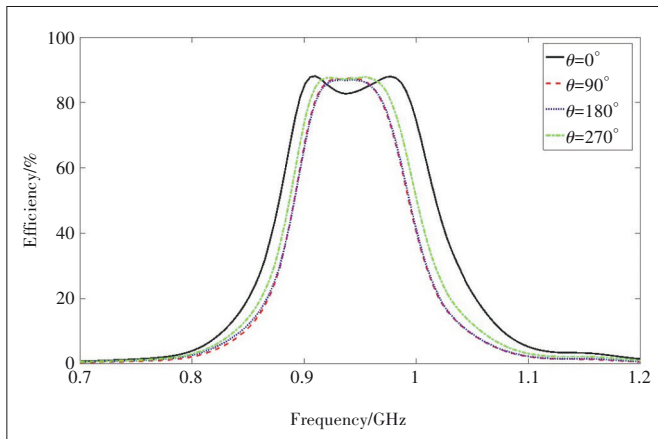
▲ Figure 7. Measured power transmission efficiency results with three different values of loading capacitance and with parameters in Table 1

data with three different values of loading capacitance. The maximum power transmission efficiency for $C = 0.5 \text{ pF}$, 1 pF , and 1.5 pF is 88.1%, 81.5%, and 75%, respectively. The measured power transmission efficiencies in Fig. 7 are lower than the simulated data presented in Fig. 3, which we believe is because certain loss is not included in the simulations, such as the loss of the dielectric substrate, printed conductors, and loading capacitor. As a result of the loss not taken into account by the simulations, the bandwidths in Fig. 7 are greater than those in Fig. 3. For instance, the bandwidth associated with $C = 0.5 \text{ pF}$ is about 60 MHz in Fig. 3 but becomes 85 MHz in Fig. 7.

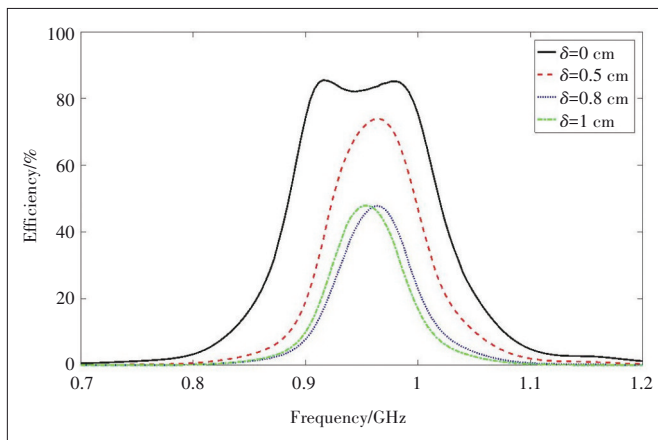
When $C = 0.5 \text{ pF}$, the power transmission efficiency is measured with four different values of angular misalignment θ . The measurement results in Fig. 8 are consistent with the simulation results in Fig. 4: the power transmission performance is insensitive to the angular misalignment.

When $C = 0.5 \text{ pF}$ and $d = 4 \text{ mm}$, the power transmission efficiency is measured with four different values of lateral misalignment δ . The measurement results in Fig. 9 are consistent with the simulation results in Fig. 5: the proposed loop resonator configuration can tolerate large lateral misalignment with respect to the size of the loop resonators.

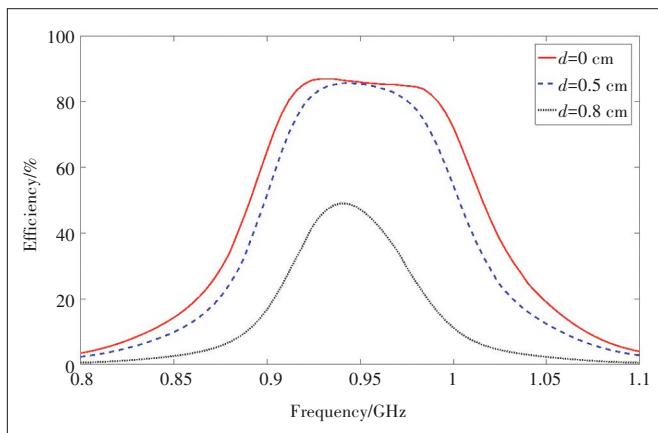
Fig. 10 shows the measured power transmission efficiency data for various values of distance d , with $C = 0.5 \text{ pF}$ and $\delta = 0$. Our measurement results reveal that the maximum power transmission efficiency is always greater than 80% when d is smaller than 5 mm.



▲ Figure 8. Measured power transmission efficiency results with various values of angular misalignment θ , when $C = 0.5$ pF and $d = 5$ mm



▲ Figure 9. Measured power transmission efficiency results with various values of lateral misalignment δ , when $C = 0.5$ pF and $d = 4$ mm



▲ Figure 10. Measured power transmission efficiency results with various values of distance d , when $C = 0.5$ pF and $\delta = 0$

The performance of the proposed loop resonators in this paper is compared with that of the scheme in Ref. [6] which is based on inductive coupling. The loop resonators in this paper and the scheme in Ref. [6] are both proposed for short-distance wireless power transmission applications. The loop resonators in this paper have a simpler physical configuration

than the coils in Ref. [6], and thus are easier to fabricate. The loop resonators in this paper operate around 1 GHz with a bandwidth of more than 50 MHz, and as a result, can accommodate wireless communications with a data rate higher than 10 Mbit/s. The scheme in Ref. [6], in contrast, operates at 107 kHz and thus does not support high-speed wireless information transfer. The radius of the loop resonators in this paper is 1 cm; when the wireless power transmission distance is 5 mm, the wireless power transmission efficiency is higher than 80%; when the lateral misalignment is 1 cm, the wireless power transmission efficiency drops to 50% approximately. The radius of coils in Ref. [6] is 6 cm; when the wireless power transmission distance is 3 cm, the wireless power transmission efficiency is slightly below 80%; when the lateral misalignment is 6 cm, the wireless power transmission efficiency drops to 50% approximately. In summary, the loop resonators proposed in this paper have the potential to enable high-speed wireless communications while offering wireless power transmission performance comparable with the inductive coupling technique in Ref. [6].

4 Conclusions

A compact microstrip loop resonator with lumped capacitive loading is proposed for short-range wireless power transmission around 1 GHz. The overall physical dimensions of the proposed loop resonator are as small as 3 cm by 3 cm. The simulation and measurement results demonstrate the power transmission efficiency is greater than 80% with a power transmission distance smaller than 5 mm. The experimental data also show that the power transmission performance associated with the proposed loop resonators is insensitive to the angular misalignment and can tolerate a large lateral misalignment with respect to the loop size. The numerical and experimental results reveal a bandwidth of more than 50 MHz within which the power transmission efficiency is above 80%. As a result, the proposed microstrip loop resonator has the potential to accomplish efficient wireless power transmission and high-speed (higher than 10 Mbit/s) wireless communication simultaneously.

References

- [1] KURS A, KARALIS A, MOFFATT R, et al. Wireless power transfer via strongly coupled magnetic resonances [J]. *Science*, 2007, 317(5834): 83 - 86. DOI: 10.1126/science.1143254
- [2] JOLANI F, YU Y Q, CHEN Z Z. A planar magnetically coupled resonant wireless power transfer system using printed spiral coils [J]. *IEEE antennas and wireless propagation letters*, 2014, 13(1): 1648 - 1651. DOI: 10.1109/LAWP.2014.2349481
- [3] HEKAL S, ABDEL-RAHMAN A B, JIA H, et al. A novel technique for compact

- size wireless power transfer applications using defected ground structures [J]. *IEEE transactions on microwave theory and techniques*, 2017, 65(2): 591 – 599. DOI: 10.1109/TMTT.2016.2618919
- [4] TAHAR F, BARAKAT A, SAAD R, et al. Dual-band defected ground structures wireless power transfer system with independent external and inter-resonator coupling [J]. *IEEE transactions on circuits and systems II: express briefs*, 2017, 64(12): 1372 – 1376. DOI: 10.1109/TCSII.2017.2740401
- [5] DAUTOV K, HASHMI M, NAURYZBAYEV G, et al. Recent advancements in defected ground structure-based near-field wireless power transfer systems [J]. *IEEE access*, 2020, 8(8): 1298 – 1309. DOI: 10.1109/ACCESS.2020.2991269
- [6] DING S, NIU W Q, GU W. Lateral misalignment tolerant wireless power transfer with a tumbler mechanism [J]. *IEEE Access*, 2019, 7: 125091 – 125100. DOI: 10.1109/ACCESS.2019.2936627

Biographies

WANG Xin (wang.x@cqu.edu.cn) received the BS and MS degrees in electronic engineering from Tsinghua University, China in 2000 and 2002 respectively, and the PhD degree in electrical and computer engineering from Purdue University, USA in 2009. He was a post-doctoral research associate with the Birck Nanotechnology Center, Purdue University from 2009 to 2010. From 2010 to 2021, he was an associate professor with the College of Electronic and Information Engineering, Nanjing University of Aeronautics and Astronautics, China. Currently, he is a professor with School of Electrical Engineering, Chongqing

University, China. His research interests include wireless power transmission, reconfigurable antennas, and RF circuit design.

LI Wenbo received the BS degree in electronic information engineering from Nanjing University of Aeronautics and Astronautics, China in 2019. He is currently an MS candidate in electronic information engineering at Nanjing University of Aeronautics and Astronautics. His research interests include wireless power transmission and RF circuit design.

LU Mingyu received the BS and MS degrees in electronic engineering from Tsinghua University, China in 1995 and 1997 respectively, and the PhD degree in electrical engineering from the University of Illinois at Urbana-Champaign, USA in 2002. From 2002 to 2005, he was a postdoctoral research associate with the Electromagnetics Laboratory, University of Illinois at Urbana-Champaign. He was an assistant professor with the Department of Electrical Engineering, University of Texas at Arlington, USA from 2005 to 2012. He joined the Department of Electrical and Computer Engineering, West Virginia University Institute of Technology, USA in 2012, where he is currently a professor. His research interests include wireless power transmission, radar systems, antenna design, and computational electromagnetics. Dr. LU received the first prize award in the student paper competition of IEEE International Antennas and Propagation Symposium (Boston, USA) in 2001. He served as the chair of Antennas and Propagation Society of the IEEE Fort Worth Section from 2006 to 2011, and received the Outstanding Service Award from the IEEE Fort Worth Section in 2008.



Programmable Metasurface for Simultaneously Wireless Information and Power Transfer System

CHANG Mingyang¹, HAN Jiaqi¹, MA Xiangjin¹,
XUE Hao¹, WU Xiaonan¹, LI Long¹, CUI Tiejun²

(1. Key Laboratory of High-Speed Circuit Design and EMC of Ministry of Education, School of Electronic Engineering, Xidian University, Xi'an 710071, China;

2. State Key Laboratory of Millimeter Waves, Southeast University, Nanjing 210096, China)

DOI: 10.12142/ZTECOM.202202008

<https://kns.cnki.net/kcms/detail/34.1294.TN.2020506.1130.002.html>,
published online May 6, 2022

Manuscript received: 2022-04-18

Abstract: Implementing self-sustainable wireless communication systems is urgent and challenging for 5G and 6G technologies. In this paper, we elaborate on a system solution using the programmable metasurface (PMS) for simultaneous wireless information and power transfers (SWIPT), offering an optimized wireless energy management network. Both transmitting and receiving sides of the proposed solution are presented in detail. On the transmitting side, employing the wireless power transfer (WPT) technique, we present versatile power conveying strategies for near-field or far-field targets, single or multiple targets, and equal or unequal power targets. On the receiving side, utilizing the wireless energy harvesting (WEH) technique, we report our work on multi-functional rectifying metasurfaces that collect the wirelessly transmitted energy and the ambient energy. More importantly, a numerical model based on the plane-wave angular spectrum method is investigated to accurately calculate the radiation fields of PMS in the Fresnel and Fraunhofer regions. With this model, the efficiencies of WPT between the transmitter and the receiver are analyzed. Finally, future research directions are discussed, and integrated PMS for wireless information and wireless power is outlined.

Keywords: programmable metasurface; simultaneously wireless information and power transfers; wireless energy harvesting; wireless power transfer

Citation (IEEE Format): M. Y. Chang, J. Q. Han, X. J. Ma, et al., "Programmable metasurface for simultaneously wireless information and power transfer system," *ZTE Communications*, vol. 20, no. 2, pp. 48 - 62, Jun. 2022. doi: 10.12142/ZTECOM.202202008.

1 Introduction

The wireless communication technology has developed rapidly in the past two decades and has become an indispensable part of our daily lives. Especially with the Internet of Things (IoT) concept, the combination of people, data, and things through networks makes network connections more relevant and valuable. People can interact with various devices more conveniently, which significantly facilitates our production and life and penetrate many fields such as home automation, industrial automation, and medical assistance. With the needs of society and the development of

science and technology, 5G technologies have gradually entered our lives^[1]. Compared with the previous generations of mobile communications, it has a better user experience rate, connection density, peak rate, and other characteristics, which can meet the mobile data growth demands of over a thousand times in the future^[2]. This provides the possibility for the further development of IoT. The future wireless environment will rely on large-scale communications and IoT to meet the increasingly intelligent world, which requires us to deploy millions of low-power sensor networks, actuators, and small computing devices in the environment^[3]. For the sustainable development of the entire wireless sensor network, how to adaptively provide enough energy for a large number of sensors has become a challenging problem we must face now.

To meet the intensive energy requirements for 5G and 6G communications, the concept of simultaneous wireless information and power transfers (SWIPT) was proposed and discussed comprehensively by the communication commu-

This work was supported by the National Key Research and Development Program of China under Grant Nos. 2017YFA0700201, 2017YFA0700202, 2017YFA0700203, and 2021YFA1401001, the 111 Project under Grant No. 111-2-05, National Natural Science Foundation of China under Grant No. 62001342, Key Research and Development Program of Shaanxi under Grant No. 2021TD-07, and Outstanding Youth Science Foundation of Shaanxi Province under Grant No. 2019JC-15.
LI Long and Cui Tiejun are the corresponding authors.

nity^[4-12]. Considering the wireless power conveying and wireless power collection for modern wireless communication networks is the notable characteristic of SWIPT. Thus, theoretical analyses and model constructions on wireless power transfer (WPT) efficiency are the main topics for system level researchers^[13-18]. The fundamentals of SWIPT for a realizable future communication network are established based on linear and nonlinear models, which point out a clear path for the hardware level designers.

The core techniques to implement SWIPT are WPT and wireless energy harvesting (WEH). The WPT technology was firstly proposed by Nikola TESLA. Because of its potential application value, it was selected by the *Technology Review* magazine as one of the ten scientific research directions that would bring considerable changes to human production and lifestyle in the future. In recent two decades, great efforts have been made on the inductive or capacitive coupling^[19-22], achieving a satisfying transmission efficiency of over 70% under several watts^[23]. However, this technique can be classified as a nonradiative type, which operates at kilohertz or megahertz within inductive near-field or Fresnel near-field. Therefore, it is not feasible to apply this resonance method to build a SWIPT network due to the transmission range and the working frequency limitations. Alternatively, the radio frequency (RF) waves can be emitted into free space through antennas, which is coined as the radiative-type WPT^[24-27]. By manipulating the radiated waves, one could direct the wireless energy to targets efficiently^[28]. It is worth noting that when adopting the radiative-type WPT, unlike the nonradiative-type WPT, a receiving device should be applied to harvest energy and convert RF power into direct circuit (DC) power, which is enabled by the WEH technique^[29-31]. The receiving device, which is called the rectenna or rectifying antenna, consists of a conventional receiving antenna and a rectifying circuit. Nevertheless, the rectifying efficiency of the rectenna severely depends on the input power level. Besides, the performance of the receiving antenna also limits the captured wireless power for the rectifying circuit. From the above research, it can be clearly observed that the existing WPT and WEH techniques mainly employ the typical RF and microwave technologies. As a result, both the WPT and WEH developments need a revolutionary methodology.

Metamaterials and metasurfaces were proposed in the early 21st century, providing a new way to observe the physical world^[32]. Previous studies on this topic focused on the basic theory and anomalous phenomenon^[33-35]. Researchers in the WPT and WEH communities keenly adopted these advanced materials to enhance the power transmission efficiency and design novel devices^[36-46]. However, such analog metamaterials possess an intrinsic issue that has fixed functionality after fabrication. In 2014, CUI et al. proposed the programmable metasurface (PMS), introducing digital coding for designing versatile metamaterials^[47]. Using active components on each meta-

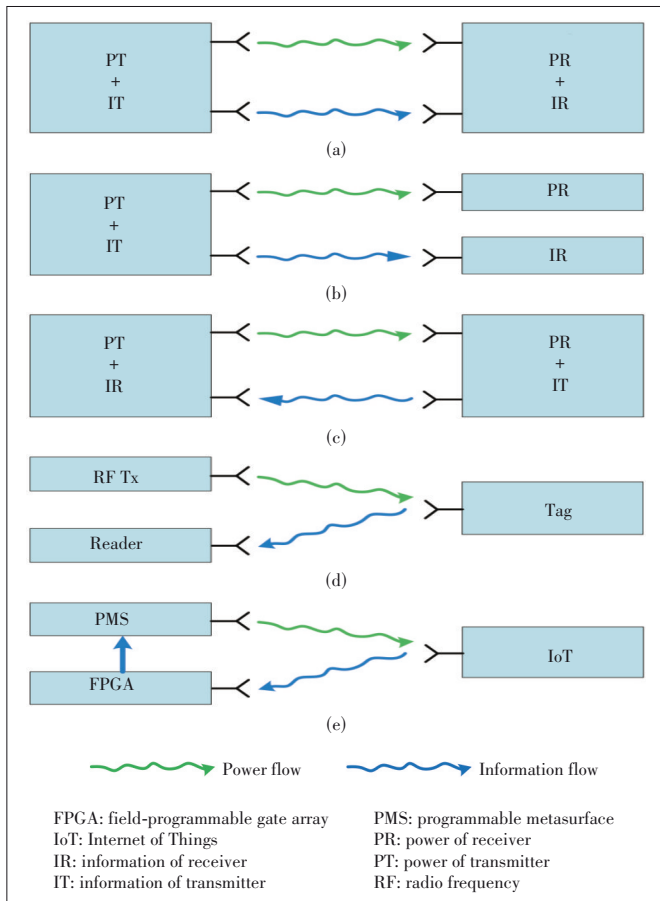
atom, one can regulate the metasurface through an external field-programmable gate array (FPGA), which greatly enriches the original analog metamaterials. Recently, we reported an adaptively smart WPT based on a 2-bit PMS, which could continuously transmit the wireless power to the receiver even though the target was moving^[48]. In addition to transmitting wireless power, wireless information can be envisioned when the space-time-coding (STC) technique is applied to PMS^[49-54]. The STC technique introduces period time modulations to each programmable meta-atom which allows us to modulate digital signals directly without using the traditional communication system architecture^[55-58]. More exciting studies on microwave imaging and recognition were also reported to examine the information PMS^[59-64]. The wireless communication community further extends this methodology to improve the communication channels. Under this application scenario, the information PMS was coined as a reconfigurable intelligent surface (RIS)^[65-67].

So far, we have briefly reviewed the concepts and relationships of SWIPT, WPT, WEH, information PMS, and RIS. However, it can be clearly seen that a system-level solution to SWIPT based on PMS is still unavailable. In this paper, we develop a feasible strategy for SWIPT to integrate wireless information and wireless power using PMS. The rest of this paper is organized as follows. We first overview the PMS-based SWIPT for the future smart cities in Section 2. Then the adaptively smart WPT strategy using PMS in Section 3 is discussed. After that, Section 4 presents the WEH metasurfaces and transmission efficiency analyses for the PMS-based SWIPT. Finally, in Section 5, we direct the future research and conclude this paper.

2 Overview of PMS-Based SWIPT for Smart City

With the advent of the 5G and 6G era, the IoT technology will inevitably usher in new development. People's production and lives will become more intelligent. More and more sensor networks will inevitably become an essential part of our interaction with the outside world. Traditional battery power supply requires manual replacement of the battery periodically to ensure the normal operation of the sensor network, which takes time and effort and causes serious pollution to the environment. The WPT technique is undoubtedly a good solution. To improve its transmission efficiency, this paper proposes a SWIPT system based on PMS. A typical SWIPT system has three forms^[6].

- SWIPT. It can transmit wireless power while transmitting traditional wireless information signals. After the wireless device receives the power, the wireless energy can be stored in the battery of the wireless device after a series of conversions, which can be used to supply power to the corresponding electrical equipment, as shown in Figs. 1(a) and 1(b).
- Wirelessly powered communication networks (WPCNs).



▲ Figure 1. Different forms of wireless information and power transfers (WIPT): (a) SWIPT with co-located receivers; (b) SWIPT with separated receivers; (c) wirelessly powered communication networks (WPCN); (d) wirelessly powered backscatter communication (WPBC); (e) our proposed structure

Power is transmitted through one link, information is transmitted through another link, and the power-collecting link provides power for the information-transmitting link, as shown in Fig. 1(c).

- Wirelessly powered backscatter communication (WPBC). Wireless power is transmitted through one link, and information is transmitted through another link. The backscatter modulation mechanism at the tag reflects and modulates the incoming radio frequency signal and sends it to the reader for communication. This kind of WPBC is widely used in RFID tags, which significantly improves the communication distance of wireless signals. Its disadvantage is that the power consumption of electrical appliances is required to be extremely low, and thus it cannot be widely used in other power scenarios, as shown in Fig. 1(d).

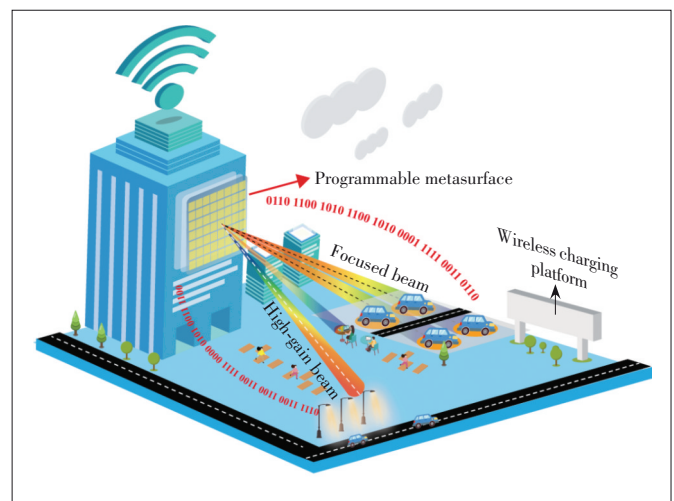
Relying on the three forms, many scholars have conducted in-depth studies. Researchers in the communication field have performed systematic research on the power ratio of energy and information and the modulation method of signals^[11]. Researchers in the antenna field have designed various anten-

nas and ports for wireless power transmission and communication, and fully considered the characteristics of port isolation^[68] and frequency characteristics^[69]. In this paper, we propose a new SWIPT structure, as shown in Fig. 1(e), by combining PMS and IoT applications. The electrical equipment in the IoT sends its position and power information to the FPGA on the transmitting end through sensors. After data processing, the FPGA will adaptively select the appropriate coding and generate the desired beams using PMS, according to the status of the electrical equipment in the external environment.

We propose a strategy to achieve the SWIPT system based on PMS, as illustrated in Fig. 2. When the battery of the electric device is low, its internal sensor will actively transmit position and energy information to the FPGA, and the PMS will supply energy to the sensor network that needs to be powered according to the coding of the FPGA. On the one hand, the PMS can form focused beams to transmit energy for the sensor network in the near-field region; on the other hand, the PMS will generate more efficient high-gain beams when the sensor network is in the far-field region. Through the internal communication between the sensor network and FPGA, the proposed system model enables the PMS to determine the charging target and select the appropriate charging scheme, which will solve the energy supply problem of the sensor network and significantly improve the system efficiency of SWIPT.

3 Adaptively Smart WPT Strategy Using PMS

In the WPT system, the most important thing is the transfer efficiency of the system. In different application scenarios, the power transmission beam has an important impact on efficiency. This paper aims to propose a method based on the location and power information of the device to be charged. PMS can intelligently allocate near-field focused



▲ Figure 2. Application scenarios of the programmable metasurface (PMS) scheme for the simultaneous wireless information and power transfers (SWIPT) system

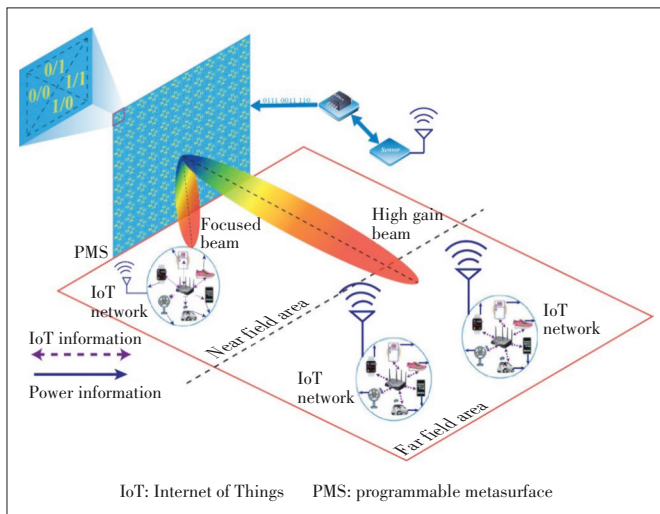
beams and far-field high-gain beams, which can achieve the purpose of efficient power transmission for different charging scenarios.

This system combines the designed PMS and IoT technology to form a new type of SWIPT system. As shown in Fig. 3, PMS can provide a flexible power beam for the device to be charged to improve the power transmission efficiency of the system. Taking the IoT network in the near field area as an example, the introduction of PMS will not affect the internal communication of the IoT network. It can also provide energy for the sensor nodes in the IoT network. When the battery energy of a sensor node is insufficient, it will actively send its energy and location information to the sensor connected to the FPGA.

After analyzing the data, the FPGA will control the switch of the corresponding PIN diodes and focus on the energy receiving part of the sensor node, which can meet the requirements of efficient and accurate energy transmission. It is also suitable for the far-field region. In summary, the proposed PMS model can simultaneously generate far-field high-gain beams and near-field focused beams. Combining PMS with the IoT networks with communication functions can achieve SWIPT, which enriches the design freedom of the power transmission system and greatly improves the power transmission efficiency of the entire system.

3.1 Far-Field WPT Strategy and Numerical Model

More and more attention has been paid to the realization of dynamic metasurfaces to construct advanced reconfigurable devices in recent years. In 2014, the concept of PMS was introduced to control the propagation of electromagnetic waves in a real-time programmable manner. Similar to the digital circuit technology, the different electromagnetic responses of the elements in the programmable metasurface are characterized by discrete digital codes. Therefore, the functional control of the



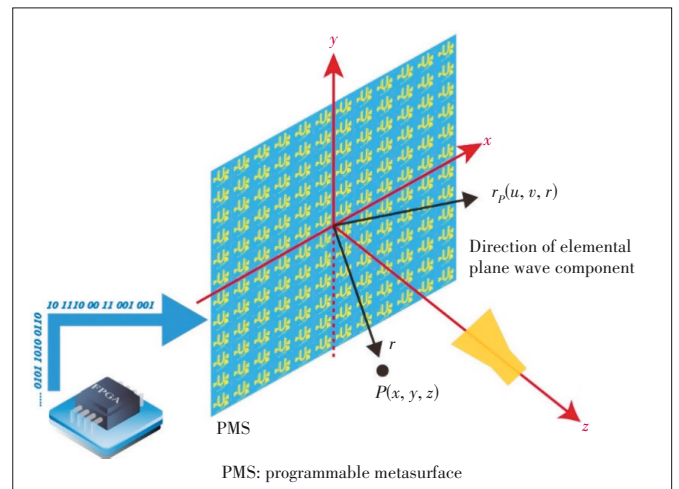
▲ Figure 3. Application of PMS in the IoT network

far-field and the near-field can be realized by changing the digital code sequences.

Here, PMS is located on the plane, and each element can flexibly adjust the phase. A feed antenna is located above the PMS for spatial feeding. By tuning the active device on the programmable element, it can scan the far-field high-gain beam, find the target to be charged in the far-field, and supply power to it. The plane-wave angular spectrum (PWAS) method is used to describe the aperture radiation problem accurately. This method is derived from Fourier optics. When the tangential electric field on the PMS is known, it can be used to calculate the electric field distributions in the far-field and the near-field. According to the requirements of the WPT system for the field distribution, we can use the Fourier transform to decompose the required field distribution into a set of plane waves. The tangential electric field can determine these plane waves on the PMS. This method is also suitable for establishing a PMS far-field wireless energy transfer model. In this part, we will use PMS to generate a high-gain beam pattern capable of beam scanning. To generate the desired field distribution, the analysis of the far-field calculation using the PWAS method is shown in Fig. 4. During the analysis, we assume that the tangential electric fields of the two orthogonal E -field components $E'_x(x, y)$ and $E'_y(x, y)$ are known. PMS has $M \times M$ elements along the x -axis and y -axis, and the element size is $p_x \times p_y$. With these assumptions, we can obtain^[70]

$$\vec{E}(x, y, z) = \int_{-\infty}^{\infty} \int_{-\infty}^{\infty} \left[\left(\hat{x} - \frac{u}{\gamma} \hat{z} \right) F_x(u, v) + \left(\hat{y} - \frac{v}{\gamma} \hat{z} \right) \times F_y(u, v) \right] \exp(-jk_0 \vec{r}_p \cdot \vec{r}) dudv, \quad (1)$$

where $F_x(u, v)$, and $F_y(u, v)$ are the spectrum functions for x - and y -directions, and k_0 is the free-space wave number. \vec{r}_p represents the elemental position vector and \vec{r} is the field vector.



▲ Figure 4. Configuration for far-field calculation using plane-wave angular spectrum (PWAS) approach

This equation can be calculated using the stationary phase method on the three directional components. Thus, we have

$$\vec{E}(x,y,z) \approx j2\pi \frac{\exp(-jk_0 r)}{k_0 r} [(\gamma \hat{x} - u \hat{z})F_x(u,v) + (\gamma \hat{y} - v \hat{z})F_y(u,v)]. \quad (2)$$

In the spherical coordinate system, the above equation can be expressed as

$$\vec{E}(\theta, \varphi) \approx j2\pi \frac{\exp(-jk_0 r)}{k_0 r} \cdot [(\cos \varphi \hat{\theta} - \cos \theta \sin \varphi \hat{\phi})F_x(u,v) + (\sin \varphi \hat{\theta} + \cos \theta \cos \varphi \hat{\phi})F_y(u,v)]. \quad (3)$$

Fourier transform can be used to describe the spectral functions

$$F_{xy}(u,v) = \frac{1}{\lambda^2} \iint_{\text{surf}} E'_{xy}(x,y) \exp[jk_0(ux + vy)] dx dy, \quad (4)$$

where $u = \sin\theta\cos\phi$, and $v = \sin\theta\sin\phi$. This formula is used to express the integral on the surface of the PMS. In addition, because PMS is a periodic structure, we can calculate the result of an element and perform a summation calculation on it. We perform the coordinate conversion based on the above assumptions and analysis process. The specific expression is as follows.

$$\begin{aligned} x &= x' + mp_x - \frac{(M-1)p_x}{2}, \quad m = 1, 2, 3, \dots, M, \\ y &= y' + np_y - \frac{(N-1)p_y}{2}, \quad n = 1, 2, 3, \dots, N, \end{aligned} \quad (5)$$

and

$$-\frac{p_x}{2} \leq x' \leq \frac{p_x}{2}, \quad -\frac{p_y}{2} \leq y' \leq \frac{p_y}{2}. \quad (6)$$

Then, Eq. (4) can be rewritten as

$$\begin{aligned} F_{xy}(u,v) &= C \cdot \sum_{m=0}^{M-1} \sum_{n=0}^{N-1} [\exp[jk_0(ump_x + vnp_y)] \cdot I], \\ C &= \frac{1}{\lambda^2} \exp\left\{-j\frac{k_0}{2}[u(M-1)p_x + v(N-1)p_y]\right\}, \\ I &= p_x p_y \text{sinc}\left(\frac{k_0 u p_x}{2}\right) \text{sinc}\left(\frac{k_0 v p_y}{2}\right) E'_{xy}(x_c, y_c), \end{aligned} \quad (7)$$

where E'_{xy} is the tangential E -field on each PMS element, and it can be expressed by

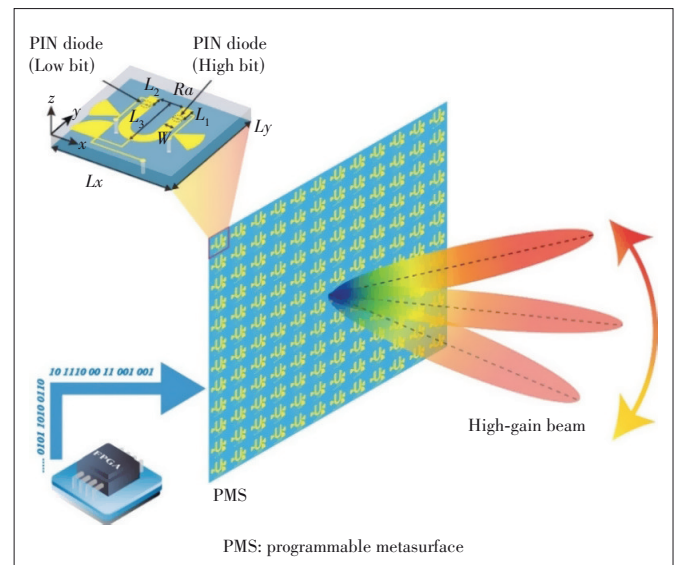
$$\begin{bmatrix} E_x^{m,n} \\ E_y^{m,n} \end{bmatrix} = \begin{bmatrix} S_{TE, TM}^{m,n} \end{bmatrix} \begin{bmatrix} E_x^{inc} \\ E_y^{inc} \end{bmatrix}, \quad (8)$$

where E_{xy}^{inc} is the incident tangential electric field of the source, and $S_{TE, TM}^{m,n}$ is the element reflection coefficient which can be simulated with the full-wave simulator. To control the high-gain beam flexibly, we need to control the switch of the active devices on the PMS to produce a phase shift in each unit to form an equal wavefront phase in the desired area. The phase shift can be described as

$$\Phi(x_m, y_n) = -k_0(\sin\theta_0 \cos\varphi_0 \times x_m + \sin\theta_0 \sin\varphi_0 \times y_n) + k_0 d_{mn}, \quad (9)$$

where (θ_0, φ_0) is the beam pointing direction and d_{mn} is the distance from the feed horn to each element. For the digital coding PMS, Φ should be quantized^[71]. When the phase shifts are calculated, the $S_{TE, TM}^{m,n}$ of each element is known. Therefore, far-field high-gain beams are generated when the distance from the PMS is greater than $2D^2/\lambda$, where λ is the wavelength and D is the largest dimension of the metasurface. The PMS radiation field can be calculated by Eqs. (3), (4), and (8).

According to the above theoretical analysis, through the PWAS mode calculation, a model with a frequency of 5.8 GHz is designed, as shown in Fig. 5. The PMS has 20×20 2-bit meta-atoms. Geometrical parameters are separately $L_x = L_y = 30$ mm, $L_1 = 3.3$ mm, $L_2 = 2.6$ mm, $L_3 = 16.2$ mm, $w = 3$ mm, and $R_a = 4.5$ mm. The entire array is printed on an F4B dielectric substrate with a thickness of 2 mm, the dielectric constant of which is 2.65, and the loss tangent angle is 0.005. The PIN diode model used is SMP1340. By combining the switchable states of the PIN diodes of low bits and high bits, the four states are termed as “00”, “01”, “10”, and “11” respectively. The

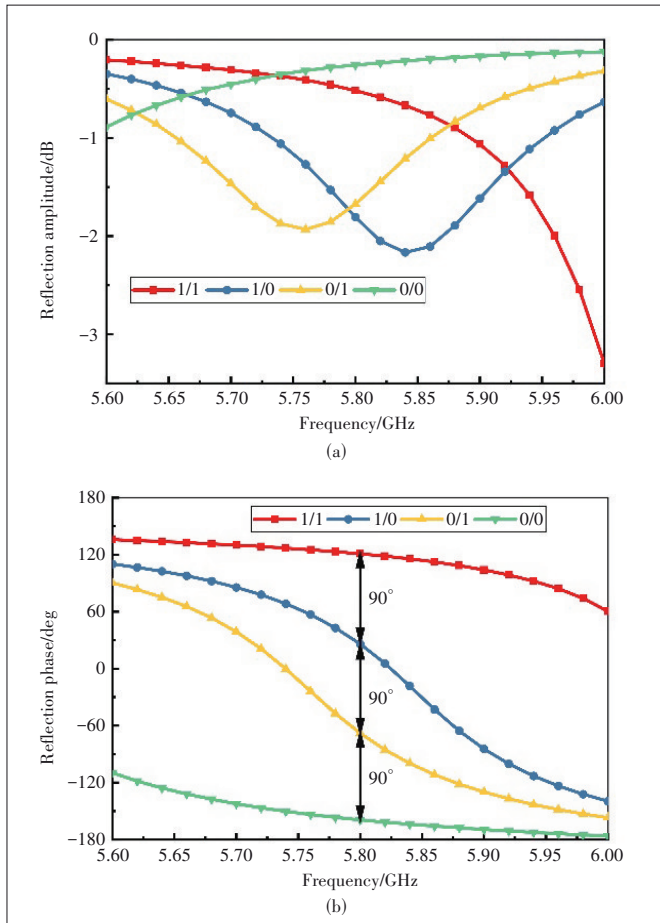


▲ Figure 5. Schematic diagram of the high gain beam structure

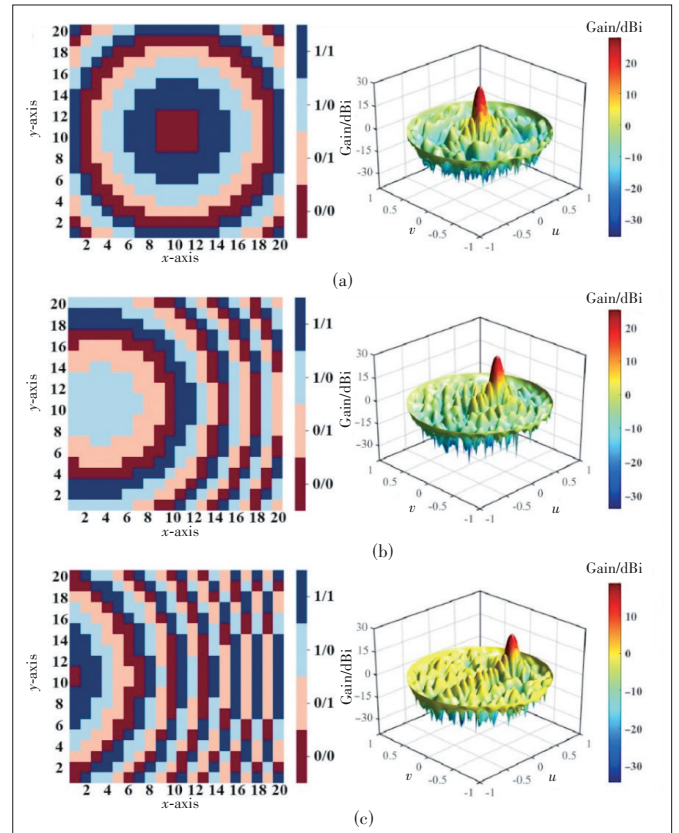
simulation results are shown in Fig. 6. We know that the phase differences of the four states are 90° at 5.8 GHz. The reflection amplitudes of “01” and “10” are close to -2 dB, and “00” and “11” states are less than 0.6 dB. The reason for this phenomenon may be that the two states of “01” and “10” work in a strong resonant mode, so their reflection amplitude fluctuates more obviously. Based on the above element model, we design a PMS array with 20×20 elements, which can realize beam scanning in the far-field area. Fig. 7 shows the coding patterns at 0° , 20° , and 40° , and the corresponding electric field distribution in the far-field area. To further verify the performance of the PMS array, we analyze its beam scanning characteristics, as shown in Fig. 8. It can be seen that there is a good scanning performance in the range of $\pm 60^\circ$, which provides more favorable conditions for the wireless energy transmission.

3.2 Near-Field WPT Strategy and Numerical Model

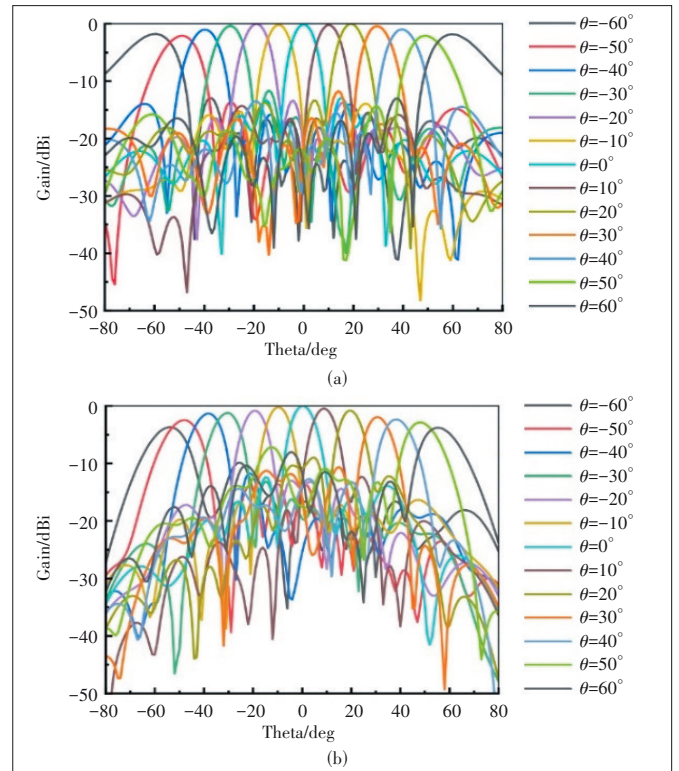
A large number of studies have shown that when the target to be charged is in the near-field area of the antenna, the focused beam has higher power transfer efficiency. Through further analysis, it is concluded that the PWAS method is also suitable for calculating the electric field distribution in the near-



▲ Figure 6. Structure of the proposed 2-bit element: (a) reflection amplitude and (b) reflection phase



▲ Figure 7. Coding patterns and E -field distributions under different angles: (a) $\theta=0^\circ$, (b) $\theta=20^\circ$ and, (c) $\theta=40^\circ$



▲ Figure 8. Normalized radiation patterns of programmable metasurface (PMS): (a) E -plane beam-scanning and (b) H -plane beam-scanning

field area. Fresnel diffraction theory is applied when the distance from the PMS is greater than $0.62\sqrt{D^3/\lambda}$ and less than $2D^2/\lambda$, and we can get the following approximate expression:

$$\gamma = \sqrt{1 - u^2 - v^2} \approx 1 - \frac{1}{2}(u^2 + v^2). \quad (10)$$

For the state of x polarization, we can use Eqs. (10) and (1) to get:

$$E_x = \exp(-jk_0 z) \int_{-\infty}^{\infty} \int_{-\infty}^{\infty} F_x(u, v) \exp\left[j\frac{k_0 z}{2}(u^2 + v^2)\right] \exp[-jk_0(xu + yv)] dudv. \quad (11)$$

After the calculation using the two-dimensional convolution theorem, the integral of the above formula can be rewritten as:

$$E_x = \frac{j}{\lambda_z} \exp(-jk_0 z) \int_{-\infty}^{\infty} \int_{-\infty}^{\infty} E'_x(u, v) \exp\left\{-\frac{jk_0}{2z}[(x-u)^2 + (y-u)^2]\right\} dudv. \quad (12)$$

Eq. (12) can be discretized on every element of the PMS surface using Eqs. (5) and (6), resulting

$$E_x(x, y, z) = \frac{j}{2} \exp(-jk_0 z) \sum_{m=0}^{M-1} \sum_{n=0}^{N-1} \left\{ E'_x(x_m, y_n) \cdot \left\{ [C(t_2) - jS(t_2)] - [C(t_1) - jS(t_1)] \right\} \right. \\ \left. \cdot \left\{ [C(t'_2) - jS(t'_2)] - [C(t'_1) - jS(t'_1)] \right\} \right\}, \quad (13)$$

where

$$C(u) = \int_0^u \cos\left(\frac{\pi}{2}t^2\right)dt, S(u) = \int_0^u \sin\left(\frac{\pi}{2}t^2\right)dt$$

$$t_1 = \sqrt{\frac{k_0}{\pi z}} \left(\frac{p_x}{2} + x - mp_x + \frac{(M-1)p_x}{2} \right)$$

$$t_2 = \sqrt{\frac{k_0}{\pi z}} \left(-\frac{p_x}{2} + x - mp_x + \frac{(M-1)p_x}{2} \right)$$

$$t'_1 = \sqrt{\frac{k_0}{\pi z}} \left(\frac{p_y}{2} + y - np_y + \frac{(N-1)p_y}{2} \right)$$

$$t'_2 = \sqrt{\frac{k_0}{\pi z}} \left(-\frac{p_y}{2} + y - np_y + \frac{(N-1)p_y}{2} \right). \quad (14)$$

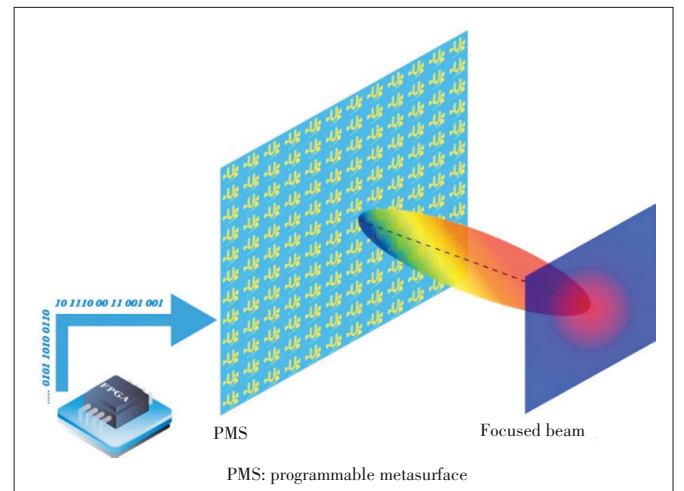
With these equations, we can analyze the electric field dis-

tribution in the near-field since the phase shift on each element is given.

To verify the validity of the near-field focusing formula of metasurfaces, the approximate solution of the Fresnel zone given by PWAS is used to design near-field electromagnetic energy focusing with metasurfaces. The designed model works at 5.8 GHz, and its element size is the same as the aforementioned high-gain beam antenna. The PMS is placed on the xoy plane and propagates along the z -axis, as shown in Fig. 9. According to Eq. (13), we have completed the flexible control of the focused beam, a dual-focus focused beam, and a single-focus focused beam at different positions. Figs. 10 (a), (d), (g) and (b), (e), (h) respectively show that the focus is at (0 m, 0 m, 0.5 m) and (0.2 m, 0.2 m, 0.5 m) of the coding patterns. The electric field distribution diagram of the PMS is at $z = 0.5$ m and on the xoz plane. The simulation data show that the PMS has a certain focus and scan functions, and the WPT system can supply power to charging equipment in different locations.

Figs. 10 (e), (f), and (i) describe the coding patterns of the dual focus (-0.2 m, -0.2 m, 0.5 m) and (0.2 m, 0.2 m, 0.5 m); their electric field distribution diagrams are at $z=0.5$ m and on the xoz plane, which indicates the PMS can supply power to multiple charging targets. Comprehensive analysis shows that the focused beam can converge most of the energy to one point, which meets our wireless power transmission requirements in the near-field area. It is worth pointing out that other quasi-non-diffraction beams, such as the Bessel beam and the Airy beam, can be flexibly regulated by PMS for wireless power transmission^[72].

Because the size of the PMS in the simulation scheme is too large and inconvenient for processing, in order to verify the scheme's feasibility, we fabricate a PMS with 12×12 meta-atoms^[48]. The size of PMS is 380×410 mm², as shown in Fig. 11(a). All DC biasing lines are led to the back of the



▲ Figure 9. Schematic diagram of the focused beam in the near-field of PMS

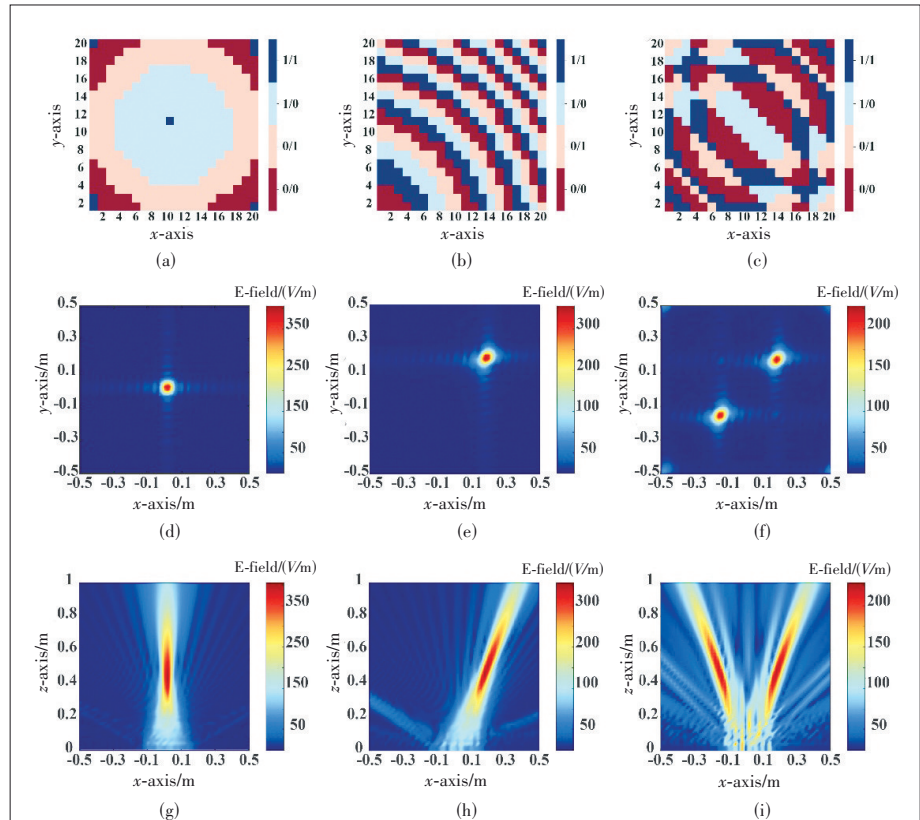
PMS. The 144 biasing lines for the low bit or high bit are grouped into twelve 2×7 sockets, as shown in Fig. 11(b). There are twelve ports for the DC biasing lines and two grounding ports for each socket. The spots that can be controlled programmatically are measured in an anechoic chamber. The configuration of the measurement setup is shown in Fig. 11(c). For the convenience of observation, we normalize the electric field distribution obtained from the test. As shown in Fig. 12, all focal spots can be observed at the expected positions, indicating that the focal spot can be programmatically determined. It is fully proved that the scheme can solve the problem of multi-target WPT.

4 WEH Metasurfaces and Transmission Efficiency Analyses

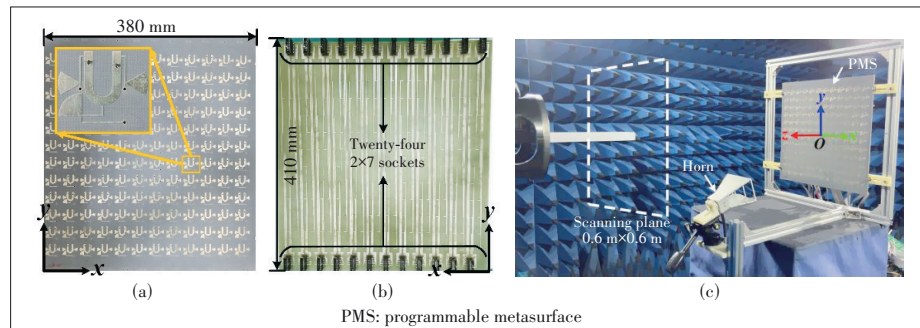
4.1 Design of Rectifying Metasurface

WEH is an important part of the SWIPT system. It is mainly composed of a receiving antenna and a rectifier circuit. After continuous exploration by many scientific researchers for the receiving antenna, many different types of receiving antennas have been proposed. Its compact structure, low sensitivity to the incident angle, polarization, and other characteristics have attracted wide attention^[73-75], and it can meet the needs of WEH to a large extent. The main function of the rectifier circuit is to convert the RF energy captured by the receiving antenna into DC energy to provide usable energy for electrical equipment. To verify the feasibility of the strategy proposed in this paper, we propose a rectifying metasurface. First of all, we design a ring resonator with stubs. The operating frequency is 5.8 GHz. When the metasurface energy harvesting structure is designed, the Floquet port in ANSYS is used in conjunction with periodic boundary conditions to calculate the S parameters of the infinite period metasurface, energy harvesting efficiency, and other related parameters.

After simulation and optimization, we get the structure of the metasurface element, as shown in Fig. 13(a). The dielectric substrate used is F4B, the relative permittivity of which is 2.65, and the dielectric loss tangent is 0.001. The structure



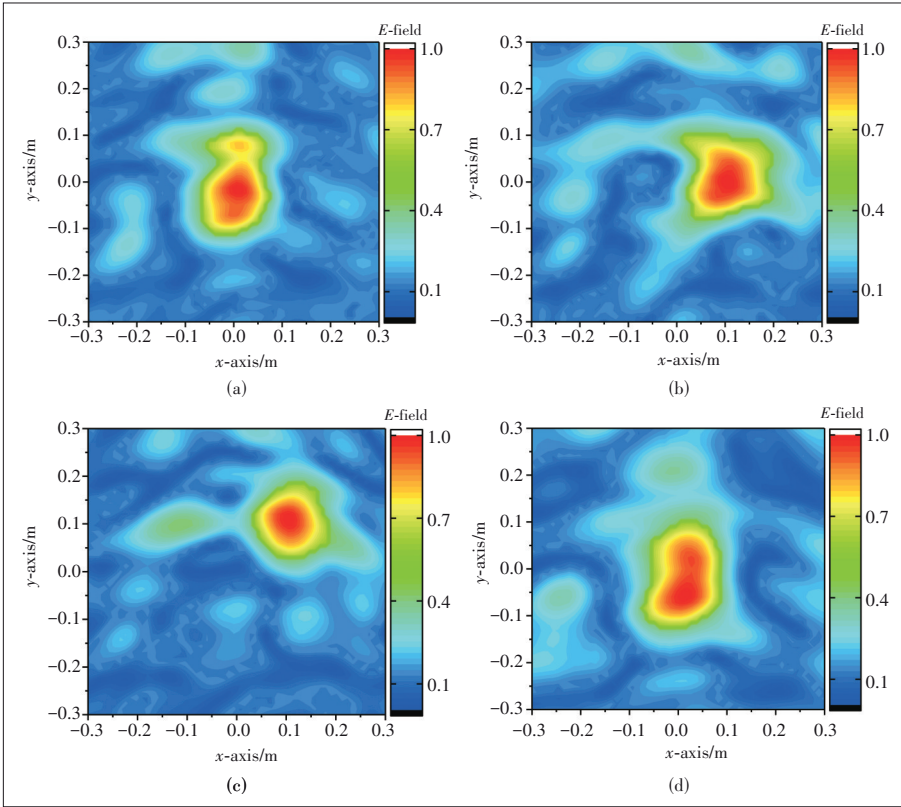
▲ Figure 10. Coding patterns and E -field distribution of the near-field focused beam, where (a), (d) and (g) describe the focus $(0 \text{ m}, 0 \text{ m}, 0.5 \text{ m})$; (b), (e) and (h) describe the focus $(0.2 \text{ m}, 0.2 \text{ m}, 0.5 \text{ m})$; (c), (f) and (i) describe the dual focus $(0.2 \text{ m}, 0.2 \text{ m}, 0.5 \text{ m})$ and $(-0.2 \text{ m}, -0.2 \text{ m}, 0.5 \text{ m})$



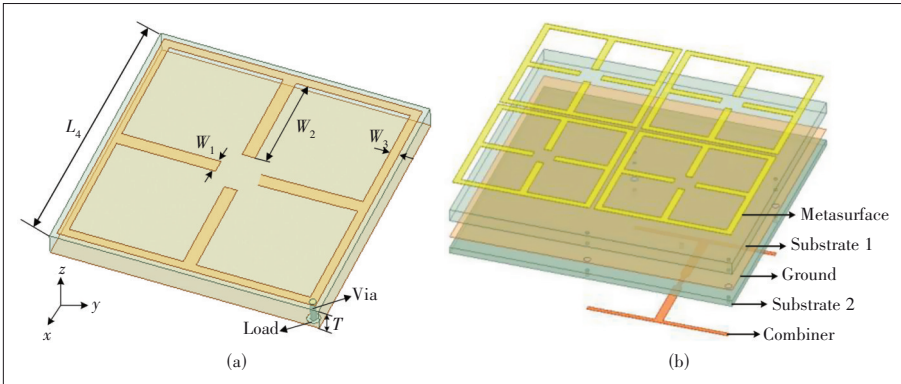
▲ Figure 11. Fabricated 2-bit PMS: (a) front view, (b) back view, and (c) near-field measurement scene for focal spots in the anechoic chamber

size is as follows: $L_4=16 \text{ mm}$, $W_1=0.53 \text{ mm}$, $W_2=4.52 \text{ mm}$, $W_3=0.57 \text{ mm}$, $T=1 \text{ mm}$, and $\text{Load}=430 \Omega$. A via is set on the diagonal of the element, and the energy collected by the metasurface is concentrated on the load, the radius of which is 0.2 mm . It is worth noting that we can flexibly design the working frequency and matching load of the metasurface by adjusting metasurface structure parameters. The harvesting efficiency of the metasurface can be calculated as^[76]

$$\text{Efficiency} = \frac{P_L}{P_R} \times 100\%. \quad (15)$$



▲ Figure 12. Measured results of the focusing E -field distribution of the 2-bit PMS at (a) (0 m, 0 m, 0.75 m), (b) (0.1m, 0 m, 0.75 m), (c) (0.1 m, 0.1 m, 0.75 m), and (d) (0 m, 0 m, 0.9 m)



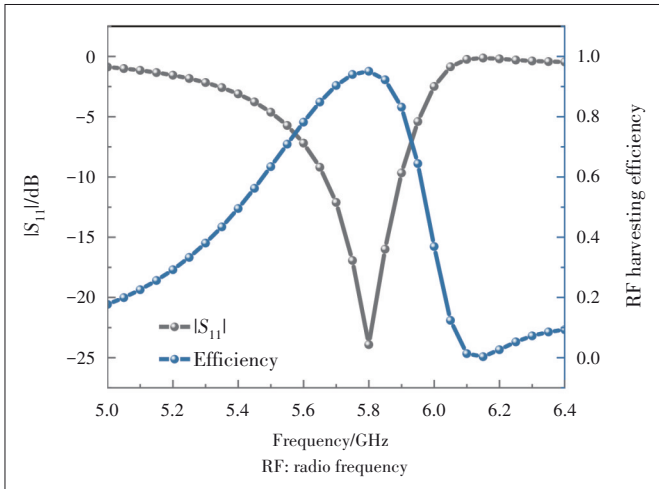
▲ Figure 13. Schematic diagram of metasurface structure: (a) element size and (b) array structure

Among them, P_L is the energy collected by the load, and P_R is the energy incident on the metasurface, which can be obtained by integrating the Poynting vector along the incident direction on the metasurface. Fig. 14 shows the reflection coefficient $|S_{11}|$ of the metasurface and the harvesting efficiency of RF energy. It can be seen from the results that the impedance matching performance of the metasurface element is good at the operating frequency of 5.8 GHz; that is, the metasurface structure can capture electromagnetic wave energy. By calculating the received power of the lumped port, it can be seen that the RF energy harvesting efficiency of the metasurface energy harvester at 5.8 GHz can reach more than 90%. So we de-

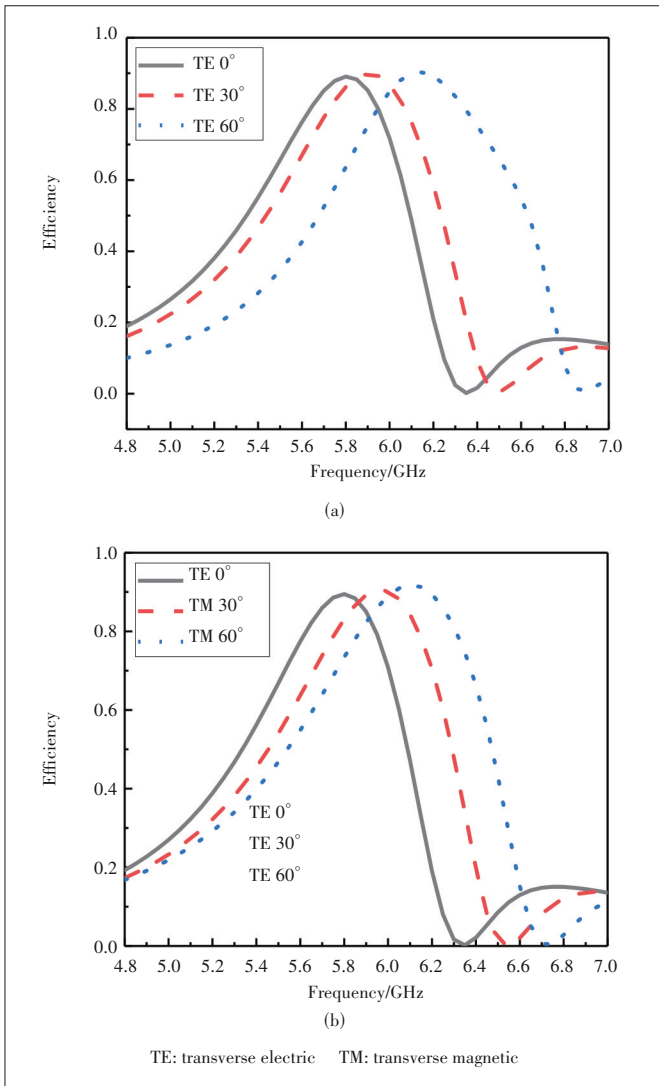
sign a 2×2 metasurface array and converge four lumped ports into one port output through the combiner, which is convenient for subsequent combination with the rectifier circuit. The structure is shown in Fig. 13(b), which is divided into five layers in total. From the top to the bottom, the first layer is the metasurface array, the second layer is an F4B dielectric substrate, the third layer is ground, the fourth layer is an S7136 H dielectric substrate (relative permittivity is 3.55, and loss tangent is 0.004) with a thickness of 0.5 mm, and the fifth layer is a combiner. The whole structure can efficiently collect electromagnetic wave energy and output it through one port. To verify the incident angle and polarization stability of the metasurface structure, it is necessary to consider two cases of transverse electric (TE) and transverse magnetic (TM) oblique incidence. Fig. 15(a) shows the energy harvesting efficiency of TE polarization at different incident angles. When the incident angle is 0° , the maximum energy harvesting efficiency obtained at 5.8 GHz is 90%. When the incident angle is 30° , the maximum energy harvesting efficiency obtained at 5.9 GHz is 90%, and the energy harvesting efficiency at 5.8 GHz is 86%. When the incident angle is 60° , the maximum energy harvesting efficiency obtained at 6 GHz is 91%, and the energy collection efficiency at 5.8 GHz is 70%.

For TM polarization, as it is shown in Fig. 15(b), when the incident angles are 0° , 30° , and 60° , the MS will obtain the maximum energy collection efficiency at 5.8 GHz, 5.95 GHz, and 6.11 GHz, and their values are all near 90%. For 5.8 GHz, the energy harvesting efficiency of 30° and 60° oblique incidences is 83% and 74%, respectively. From the above analysis results, it can be seen that be it TE polarization or TM polarization, the working frequency of the maximum harvesting efficiency of the MS will shift as the incident angle increases. However, the energy harvesting efficiency at 5.8 GHz remains above 70%, showing good incident angle and polarization stability compared with traditional receiving antennas.

In order to convert the RF energy collected by the MS array into DC energy, we select MA4E1317 Schottky Barrier Diode



▲ Figure 14. $|S_{11}|$ and RF harvesting efficiency of the proposed metasurface element

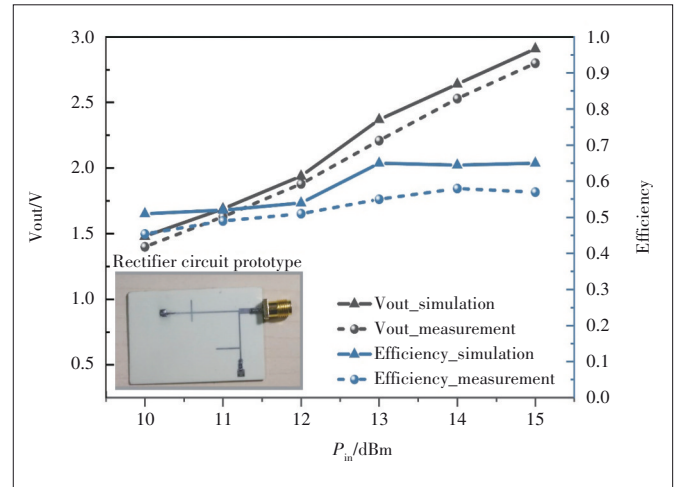


▲ Figure 15. Energy harvesting efficiency of metasurface: (a) TE polarization oblique incidence ($0 - 60^\circ$), (b) TM polarization oblique incidence ($0 - 60^\circ$)

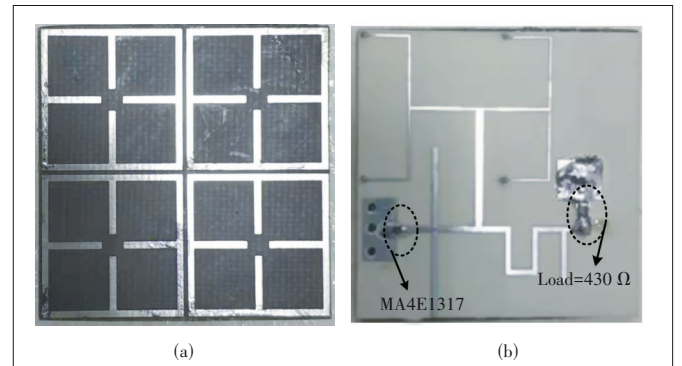
(SBD) from MACOM as the rectifier device and designed an F-type rectifier circuit that works at 5.8 GHz. The selected dielectric substrate is the same as the dielectric substrate of the metasurface combiner in order to integrate the design with the MS array and reduce the cost. The size of the designed rectifier circuit is $25 \times 15 \text{ mm}^2$, which is easy to integrate. The test and simulation performance are shown in Fig. 16. It can be found that when the input power is in the range of 12 dBm to 15 dBm, the rectification efficiency can be stabilized above 55%, and the output voltage at this time is higher than 1.6 V, which can provide energy for some low-power electrical appliances. In order to reduce the volume, we integrate the metasurface array and the rectifier circuit and process the principle prototype, as shown in Fig. 17, which can be used as the wireless energy harvesting part of the strategy we propose in this paper. Furthermore, a compact dual-band, wide-angle, and polarization-angle-independent rectifying metasurface can be applied for ambient energy harvesting^[38].

4.2 Accurate WPT Efficiency Analysis of PMS

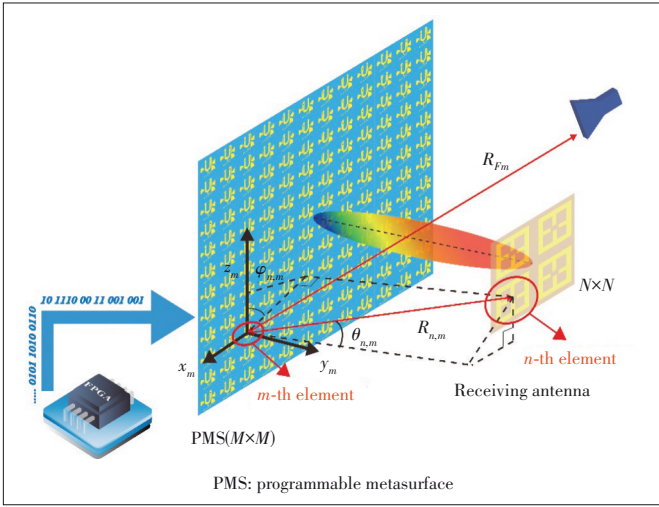
We accurately analyze the wireless power transmission efficiency from the near-field to far-field regions for the PMS. Fig. 18 shows the schematic diagram of the WPT system



▲ Figure 16. Rectifier circuit efficiency and output voltage



▲ Figure 17. A prototype of the rectifying metasurface: (a) front side and (b) backside



▲ Figure 18. Schematic diagram of the wireless power transfer (WPT) system based on PMS and rectifying metasurface

based on PMS. The transmitting part includes a feed horn and a PMS composed of $M \times M = 20 \times 20$ meta-atoms, and the receiving part is the $N \times N = 2 \times 2$ rectifying metasurface proposed in Section 4.1. The PMS is fed through a vertically incident horn antenna, and the transmitted power is P_T . The power of each element on the PMS can be extracted. Because the PMS is large enough, even if the receiving element is in the near field of the array, the receiving element is in the far field relative to the PMS element. Therefore, the energy received by the n -th receiving element from the m -th PMS element can be represented by Eq. (16). Where P_{sm} is the power of the m -th element of the PMS, λ is the wavelength. $G_{sm}(\theta_{n,m}, \phi_{n,m})$ and $G_{rn}(\theta_{n,m}, \phi_{n,m})$ are the gain of the m -th element of the PMS and the n -th element of the receiving antenna array, and $R_{n,m}$ is the distance between the two elements.

The power density can be expressed as $W = |E|^2/2\eta$. The amplitude of the electric field from the m -th element on the PMS to the n -th element of the receiving antenna array can be calculated by Eq. (17), where η is the wave impedance, k is the wavenumber, and $e^{-j(kR_{n,m} - \beta_m)}$ is the electric field phase. β_m is the initial phase of the PMS element which can be calculated by Eq. (18), where R_{Fm} is the distance from the phase center of the feed horn to the phase center of the PMS element, and β_{cm} is the compensation phase. According to the definition of power density, the power density received by the n -th receiving element from the m -th PMS element is $W_{n,m} = P_{sm}/(4\pi R_{n,m}^2)^{[77]}$. Assuming that the radiation source is isotropic, the power generated at R distance from the power source is $P = 4\pi R^2 W = 4\pi R^2 |E|^2/2\eta$. Eq. (19) can calculate the power received by the n -th receiving element from the entire PMS. The total power P_R received by the receiving antenna is the superposition of the power of each receiving element. The wireless power transmission efficiency is defined as the ratio of the total power received by the receiving antenna array to the microwave power emitted by the feed horn, as shown in Eq. (21).

It is worth noting that the PMS proposed in this paper introduces insertion loss due to the PIN diodes, which mainly affects the gain of antennas, so Eq. (21) is also applicable to the efficiency calculation of the PMS.

$$P_{r_{n,m}} = P_{s_m} G_{s_m}(\theta_{n,m}, \phi_{n,m}) G_{r_n}(\theta_{n,m}, \phi_{n,m}) \left(\frac{\lambda}{4\pi R_{n,m}} \right)^2. \quad (16)$$

$$E_{n,m} = \sqrt{2\eta W_{n,m}} e^{-j(kR_{n,m} - \beta_m)}. \quad (17)$$

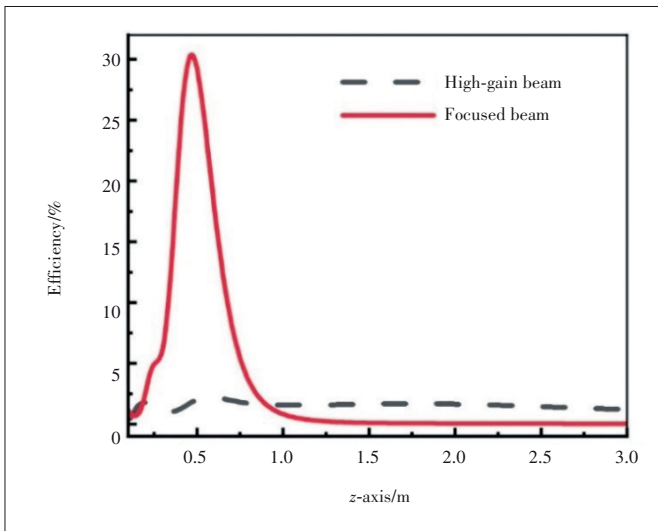
$$\beta_m = \beta_{c_m}(l) - kR_{F_m}. \quad (18)$$

$$P_{r_n} = \frac{4\pi}{2\eta} \left| \sum_{m=1}^M R_{n,m} E_{n,m} \right|^2 = \left(\frac{\lambda}{4\pi} \right)^2 \left| \sum_{m=1}^M \sqrt{P_{s_m} G_{s_m}(\theta_{n,m}, \phi_{n,m}) G_{r_n}(\theta_{n,m}, \phi_{n,m})} \frac{e^{-j(kR_{n,m} - \beta_m(l) + kR_{F_m})}}{R_{n,m}} \right|^2. \quad (19)$$

$$P_R = \left(\frac{\lambda}{4\pi} \right)^2 \left(\sum_{n=1}^N \left| \sum_{m=1}^M \sqrt{P_{s_m} G_{s_m}(\theta_{n,m}, \phi_{n,m}) G_{r_n}(\theta_{n,m}, \phi_{n,m})} \frac{e^{-j(kR_{n,m} - \beta_m(l) + kR_{F_m})}}{R_{n,m}} \right|^2 \right). \quad (20)$$

$$\frac{P_R}{P_T} = \left(\frac{\lambda}{4\pi} \right)^2 \frac{\left(\sum_{n=1}^N \left| \sum_{m=1}^M \sqrt{P_{s_m} G_{s_m}(\theta_{n,m}, \phi_{n,m}) G_{r_n}(\theta_{n,m}, \phi_{n,m})} \frac{e^{-j(kR_{n,m} - \beta_m(l) + kR_{F_m})}}{R_{n,m}} \right|^2 \right)}{P_T}. \quad (21)$$

For the WPT system composed of PMS, we analyze the transmission efficiency of the beams mentioned in Sections 3.1 and 3.2. Fig. 19 shows the efficiency comparison of different beams when propagating along the center of the PMS. For focused beams, we can see from the figure that the transmission efficiency at our preset focal point (0 m, 0 m, 0.5 m) is higher than 25% and much higher than the transmission efficiency of the high-gain beam. But as the transmission distance increases or decreases, the transmission efficiency of the focused beam will drop sharply. This can be solved by the strategy mentioned in this paper, which is to achieve precise positioning by transmitting location information. When the distance between the receiving metasurface array and the PMS is greater than 1 m, the advantages of the high-gain beam are gradually revealed. Its transmission efficiency is greater than that of the focused beam, suitable for long-distance wireless



▲ Figure 19. Wireless power transmission efficiency versus distance using high-gain beam and focused beam

power transmission. Based on the above analysis results, it can be obtained that the high-gain beam is suitable for the far-field WPT system, and the focused beam is suitable for the near-field WPT system. It fully demonstrates the feasibility of the strategy proposed in this paper.

5 Future Work and Conclusions

In previous sections, we describe a new strategy for the SWIPT system using the advanced metamaterials, PMS, including the overall solution scheme, the adaptively smart WPT strategy, WEH metasurfaces, and wireless power transmission efficiency analyses. We emphasize that the WPT and WEH using PMS are the major topics of this work because of the information that PMSs have been deeply studied. When the two aspects are properly unified, a feasible SWIPT solution to the self-sustainable 6G network may be realized. In this section, we discuss future research directions of the SWIPT network based on the PMS solution scheme, and make a systematic conclusion of this paper.

5.1 Full-Duplex PMS

A typical PMS could operate the amplitude, phase, and polarization of the incident EM waves. Technically, PMS is suitable for changing the channel state, which cannot be used to enhance the communication capacity. Researchers are aware of this and some RF channel operational PMSs have been reported^[78-80]. The concept and prototype of multiple-input multiple-output (MIMO) PMS were proposed and tested^[81]. Besides, a novel holographic MIMO surface was envisioned for the 6G network^[82]. A theoretical analysis of dynamic metasurface antennas for uplink massive MIMO systems was presented in Ref. [83]. However, a complete uplink and downlink experiment based on PMS is still unavailable. Thus, realizing a full-duplex PMS would be the major research direction in

the future.

5.2 Wireless Information and Power Integrated Surface

Imposing WPT and WEH techniques presented in this paper on the full-duplex PMS, we have a wireless information and power integrated surface (WIPIS), which is our main solution scheme to the SWIPT network. Distinct from the existing SWIPT, the WIPIS scheme depends on a cutting-edge technique, PMS. Both the information modulation and power management implemented by such a paradigm will gain more attention in microwave techniques, antenna propagation, and wireless communication communities. Although great efforts have been put into the WIPIS prototype design and modeling, it is still at the early stage. In the foreseeable future, we believe that the WIPIS-based system would appear. Recent advances in metamaterials and metasurfaces can stimulate the research for simultaneous wireless information and power transmission^[84-87].

5.3 Base Station Side, Relay Side, and Edge Side WIPIS

For different working scenarios, the WIPIS should provide distinct functionalities. A three-layer architecture of a WIPIS-based network is envisioned, including the base station side, the relay side, and the edge side. On the base station side, a WIPIS base station could offer point-to-point, point-to-multipoint, and specific area power coverage services in addition to mobile network access. On the relay side, a WIPIS could operate as a repeater or improve the channels. Besides, the relay WIPIS redistributes wireless power to surrounding IoT sensors or the edge side WIPIS. We emphasize that the main energy for a relay WIPIS is guaranteed by the WIPIS base station. At the edge side, microwatt level devices are accompanied by the low-level WIPISs which connect the relay WIPIS and coordinate the energy interconnections. All these WIPISs collaborate to form a featured SWIPT wireless network.

5.4 Conclusions

A perspective strategy of using PMS for the SWIPT system is proposed. Based on the PMS hardware platform, we develop an adaptively smart WPT strategy including the numerical models and analysis results of the near-field and far-field WPT systems. To collect and capture the wireless powers, the rectifying metasurface is presented employing the WEH technique. More importantly, the wireless power transmission efficiency is analyzed when using PMS as the transmitter and the rectifying metasurface as the receiver, suggesting that the proposed PMS-based SWIPT network is efficient and low-cost. The future research directions using the proposed scheme are summarized. The opportunities and challenges co-exist for implementing the future SWIPT network that can fulfill the carbon peak and carbon neutralization development strategy.

References

- [1] ANDREWS J G, BUZZI S, CHOI W, et al., What will 5G be [J]. *IEEE journal on selected areas in communications*, 2014, 32(6): 1065 – 1082. DOI: 10.1109/JSAC.2014.2328098
- [2] HU R Q, QIAN Y. An energy efficient and spectrum efficient wireless heterogeneous network framework for 5G systems [J]. *IEEE communications magazine*, 2014, 52(5): 94 – 101. DOI: 10.1109/mcom.2014.6815898
- [3] AL-FUQAHA A, GUIZANI M, MOHAMMADI M, et al. Internet of Things: a survey on enabling technologies, protocols, and applications [J]. *IEEE communications surveys & tutorials*, 2015, 17(4): 2347 – 2376. DOI: 10.1109/COMST.2015.2444095
- [4] VARSHNEY L R. Transporting information and energy simultaneously [C]//*Proceedings of 2008 IEEE International Symposium on Information Theory*. IEEE, 2008: 1612 – 1616. DOI: 10.1109/ISIT.2008.4595260
- [5] PONNIMBADUGE P T D, JAYAKODY D N K, SHARMA S K, et al. Simultaneous wireless information and power transfer (SWIPT): recent advances and future challenges [J]. *IEEE communications surveys & tutorials*, 2018, 20(1): 264 – 302. DOI: 10.1109/COMST.2017.2783901
- [6] CLERCKX B, ZHANG R, SCHOBER R, et al. Fundamentals of wireless information and power transfer: from RF energy harvester models to signal and system designs [J]. *IEEE journal on selected areas in communications*, 2019, 37(1): 4 – 33. DOI: 10.1109/JSAC.2018.2872615
- [7] ZHANG R, HO C K. MIMO broadcasting for simultaneous wireless information and power transfer [J]. *IEEE transactions on wireless communications*, 2013, 12(5): 1989 – 2001. DOI: 10.1109/TWC.2013.031813.120224
- [8] HUANG K B, LARSSON E G. Simultaneous information-and-power transfer for broadband downlink systems [C]//*IEEE International Conference on Acoustics, Speech and Signal Processing*. IEEE, 2013. DOI: 10.1109/ICASSP.2013.6638500
- [9] DIAMANTOULAKIS P D, KARAGIANNIDIS G K, DING Z G. Simultaneous lightwave information and power transfer (SLIPT) [J]. *IEEE transactions on green communications and networking*, 2018, 2(3): 764 – 773. DOI: 10.1109/TGCN.2018.2818325
- [10] DO T P, SONG I, KIM Y H. Simultaneous wireless transfer of power and information in a decode-and-forward two-way relaying network [J]. *IEEE transactions on wireless communications*, 2017, 16(3): 1579 – 1592. DOI: 10.1109/TWC.2017.2648801
- [11] ZHOU X, ZHANG R, HO C K. Wireless information and power transfer: architecture design and rate-energy tradeoff [J]. *IEEE transactions on communications*, 2013, 61(11): 4754 – 4767. DOI: 10.1109/TCOMM.2013.13.120855
- [12] KRIKIDIS I, TIMOTHEOU S, NIKOLAOU S, et al. Simultaneous wireless information and power transfer in modern communication systems [J]. *IEEE communications magazine*, 2014, 52(11): 104 – 110. DOI: 10.1109/MCOM.2014.6957150
- [13] CHEN H, LI Y H, JIANG Y X, et al. Distributed power splitting for SWIPT in relay interference channels using game theory [J]. *IEEE transactions on wireless communications*, 2015, 14(1): 410 – 420. DOI: 10.1109/TWC.2014.2349892
- [14] KHAN T A, ALKHATEEB A, HEATH R W. Millimeter wave energy harvesting [J]. *IEEE transactions on wireless communications*, 2016, 15(9): 6048 – 6062. DOI: 10.1109/TWC.2016.2577582
- [15] XIA M H, AISSA S. On the efficiency of far-field wireless power transfer [J]. *IEEE transactions on signal processing*, 2015, 63(11): 2835 – 2847. DOI: 10.1109/TSP.2015.2417497
- [16] LIU H W, KIM K J, KWAK K S, et al. Power splitting-based SWIPT with decode-and-forward full-duplex relaying [J]. *IEEE transactions on wireless communications*, 2016, 15(11): 7561 – 7577. DOI: 10.1109/TWC.2016.2604801
- [17] LU X, WANG P, NIYATO D, et al. Wireless charging technologies: Fundamentals, standards, and network applications [J]. *IEEE communications surveys & tutorials*, 2016, 18(2): 1413 – 1452. DOI: 10.1109/COMST.2015.2499783
- [18] NG D W K, LO E S, SCHOBER R. Wireless information and power transfer: energy efficiency optimization in OFDMA systems [J]. *IEEE transactions on wireless communications*, 2013, 12(12): 6352 – 6370. DOI: 10.1109/TWC.2013.103113.130470
- [19] KURS A, KARALIS A, MOFFATT R, et al. Wireless power transfer via strongly coupled magnetic resonances [J]. *Science*, 2007, 317(5834): 83 – 86. DOI: 10.1126/science.1143254
- [20] MAYORDOMO I, DRÄGER T, SPIES P, et al. An overview of technical challenges and advances of inductive wireless power transmission [J]. *Proceedings of the IEEE*, 2013, 101(6): 1302 – 1311. DOI: 10.1109/JPROC.2013.2243691
- [21] COVIC G A, BOYS J T. Inductive power transfer [J]. *Proceedings of the IEEE*, 2013, 101(6): 1276 – 1289. DOI: 10.1109/JPROC.2013.2244536
- [22] ZHANG Z, PANG H L, GEORGIADIS A, et al. Wireless power transfer: an overview [J]. *IEEE transactions on industrial electronics*, 2019, 66(2): 1044 – 1058. DOI: 10.1109/TIE.2018.2835378
- [23] HUI S Y R, ZHONG W X, LEE C K. A critical review of recent progress in mid-range wireless power transfer [J]. *IEEE transactions on power electronics*, 2014, 29(9): 4500 – 4511. DOI: 10.1109/TPEL.2013.2249670
- [24] BROWN W C. The history of power transmission by radio waves [J]. *IEEE transactions on microwave theory and techniques*, 1984, 32(9): 1230 – 1242. DOI: 10.1109/TMTT.1984.1132833
- [25] BROWN W C. Status of the microwave power transmission components for the solar power satellite [J]. *IEEE transactions on microwave theory and techniques*, 1981, 29(12): 1319 – 1327. DOI: 10.1109/TMTT.1981.1130559
- [26] SHINOHARA N. History and innovation of wireless power transfer via microwaves [J]. *IEEE journal of microwaves*, 2021, 1(1): 218 – 228. DOI: 10.1109/JMW.2020.3030896
- [27] YANG B, CHEN X J, CHU J, et al. A 5.8-GHz phased array system using power-variable phase-controlled magnetrons for wireless power transfer [J]. *IEEE transactions on microwave theory and techniques*, 2020, 68(11): 4951 – 4959. DOI: 10.1109/TMTT.2020.3007187
- [28] RODENBECK C T, JAFFE P I, STRASSNER B H, et al. Microwave and millimeter wave power beaming [J]. *IEEE journal of microwaves*, 2021, 1(1): 229 – 259. DOI: 10.1109/jmw.2020.3033992
- [29] SHINOHARA N. Trends in wireless power transfer: WPT technology for energy harvesting, millimeter-wave/THz rectennas, MIMO-WPT, and advances in near-field WPT applications [J]. *IEEE microwave magazine*, 2021, 22(1): 46 – 59. DOI: 10.1109/MMM.2020.3027935
- [30] TAKABAYASHI N, SHINOHARA N, MITANI T, et al. Rectification improvement with flat-topped beams on 2.45-GHz rectenna arrays [J]. *IEEE transactions on microwave theory and techniques*, 2020, 68(3): 1151 – 1163. DOI: 10.1109/TMTT.2019.2951098
- [31] WANG C, YANG B, SHINOHARA N. Study and design of a 2.45-GHz rectifier achieving 91% efficiency at 5-W input power [J]. *IEEE microwave and wireless components letters*, 2021, 31(1): 76 – 79. DOI: 10.1109/LMWC.2020.3032574
- [32] CUI T J, SMITH D, LIU R P, et al. *Metamaterials: theory, design and applications* [M]. Heidelberg, Germany: Springer, 2010. DOI: 10.1007/978-1-4419-0573-4
- [33] YU N F, GENEVEY P, KATS M A, et al. Light propagation with phase discontinuities: generalized laws of reflection and refraction [J]. *Science*, 2011, 334(6054): 333 – 337. DOI: 10.1126/science.1210713
- [34] YU N, CAPASSO F. Flat optics with designer metasurfaces [J]. *Nature materials*, 2014, 13(2): 139 – 150. DOI: 10.1038/nmat3839
- [35] LIU R, JI C, MOCK J J, et al. Broadband ground-plane cloak [J]. *Science*, 2009, 323(5912): 336 – 369. DOI: 10.1126/science.1166949
- [36] ZHOU J F, ZHANG P, HAN J Q, et al. Metamaterials and metasurfaces for wireless power transfer and energy harvesting [J]. *Proceedings of the IEEE*, 2022, 110(1): 31 – 55. DOI: 10.1109/JPROC.2021.3127493
- [37] LI L, ZHANG P, CHENG F J, et al. An optically transparent near-field focusing metasurface [J]. *IEEE transactions on microwave theory and techniques*, 2021, 69(4): 2015 – 2027. DOI: 10.1109/TMTT.2021.3061475
- [38] LI L, ZHANG X M, SONG C Y, et al. Compact dual-band, wide-angle, polarization-angle-independent rectifying metasurface for ambient energy harvesting and wireless power transfer [J]. *IEEE transactions on microwave theory and techniques*, 2021, 69(3): 1518 – 1528. DOI: 10.1109/TMTT.2020.3040962
- [39] LI L, ZHANG X M, SONG C Y, et al. Progress, challenges, and perspective on metasurfaces for ambient radio frequency energy harvesting [J]. *Applied physics letters*, 2020, 116(6): 060501. DOI: 10.1063/1.5140966
- [40] ERKMEN F, ALMONEEF T S, RAMAHI O M. Scalable electromagnetic energy harvesting using frequency-selective surfaces [J]. *IEEE transactions on microwave theory and techniques*, 2018, 66(5): 2433 – 2441. DOI: 10.1109/TMTT.2018.2804956
- [41] ALMONEEF T S, RAMAHI O M. Metamaterial electromagnetic energy harvester with near unity efficiency [J]. *Applied physics letters*, 2015, 106(15): 153902. DOI: 10.1063/1.4916232

- [42] ZHANG X M, LIU H X, LI L. Tri-band miniaturized wide-angle and polarization-insensitive metasurface for ambient energy harvesting [J]. *Applied physics letters*, 2017, 111(7): 071902. DOI: 10.1063/1.4999327
- [43] ALAVIKIA B, ALMONEEF T S, RAMAHI O M. Wideband resonator arrays for electromagnetic energy harvesting and wireless power transfer [J]. *Applied physics letters*, 2015, 107(24): 243902. DOI: 10.1063/1.4937591
- [44] ZHANG P, YI H, LIU H X, et al. Back-to-back microstrip antenna design for broadband wide-angle RF energy harvesting and dedicated wireless power transfer [J]. *IEEE access*, 2020, 8: 126868 – 126875. DOI: 10.1109/ACCESS.2020.3008551
- [45] ZHANG P, LI L, ZHANG X M, et al. Design, measurement and analysis of near-field focusing reflective metasurface for dual-polarization and multi-focus wireless power transfer [J]. *IEEE access*, 2019, 7: 110387 – 110399. DOI: 10.1109/ACCESS.2019.2934135
- [46] YU S X, LIU H X, LI L. Design of near-field focused metasurface for high-efficient wireless power transfer with multifocus characteristics [J]. *IEEE transactions on industrial electronics*, 2019, 66(5): 3993 – 4002. DOI: 10.1109/TIE.2018.2815991
- [47] CUI T J, QI M Q, WAN X, et al. Coding metamaterials, digital metamaterials and programmable metamaterials [J]. *Light: science & applications*, 2014, 3(10): 218. DOI: 10.1038/lsa.2014.99
- [48] HAN J Q, LI L, MA X J, et al. Adaptively smart wireless power transfer using 2-bit programmable metasurface [J]. *IEEE transactions on industrial electronics*, 2022, 69(8): 8524 – 8534. DOI: 10.1109/TIE.2021.3105988
- [49] DAI J Y, TANG W K, CHEN M Z, et al. Wireless communication based on information metasurfaces [J]. *IEEE transactions on microwave theory and techniques*, 2021, 69(3): 1493 – 1510. DOI: 10.1109/TMTT.2021.3054662
- [50] ZHANG L, CHEN X Q, LIU S, et al. Space-time-coding digital metasurfaces [J]. *Nature communications*, 2018, 9: 4334. DOI: 10.1038/s41467-018-06802-0
- [51] ZHANG L, CUI T J. Space-time-coding digital metasurfaces: principles and applications [J]. *Research*, 2021: 1 – 25. DOI: 10.34133/2021/9802673
- [52] WU H T, BAI G D, LIU S, et al. Information theory of metasurfaces [J]. *National science review*, 2020, 7(3): 561 – 571. DOI: 10.1093/nsr/nwz195
- [53] CUI T J, LI L L, LIU S, et al. Information metamaterial systems [J]. *IScience*, 2020, 23(8): 101403. DOI: 10.1016/j.isci.2020.101403
- [54] MA Q, CUI T J. Information Metamaterials: Bridging the physical world and digital world [J]. *PhotonIX*, 2020, 1: 1. DOI: 10.1186/s43074-020-00006-w
- [55] ZHANG L, CHEN M Z, TANG W K, et al. A wireless communication scheme based on space- and frequency-division multiplexing using digital metasurfaces [J]. *Nature electronics*, 2021, 4(3): 218 – 227. DOI: 10.1038/s41928-021-00554-4
- [56] TANG W K, DAI J Y, CHEN M Z, et al. MIMO transmission through reconfigurable intelligent surface: System design, analysis, and implementation [J]. *IEEE journal on selected areas in communications*, 2020, 38(11): 2683 – 2699. DOI: 10.1109/JSAC.2020.3007055
- [57] CHEN M Z, TANG W K, DAI J Y, et al. Accurate and broadband manipulations of harmonic amplitudes and phases to reach 256 QAM millimeter-wave wireless communications by time-domain digital coding metasurface [J]. *National science review*, 2021, 9(1): 134. DOI: 10.1093/nsr/nwab134
- [58] WU H, GAO X X, ZHANG L, et al. Harmonic information transitions of spatiotemporal metasurfaces [J]. *Light: science & applications*, 2020, 9: 198. DOI: 10.1038/s41377-020-00441-1
- [59] ZHAO H T, SHUANG Y, WEI M L, et al. Metasurface-assisted massive backscatter wireless communication with commodity Wi-Fi signals [J]. *Nature communications*, 2020, 11: 3926. DOI: 10.1038/s41467-020-17808-y
- [60] RUAN H X, LI L L. Imaging resolution analysis of single-frequency and single-sensor programmable microwave imager [J]. *IEEE transactions on antennas and propagation*, 2020, 68(11): 7727 – 7732. DOI: 10.1109/TAP.2020.2986653
- [61] LI L, SHUANG Y, MA Q, et al. Intelligent metasurface imager and recognizer [J]. *Light: science & applications*, 2019, 8: 97. DOI: 10.1038/s41377-019-0209-z
- [62] MA Q, BAI G D, JING H B, et al. Smart metasurface with self-adaptively reprogrammable functions [J]. *Light: science & applications*, 2019, 8: 98. DOI: 10.1038/s41377-019-0205-3
- [63] LI L L, RUAN H X, LIU C, et al. Machine-learning reprogrammable metasurface imager [J]. *Nature communications*, 2019, 10(1): 1082. DOI: 10.1038/s41467-019-09103-2
- [64] HUANG T J, TANG H H, TAN Y H, et al. Terahertz super-resolution imaging based on subwavelength metallic grating [J]. *IEEE transactions on antennas and propagation*, 2019, 67(5): 3358 – 3365. DOI: 10.1109/TAP.2019.2894260
- [65] ELMOSSALLAMY M A, ZHANG H L, SONG L Y, et al. Reconfigurable intelligent surfaces for wireless communications: principles, challenges, and opportunities [J]. *IEEE transactions on cognitive communications and networking*, 2020, 6(3): 990 – 1002. DOI: 10.1109/TCCN.2020.2992604
- [66] BASAR E, DI RENZO M, DE ROSNY J, et al. Wireless communications through reconfigurable intelligent surfaces [J]. *IEEE access*, 2019, 7: 116753 – 116773. DOI: 10.1109/ACCESS.2019.2935192
- [67] WU Q Q, ZHANG R. Intelligent reflecting surface enhanced wireless network via joint active and passive beamforming [J]. *IEEE transactions on wireless communications*, 2019, 18(11): 5394 – 5409. DOI: 10.1109/TWC.2019.2936025
- [68] YANG X X, JIANG C, ELSHERBENI A Z, et al. A novel compact printed rectenna for data communication systems [J]. *IEEE transactions on antennas and propagation*, 2013, 61(5): 2532 – 2539. DOI: 10.1109/TAP.2013.2244550
- [69] LU P, YANG X S, WANG B Z. A two-channel frequency reconfigurable rectenna for microwave power transmission and data communication [J]. *IEEE transactions on antennas and propagation*, 2017, 65(12): 6976 – 6985. DOI: 10.1109/TAP.2017.2766450
- [70] CLARKE R H, BROWN J. *Diffraction theory and antennas* [M]. Chichester, UK: Halsted Press, 1980. DOI: 10.1016/0029-8018(81)90030-5
- [71] HAN J Q, LI L, LIU G Y, et al. A wideband 1 bit 12×12 reconfigurable beam-scanning reflectarray: design, fabrication, and measurement [J]. *IEEE antennas and wireless propagation letters*, 2019, 18(6): 1268 – 1272. DOI: 10.1109/LAWP.2019.2914399
- [72] ZHANG S, XUE H, CHANG M Y, et al. Generation of airy beams using an amplitude-phase-modulated metasurface [C]//*Proceedings of 2021 IEEE MTT-S International Microwave Workshop Series on Advanced Materials and Processes for RF and THz Applications*. IEEE, 2021: 332 – 334. DOI: 10.1109/IMWS-AMP53428.2021.9643966
- [73] ZHANG W Z, SONG C Y, PEI R, et al. Broadband metasurface antenna using hexagonal loop-shaped unit cells [J]. *IEEE access*, 2020, 8: 223797 – 223805. DOI: 10.1109/ACCESS.2020.3043656
- [74] YU F, YANG X X, ZHONG H T, et al. Polarization-insensitive wide-angle-reception metasurface with simplified structure for harvesting electromagnetic energy [J]. *Applied physics letters*, 2018, 113(12): 123903. DOI: 10.1063/1.5046927
- [75] XU P, WANG S Y, W G Y. Design of an effective energy receiving adapter for microwave wireless power transmission application [J]. *AIP advances*, 2016, 6(10): 105010. DOI: 10.1063/1.4966050
- [76] ZHANG X M, LIU H X, LI L. Electromagnetic power harvester using wide-angle and polarization-insensitive metasurfaces [J]. *Applied sciences*, 2018, 8(4): 497. DOI: 10.3390/app8040497
- [77] SONG C M, TRINH-VAN S, YI S H, et al. Analysis of received power in RF wireless power transfer system with array antennas [J]. *IEEE access*, 2021, 9: 76315 – 76324. DOI: 10.1109/ACCESS.2021.3083270
- [78] CHEN L, MA Q, JING H B, et al. Space-energy digital-coding metasurface based on an active amplifier [J]. *Physical review applied*, 2019, 11(5): 054051. DOI: 10.1103/physrevapplied.11.054051
- [79] MA Q, CHEN L, JING H B, et al. Controllable and programmable nonreciprocity based on detachable digital coding metasurface [J]. *Advanced optical materials*, 2019, 7(24): 1901285. DOI: 10.1002/adom.201901285
- [80] QIU T S, JIA Y X, WANG J F, et al. Controllable reflection-enhancement metasurfaces via amplification excitation of transistor circuit [J]. *IEEE transactions on antennas and propagation*, 2021, 69(3): 1477 – 1482. DOI: 10.1109/TAP.2020.3019351
- [81] TANG W K, DAI J Y, CHEN M Z, et al. MIMO transmission through reconfigurable intelligent surface: System design, analysis, and implementation [J]. *IEEE journal on selected areas in communications*, 2020, 38(11): 2683 – 2699. DOI: 10.1109/JSAC.2020.3007055
- [82] HUANG C W, HU S, ALEXANDROPOULOS G C, et al. Holographic MIMO surfaces for 6G wireless networks: opportunities, challenges, and trends [J]. *IEEE wireless communications*, 2020, 27(5): 118 – 125. DOI: 10.1109/

MWC.001.1900534

- [83] SHLEZINGER N, DICKER O, ELDAR Y C, et al. Dynamic metasurface antennas for uplink massive MIMO systems [J]. *IEEE transactions on communications*, 2019, 67(10): 6829 – 6843. DOI: 10.1109/TCOMM.2019.2927213
- [84] TIAN S C, ZHANG X M, WANG X, et al. Recent advances in metamaterials for simultaneous wireless information and power transmission [J]. *Nanophotonics*, 2022: 1 – 27. DOI: 10.1515/nanoph-2021-0657
- [85] WANG X, HAN J Q, TIAN S C, et al. Amplification and manipulation of non-linear electromagnetic waves and enhanced nonreciprocity using transmissive space-time-coding metasurface [J]. *Advanced science*, 2022, 9(11): 2105960. DOI: 10.1002/advs.202105960
- [86] ZHANG P, ZHANG X M, LI L. An optically transparent metantenna for RF wireless energy harvesting [J]. *IEEE transactions on antennas and propagation*, 2022, 70(4): 2550 – 2560. DOI: 10.1109/TAP.2021.3137166
- [87] LI L, ZHANG P, HAN J, et al. Key technologies of microwave wireless power transfer and energy harvesting based on electromagnetic metamaterials [J]. *Acta photonica sinica*, 2021, 50(10): 1016001. DOI: 10.3788/gzxb20215010.1016001

Biographies

CHANG Mingyang received the BE degree in electronic information science and technology from Yantai University, China in 2018. He is currently pursuing the PhD degree in electromagnetic fields and microwave technology at Xidian University, China. His research interests include wireless power transfer, wireless energy harvesting, metasurfaces, and simultaneous wireless information and power transfer.

HAN Jiaqi received the BE degree in electronic and information engineering from Henan Normal University, China in 2014, and the PhD degree in electromagnetic fields and microwave technology from Xidian University, China in 2019. He is currently a post-doctoral fellow with the School of Electronic Engineering, Xidian University. His research interests include the design of programmable metasurfaces and their applications on wireless power transfer and computational imaging.

MA Xiangjin received the BE degree in communication engineering from Nanchang Institute of Technology, China in 2019. He is currently pursuing the PhD degree in electromagnetic field and microwave technology at Xidian University, China. His current research interests include analysis and application of programmable metasurfaces, design of high-performance programmable metasur-

faces and microwave holographic imaging.

XUE Hao received the BE degree in electronic and information engineering from Xidian University, China in 2015. He is currently pursuing the PhD degree in electronic science and technology at Xidian University. His research interests include antenna design, metasurface, wireless power transfer, and OAM vortex beam. He received the honors and awards include the National scholarship for postgraduates 2017, the Best Student Paper Awards of IEEE iWAT 2018, and IEEE IMWS-AMP 2021.

WU Xiaonan received the BE degree in electronic information engineering from Xidian University, China in 2020. He is currently pursuing the master's degree in electromagnetic field and microwave technology at Xidian University. His research interests include wireless power transfer, wireless energy harvesting, design of metasurfaces, and simultaneous wireless information and power transfer.

LI Long (lilong@mail.xidian.edu.cn) received the BE and PhD degrees in electromagnetic fields and microwave technology from Xidian University, China in 1998 and 2005, respectively. He is currently a professor in the School of Electronic Engineering, Xidian University. Prof. LI is the Director of Key Laboratory of High-Speed Circuit Design and EMC, Ministry of Education, China. His research interests include metamaterials/metasurfaces, antennas and microwave devices, wireless power transfer and harvesting technology, and OAM vortex waves. He has published over 180 papers in journals and held more than 40 patents. Prof. LI was awarded the Chang Jiang Scholars Distinguished Professor by Ministry of Education, China in 2021. Prof. LI is the Vice-President of MTT-Chapter in IEEE Xi'an Section. He is a TPC Co-Chair of APCAP2017 and a General Co-Chair of AWPT2019.

CUI Tiejun (tjcui@seu.edu.cn) received the BS, MS, and PhD degrees in electrical engineering from Xidian University, China in 1987, 1990, and 1993, respectively. He is currently the Chief Professor of Southeast University, China. Prof. CUI is the Academician of Chinese Academy of Science and an IEEE Fellow. Prof. CUI's research interests include metamaterials and computational electromagnetics. He proposed the concepts of digital coding and programmable metamaterials, and realized their first prototypes, based on which he founded the new direction of information metamaterials, bridging the physical world and digital world. He has published over 500 peer-review journal papers, which have been cited by more than 43 000 times (H-Factor 105, Google Scholar), and licensed over 150 patents. Prof. CUI was awarded a Cheung Kong Professor by the Ministry of Education, China in 2001, and received the National Science Foundation of China for Distinguished Young Scholars in 2002. Prof. CUI received the Natural Science Award (first class) from the Ministry of Education, China in 2011, and the National Natural Science Awards of China (second class, twice) in 2014 and 2018, respectively.

ZTE Communications Guidelines for Authors

Remit of Journal

ZTE Communications publishes original theoretical papers, research findings, and surveys on a broad range of communications topics, including communications and information system design, optical fiber and electro-optical engineering, microwave technology, radio wave propagation, antenna engineering, electromagnetics, signal and image processing, and power engineering. The journal is designed to be an integrated forum for university academics and industry researchers from around the world.

Manuscript Preparation

Manuscripts must be typed in English and submitted electronically in MS Word (or compatible) format. The word length is approximately 3 000 to 8 000, and no more than 8 figures or tables should be included. Authors are requested to submit mathematical material and graphics in an editable format.

Abstract and Keywords

Each manuscript must include an abstract of approximately 150 words written as a single paragraph. The abstract should not include mathematics or references and should not be repeated verbatim in the introduction. The abstract should be a self-contained overview of the aims, methods, experimental results, and significance of research outlined in the paper. Five carefully chosen keywords must be provided with the abstract.

References

Manuscripts must be referenced at a level that conforms to international academic standards. All references must be numbered sequentially in-text and listed in corresponding order at the end of the paper. References that are not cited in-text should not be included in the reference list. References must be complete and formatted according to *ZTE Communications* Editorial Style. A minimum of 10 references should be provided. Footnotes should be avoided or kept to a minimum.

Copyright and Declaration

Authors are responsible for obtaining permission to reproduce any material for which they do not hold copyright. Permission to reproduce any part of this publication for commercial use must be obtained in advance from the editorial office of *ZTE Communications*. Authors agree that a) the manuscript is a product of research conducted by themselves and the stated co-authors; b) the manuscript has not been published elsewhere in its submitted form; c) the manuscript is not currently being considered for publication elsewhere. If the paper is an adaptation of a speech or presentation, acknowledgement of this is required within the paper. The number of co-authors should not exceed five.

Content and Structure

ZTE Communications seeks to publish original content that may build on existing literature in any field of communications. Authors should not dedicate a disproportionate amount of a paper to fundamental background, historical overviews, or chronologies that may be sufficiently dealt with by references. Authors are also requested to avoid the overuse of bullet points when structuring papers. The conclusion should include a commentary on the significance/future implications of the research as well as an overview of the material presented.

Peer Review and Editing

All manuscripts will be subject to a two-stage anonymous peer review as well as copyediting, and formatting. Authors may be asked to revise parts of a manuscript prior to publication.

Biographical Information

All authors are requested to provide a brief biography (approx. 100 words) that includes email address, educational background, career experience, research interests, awards, and publications.

Acknowledgements and Funding

A manuscript based on funded research must clearly state the program name, funding body, and grant number. Individuals who contributed to the manuscript should be acknowledged in a brief statement.

Address for Submission

<http://mc03.manuscriptcentral.com/ztecom>

ZTE COMMUNICATIONS

中兴通讯技术(英文版)

ZTE Communications has been indexed in the following databases:

- Abstract Journal
- Cambridge Scientific Abstracts (CSA)
- China Science and Technology Journal Database
- Chinese Journal Fulltext Databases
- Index of Copernicus
- Ulrich's Periodicals Directory
- Wanfang Data
- WJCI 2021

Industry Consultants:

DUAN Xiangyang, GAO Yin, HU LiuJun, HUA Xinhai, LIU Xinyang, LU Ping, SHI Weiqiang, WANG Huitao, XIONG Xiankui, ZHU Xiaoguang, ZHAO Yajun, ZHAO Zhiyong

ZTE COMMUNICATIONS

Vol. 20 No. 2 (Issue 79)

Quarterly

First English Issue Published in 2003

Supervised by:

Anhui Publishing Group

Sponsored by:

Time Publishing and Media Co., Ltd.

Shenzhen Guangyu Aerospace Industry Co., Ltd.

Published by:

Anhui Science & Technology Publishing House

Edited and Circulated (Home and Abroad) by:

Magazine House of ZTE Communications

Staff Members:

General Editor: WANG Xiyu

Editor-in-Chief: JIANG Xianjun

Executive Editor-in-Chief: HUANG Xinming

Editorial Director: LU Dan

Editor-in-Charge: ZHU Li

Editors: REN Xixi, XU Ye, YANG Guangxi

Producer: XU Ying

Circulation Executive: WANG Pingping

Assistant: WANG Kun

Editorial Correspondence:

Add: 12F Kaixuan Building, 329 Jinzhai Road,

Hefei 230061, P. R. China

Tel: +86-551-65533356

Email: magazine@zte.com.cn

Website: <http://zte.magtechjournal.com>

Annual Subscription: RMB 120

Printed by:

Hefei Tiancai Color Printing Company

Publication Date: June 25, 2022

China Standard Serial Number: $\frac{\text{ISSN } 1673-5188}{\text{CN } 34-1294/\text{TN}}$